GeoSim

MODELING OF THE GREAT EARTHQUAKE SEISMIC CYCLES

Dissertation
zur Erlangung des akademischen Grades
"doctor rerum naturalium"
(Dr. rer. nat.)
in der Wissenschaftsdisziplin "Geophysik"

eingereicht an der
Mathematisch-Naturwissenschaftlichen Fakultät
der Universität Potsdam

vorgelegt von
Iskander Muldashev

Am Dezember 2016

Published online at the
Institutional Repository of the University of Potsdam:
URN urn:nbn:de:kobv:517-opus4-398926
http://nbn-resolving.de/urn:nbn:de:kobv:517-opus4-398926

To my parents, for their endless love, support and encouragement

To my grandfather who fostered my interest in physics

Abstract

The timing and location of the two largest earthquakes of the 21st century (Sumatra, 2004 and Tohoku 2011, events) greatly surprised the scientific community, indicating that the deformation processes that precede and follow great megathrust earthquakes remain enigmatic. During these phases before and after the earthquake a combination of multi-scale complex processes are acting simultaneously: Stresses built up by long-term tectonic motions are modified by sudden jerky deformations during earthquakes, before being restored by multiple ensuing relaxation processes.

This thesis details a cross-scale thermomechanical model developed with the aim of simulating the entire subduction process from earthquake (1 minute) to million years' time scale, excluding only rupture propagation. The model employs elasticity, non-linear transient viscous rheology, and rate-and-state friction. It generates spontaneous earthquake sequences, and, by using an adaptive time-step algorithm, recreates the deformation process as observed naturally over single and multiple seismic cycles. The model is thoroughly tested by comparing results to those from known high- resolution solutions of generic modeling setups widely used in modeling of rupture propagation. It is demonstrated, that while not modeling rupture propagation explicitly, the modeling procedure correctly recognizes the appearance of instability (earthquake) and correctly simulates the cumulative slip at a fault during great earthquake by means of a quasi-dynamic approximation.

A set of 2D models is used to study the effects of non-linear transient rheology on the postseismic processes following great earthquakes. Our models predict that the viscosity in the mantle wedge drops by 3 to 4 orders of magnitude during a great earthquake with magnitude above 9. This drop in viscosity results in spatial scales and timings of the relaxation processes following the earthquakes that are significantly different to previous estimates. These models replicate centuries long seismic cycles exhibited by the greatest earthquakes (like the Great Chile 1960 Earthquake) and are consistent with the major features of postseismic surface displacements recorded after the Great Tohoku Earthquake.

The 2D models are also applied to study key factors controlling maximum magnitudes of earthquakes in subduction zones. Even though methods of instrumentally observing earthquakes at subduction zones have rapidly improved in recent decades, the characteristic recurrence interval of giant earthquakes (Mw>8.5) is much larger than the currently available observational record and therefore the necessary conditions for giant earthquakes are not clear. Statistical studies have recognized the importance of the slab shape and its surface roughness, state of the strain of the upper plate and thickness of sediments filling the trenches. In this thesis we attempt to explain these observations and to identify key controlling parameters. We

test a set of 2D models representing great earthquake seismic cycles at known subduction zones with various known geometries, megathrust friction coefficients, and convergence rates implemented. We found that low-angle subduction (large effect) and thick sediments in the subduction channel (smaller effect) are the fundamental necessary conditions for generating giant earthquakes, while the change of subduction velocity from 10 to 3.5 cm/yr has a lower effect. Modeling results also suggest that having thick sediments in the subduction channel causes low static friction, resulting in neutral or slightly compressive deformation in the overriding plate for low-angle subduction zones. These modeling results agree well with observations for the largest earthquakes. The model predicts the largest possible earthquakes for subduction zones of given dipping angles. The predicted maximum magnitudes exactly threshold magnitudes of all known giant earthquakes of 20th and 21st centuries.

The clear limitation of most of the models developed in the thesis is their 2D nature. Development of 3D models with comparable resolution and complexity will require significant advances in numerical techniques. Nevertheless, we conducted a series of low-resolution 3D models to study the interaction between two large asperities at a subduction interface separated by an aseismic gap of varying width. The novelty of the model is that it considers behavior of the asperities during multiple seismic cycles. As expected, models show that an aseismic gap with a narrow width could not prevent rupture propagation from one asperity to another, and that rupture always crosses the entire model. When the gap becomes too wide, asperities do not interact anymore and rupture independently. However, an interesting mode of interaction was observed in the model with an intermediate width of the aseismic gap: In this model the asperities began to stably rupture in anti-phase following multiple seismic cycles. These 3D modeling results, while insightful, must be considered preliminary because of the limitations in resolution.

The technique developed in this thesis for cross-scale modeling of seismic cycles can be used to study the effects of multiple seismic cycles on the long-term deformation of the upper plate. The technique can be also extended to the case of continental transform faults and for the advanced 3D modeling of specific subduction zones. This will require further development of numerical techniques and adaptation of the existing advanced highly scalable parallel codes like LAMEM and ASPECT.

Zusammenfassung

Zeitpunkt und Ort der zwei größten Erdbeben des 21. Jahrhunderts (Sumatra 2004 und Tohoku 2011) überraschten die wissenschaftliche Gemeinschaft, da sie darauf hindeuten, dass die einem Megathrust-Erdbeben vorangehenden und folgenden Deformationsprozesse weiterhin rästelhaft bleiben. Ein Problem ist die komplexe Art der Subduktionsprozesse auf unterschiedlichen Skalen. Spannungen werden durch langzeitliche, tektonische Bewegungen aufgebaut, von plötzlicher, ruckartiger Deformation während Erdbeben modifiziert und anschließend durch verschiedene Entspannungsprozesse wiederhergestellt.

In dieser Arbeit wird ein skalen-übergreifendes thermomechanisches Modell entwickelt mit dem Ziel den vollständigen Subduktionsprozess von kleiner Skala (Minuten, z.B. Erdbeben) bis zu Millionen Jahren zu simulieren. Dabei bleibt nur das dynamische Prozess der unberücksichtigt. Das Modell nutzt Elastizität, nicht-lineare transient viskose Rheologie und „rate-and-state“ Reibungsgesetz. Es erzeugt spontane Erdbeben-Sequenzen und stellt durch das Nutzen eines adaptiven Zeitschritt Algorithmus den Deformationsprozess nach, wie er in der Natur während einzelner und mehrerer seismischer Zyklen beobachtet wird.

Anhand der 2D-Modell Reihe werden die Effekte der nicht-linearen transient (viskosen) Rheologie auf postseismische Prozesse nach großen Erdbeben untersucht. Die Modelle sagen eine Verringerung der Mantelkeil-Viskosität um 3 bis 4 Größenordnungen während der großen Erdbeben (Mw > 9) vorher. Im Gegensatz zur momentanen Meinung, ergeben sich andere räumliche und zeitliche Verteilungen des Entspannungsprozesses nach großen Erdbeben. Jahrhunderte lange seismische Zyklen, wie zum Beispiel das große Erdbeben in Chile 1960, werden reproduziert und stimmen mit den Hauptmerkmalen der postseismischen Oberflächenverschiebungen überein, die nach dem großen Tohoku Erdbeben aufgezeichnet wurden.

Mithilfe der 2D-Modelle werden außerdem Schlüsselfaktoren untersucht, die die maximale Magnitude von Erdbeben bestimmen. Obwohl die instrumentellen Methoden zur Beobachtung von Erdbeben in Subduktionszonen in den letzten Jahrzehnten stetig verbessert wurden, kann das Auftreten der größten Erdbeben (Mw > 8.5) und die dafür vorrauszusetzenden Bedingungen nicht genau bestimmt werden, da die charackeristische Zeit für ein Wiederauftreten deutlich größer als der Beobachtungszeitraum ist. Wir versuchen in dieser Arbeit diese Beobachtungen zu erklären und die kontrollierenden Schlüsselfaktoren zu bestimmen. Eine 2D-Modell Reihe mit großen, seismischen Erdbebenzyklen untersucht unterschiedliche Geometrien von Subduktionszonen sowie Reibungskoeffizieten an der Subduktions Platten-Grenzoberfläche und Konvergenzraten. Subduktion mit geringem Winkel (großer Effekt) und mächtige Sedimente im Subduktionskanal (kleiner Effekt) sind grundlegend notwendige Bedingungen für riesige Erdbeben, während eine Änderung des Reibungsparameters nur geringe Auswirkungen hat. Die Modellierungsergebnisse sind in

Übereinstimmung mit den Beobachtungen von den größten Erdbeben. Die maximale vohergesagte Magnituden liegen an der oberen Grenze alle historische Beben der 20. und 21. Jahrhunderden.

Die größte Einschränkung der entwickelten Modelle ist ihre 2-dimensionale Natur. Um die Interaktion zwischen zwei großen Unebenheiten („asperities“) auf der Subduktions Platten-Grenzoberfläche, die von einer aseismischen Lücke („gap“) voneinander getrennt sind, zu untersuchen, wurde eine 3D-Modell Reihe mit geringer Auflösung durchgeführt. Neu an diesem Modell ist, dass das Verhalten der Unebenheiten während mehrerer seismischer Zyklen berücksichtigt wird. Wie erwartet zeigt das Modell, dass eine schmale, aseismische Lücke ein Propagieren von Brüchen von einer Unebenheit zur nächsten nicht verhindern kann und diese Brüche das gesamte Modell durchkreuzen. Wird die Lücke zu groß interagieren die Unebenheiten nicht mehr miteinander und brechen unabhängig voneinander. Allerdings wurde in dem Modell mit mittlerer Breite der aseismischen Lücke eine interessante Art von Interaktion beobachtet: Nach einigen seismischen Zyklen beginnen die Unebenheiten kontinuerlich und zwar in Gegen-Phasen zu brechen. Diese Ergebnisse sind andeutend, aber können aufgrund der geringen Auflösung des Models nur als vorläufig angesehen werden und erfordern weitere Bestätigung mit hoch-auflösenden Modellen.

Contents

Chapter 1 Introduction

1.1 Previous Studies on Earthquake Modeling

Modeling of seismic cycles is important for understanding physics of earthquakes. Recent results in simulations of single events and whole seismic cycles in self-consistent models can be divided to the three major groups of studies: 1) modeling of rupture propagation, 2) modeling of viscoelastic postseismic relaxation, and 3) modelling of seismic cycles as sequence of earthquakes.

1.1.1 Modeling of Rupture Propagation

The challenge of modeling of rupture propagation and preceding nucleation comes from dramatic variations of slip velocities which can vary from millimeters per year during interseismic loading to meters per second during rupture. While giant earthquakes release large elastic strain, accumulation of this deformation can last centuries or even thousands of years. Taking into account many orders difference of characteristic slip velocities over the time, modeling of rupture propagation requires very high temporal and spatial resolution and adequate numerical techniques. Variety of methods were proposed.

Earlier implementations (e.g., Okubo, 1989; Shibazaki and Matsu'ura, 1992) employ a quasi-static method during slow deformation and then switched to a dynamic method once instability starts. However, sudden switching between numerical schemes may disrupt the natural development of the instability. Other approaches (e.g., Cochard and Madariaga, 1996; Myers et al., 1996]) neglect all aseismic fault slippage, so that stressing between earthquakes is trivially modeled, and give the fault a "kick" in the form of an abrupt small strength drop (means decrease of yield stress), once a critical stress has been reached somewhere. At that stage, an elastodynamic algorithm calculates rupture until arrest occurs. Another way is to use a tectonic loading rate that is only a few orders of magnitude less than representative seismic slip rates, rather than the roughly 10 orders as for natural faults, and to use standard elastodynamic numerical methodology throughout (Shaw and Rice, 2000). But this approach does not fit for modelling of large earthquakes.

Significant success in modelling of rupture propagations was achieved in integrated numerical scheme proposed by (Lapusta et al., 2000) which allows resolution of both slow and fast deformational phases, as well as the transition between them, within a single mathematical framework for elastodynamics. I explain this technique in more details below.

As it was mentioned before, this type of modelling requires high spatial resolution. If mesh is properly refined, perturbation on a single cell does not affect the system. Hence, the acceleration of the slipping cell can happen only as a part of the sliding patch. So the mesh

should be refined enough so space element size h should be much smaller than the critical cell size h^* ($\eta = \frac{h^*}{h} \gg 1$) which is defined:

$$h^* = \frac{\pi}{4}\frac{GL}{(b-a)\bar{\sigma}} \tag{1.1}$$

where G is shear modulus, ν is Poisson's ratio, L is characteristic slip distance, σ is effective normal stress, and a and b are rate-and-state friction parameters. Also, sometimes parameter $h^*$is called nucleation size.

Simulating of slow loading in interseismic and capturing details of occasional rapid failures requires evolution time step technique. Time step selection is based on the idea that its value should be the function of the fastest slip velocity in the model. Thus, method must assure proper integration of the constitutive law during the calculation. At every step largest displacement of any element should be smaller than characteristic slip evolution distance:

$$\Delta t_{ev} = min[\varepsilon_i L_i / V_i] \tag{1.2}$$

Where L_i, V_i, and ε_i are the characteristic slip distance, current slip velocity, and a prescribed parameter for ith cell respectively. ε_i depends on the constitutive friction law and stability considerations. In case of Dieterich-Ruina rate-and-state friction law (Dieterich, 1972)

$$\varepsilon_i = min\left\{\frac{A_i}{kL_i-(B_i-A_i)}, \frac{1}{2}\right\} \tag{1.3}$$

if $\chi_i > 0$ and

$$\varepsilon_i = min\left\{1 - \frac{B_i-A_i}{kL_i}, \frac{1}{2}\right\} \tag{1.4}$$

if $\chi_i < 0$, where

$$\chi_i = \frac{1}{4}\left(\frac{kL_i}{A_i} - \frac{B_i-A_i}{A_i}\right)^2 - \frac{kL_i}{A_i} \tag{1.5}$$

where i denotes element, A and B denote $a \cdot \sigma$ and $b \cdot \sigma$ respectively, and k is the single-cell stiffness, $\gamma G/h$. Here γ is a model-dependent constant, of order unity. Thus, temporal resolution directly depends on spatial resolution.

Implementing given technique into crustal strike-slip fault model with depth-dependent frictional parameters on interface results in sequence of rapid earthquake failures (Figure 1.1).

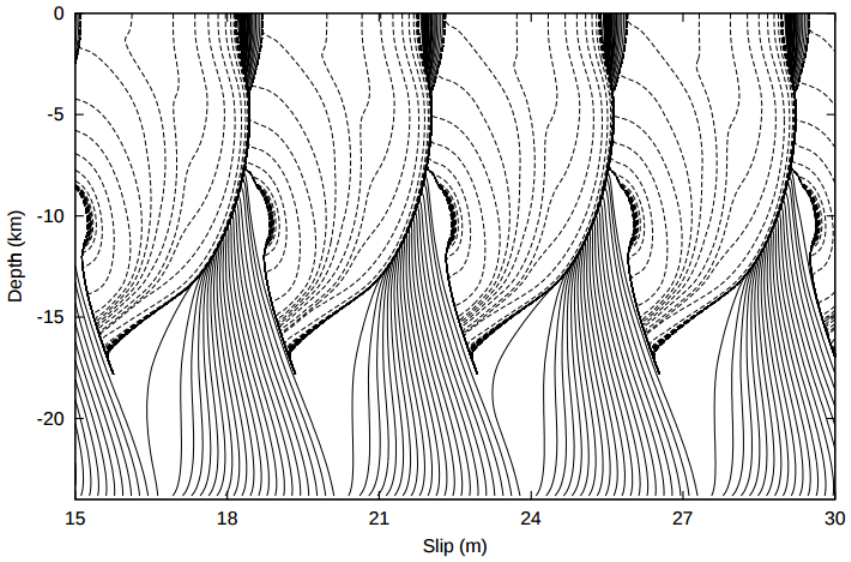

Figure 1.1 Accumulation of slip versus depth for the case $h^* = 0.94\ km$. The solid lines are plotted every 5 years. The dashed lines are plotted above 18 km depth every second if the maximum velocity anywhere on the fault exceeds 0.001 m/s. The model response consists of large, essentially periodic events rupturing the whole fault. From Lapusta et al., 2000.

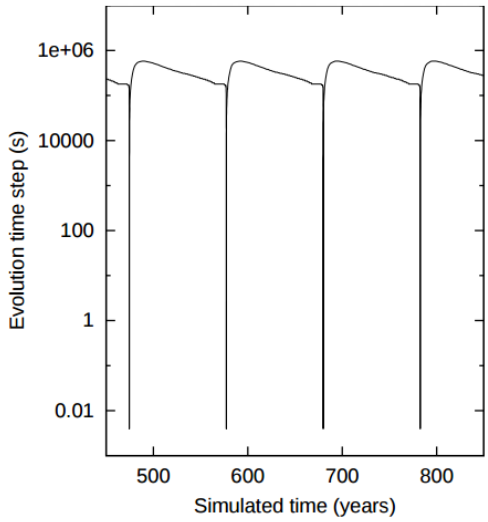

Figure 1.2 Values of evolution time steps (in seconds) plotted as a function of time in years.

For the slow deformation periods in between dynamic rupture events, the time steps taken are quite large (weeks). Within this technique variations of time steps may span more than 8 orders of magnitude (Figure 1.2).

Tests (Figure 1.3) had shown that spatial resolution should be at least about 40 times bigger than critical size of element (equation 1.1). Models with grid resolution $\eta = \frac{h^*}{h} \geq 40$ show the same results, while the resolution $\eta < 40$ is less sufficiently resolved.

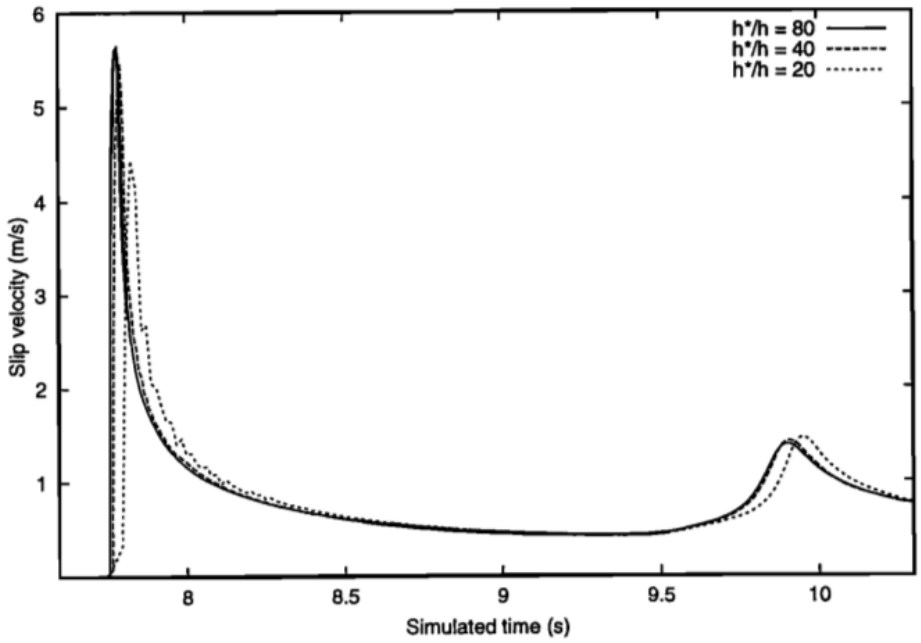

Figure 1.3 Slip velocity history at 3 km depth as a function of time for the second event in the sequence with h^*=0.94 km. Zero time is chosen arbitrarily for plotting convenience. The resolution h^*/h=40 gives essentially the same results as h^*/h=80. The case h^*/h=20 is less sufficiently resolved. From Lapusta et al., 2000.

Unlike the case with sufficient grid discretization η=40 (Figure 1.4a) and required time step criteria, case with two times smaller time discretization (Figure 1.4b) demonstrates that numerical instabilities start to occur at slow sliding velocities. While for the case with five times smaller time discretization (Figure 1.4c) response looks very complex, with numerous events of different maximum velocities, which is actually just a numerical artifact.

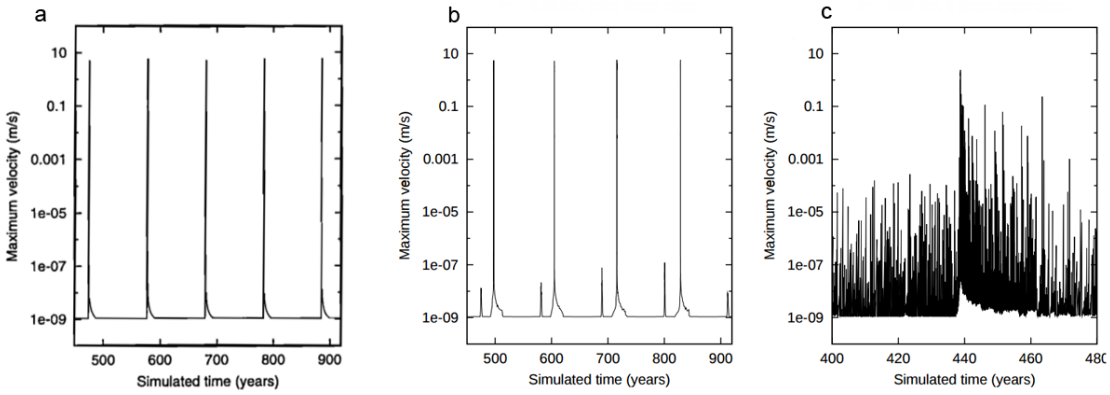

Figure 1.4 Maximum velocity on the fault as a function of time for a model with sufficient spatial resolution. (a) Original time step criteria, (b) ε_i increased by a factor of 2, and (c) ε_i increased by a factor of 5. From Lapusta et al. (2000).

Method of Lapusta et al. (2000) resolve all details of the break out of rupture, its propagation and arrest, and the transient afterslip postseismic slippage that develops. Earlier versions of this methodology were briefly outlined and implemented by Zheng et al. (1995), Rice and Ben-Zion (1996), and Ben-Zion and Rice (1997).

Drawbacks of this approach is the lack of viscous rheology, free surface on the top of the model and inability of using nonflat interfaces for faults which makes usage of this method quite limited.

While being very powerful in explaining of many features of rupture nucleation, propagation, and arrest, the method of Lapusta is extremely computational expensive. A simplified solution were performed by Rice (1993). His method uses quasi-static elasticity (i. e. the "quasidynamic approximation") instead of elastodynamic and is capable to approximate reproduction of the rupture propagation and slip velocities as in the proper dynamic simulation. Advantage of this approach is in relatively small spatial resolution ($\frac{h^*}{h} < 10$) and moderate criteria for time resolution: $\varepsilon = 1$ in equations 1.3 and 1.4.

1.1.2 Modeling of Viscoelastic Postseismic Relaxation

All the methods mentioned above are aimed to resolve nucleation, propagation and rupture arrest and entirely focus on mechanics of rate and state behavior in the brittle domain. They do ignore deformations occurring in the viscous part of the mantle. However, modelling of postseismic deformations after large earthquakes cannot avoid modeling postseismic relaxation not only due to the afterslip but also due to the viscoelastic relaxation which takes place in the upper mantle and lower crust.

Usually, the two rheological models are used for resolving of viscoelastic deformation - Maxwell's fluid and Burger's body.

Maxwell's rheology can be illustrated with Maxwell's fluid (Figure 1.5) which consists of viscous damper with viscosity η and a pure elastic spring with elastic modulus E connected in series.

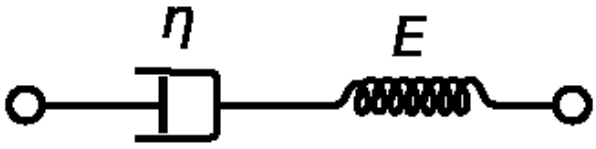

Figure 1.5 Maxwell's fluid.

Under applied axial stress total strain is defined as a sum of elastic strain and viscous strain, and total stress equals to the stress on each element:

$$\sigma_{Tot} = \sigma_D = \sigma_S \tag{1.6}$$

$$\varepsilon_{Tot} = \varepsilon_D + \varepsilon_S \tag{1.7}$$

Where subscripts D and S stay for damper and spring, respectively. Taking the derivative of strain with respect to time, we obtain strain evolution law:

$$\frac{d\varepsilon_{Tot}}{dt} = \frac{d\varepsilon_D}{dt} + \frac{d\varepsilon_S}{dt} = \frac{\sigma}{\eta} + \frac{1}{E}\frac{d\sigma}{dt} \tag{1.8}$$

Connecting viscous damper with elastic spring in parallel will make a Kelvin-Voigt solid (Figure 1.6).

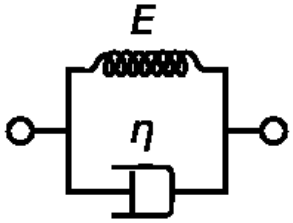

Figure 1.6 Kelvin-Voigt material

Since materials connected in parallel they have equal deformations and total stress equals the sum of stresses on elements:

$$\sigma_{Tot} = \sigma_D + \sigma_S \tag{1.9}$$

$$\varepsilon_{Tot} = \varepsilon_D = \varepsilon_S \tag{1.10}$$

From equations above we obtain rate of change of stress with respect to time:

$$\sigma(t) = E\varepsilon(t) + \eta \frac{d\varepsilon(t)}{dt} \tag{1.11}$$

In case of a suddenly applied stress (e.g. during an earthquake), deformations would approach the deformation for the elastic body σ/E which will decay exponentially:

$$\varepsilon(t) = \frac{\sigma}{E}\left(1 - e^{-\lambda t}\right) \tag{1.12}$$

where t is time, and $\lambda = \frac{E}{\eta}$ is rate of relaxation.

Combining these two materials in series results in Burgers body (Figure 1.7) which also can be called biviscous Burger's body. This rheology considers two different viscosities and different shear modulus which results in two different relaxation patches in time.

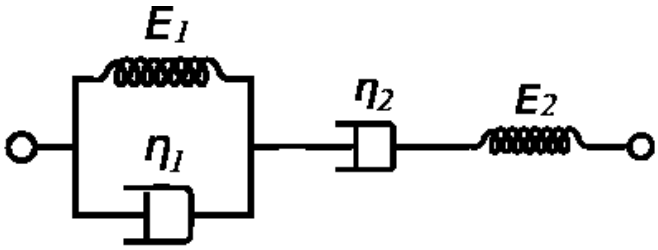

Figure 1.7 Burger's Body.

Deformation mechanisms operating in a rock and determining its constitutive behavior depend on phase content, chemical composition, and various thermodynamic variables (Burgmann and Dresen, 2008). Experimental data from wide range of conditions are well fit with following constitutive equation:

$$\dot{\varepsilon} = A\sigma^n e^{\left(-\frac{Q}{RT}\right)} \tag{1.13}$$

Where A is a material constant, σ is the stress, n is the power-law stress exponent, Q is the activation energy, T is the temperature, and R is the molar gas constant. When stress exponent n equals 1 viscosity is considered as linear and nonlinear when n>1.

Despite Maxwell's approximation with linear viscosity is useful to fit postseismic deformations after large earthquakes (Hu et al, 2004; Suito and Freymueller, 2009) this approximation is valid only after some years after earthquakes. Using precise instrumental

observations GPS and InSAR, Pollitz (2003) had shown that postseismic deformations during the first 2.5 years after an earthquake cannot be explained by Maxwell's linear viscosity fluid but, instead, can be well explained with transient rheology, in particular, with linear bi-viscous rheology. Thus, Burger's body can explain two modes of viscosity which can be observed after large earthquakes.

Later laboratory, geodesy and field observations (Burgmann and Dresen, 2008; Freed et al, 2010) shown the necessity of transient rheology with two modes of relaxation and power-law dependency between viscosity and stress.

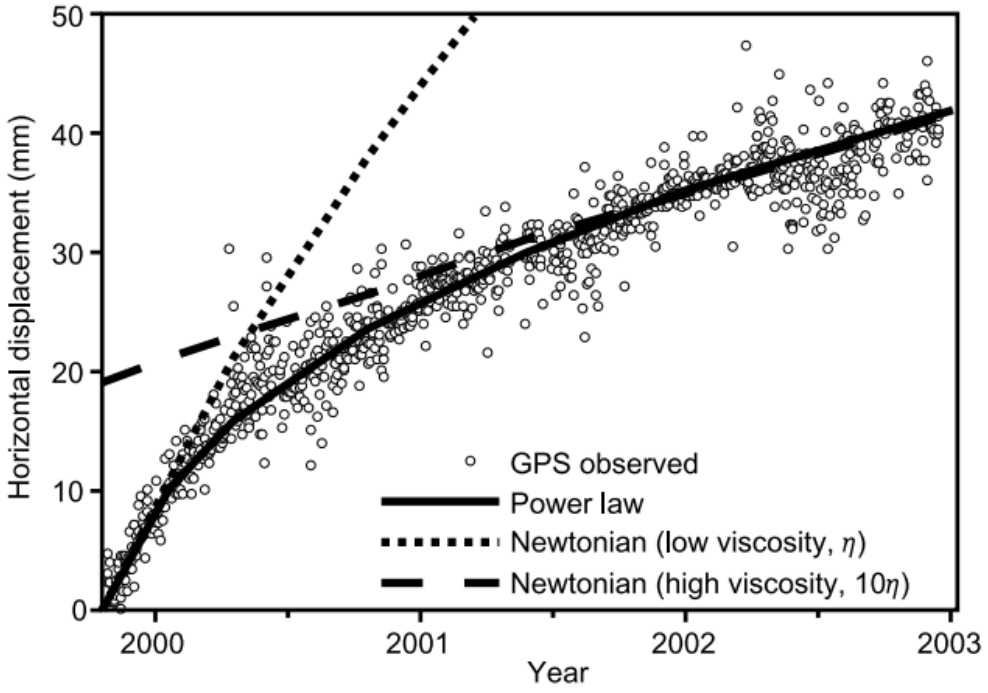

Figure 1.8 Comparison of representative observed and calculated postseismic displacement time series(station OPCX following the Hector Mine earthquake). Power-law mantle flow model (solid curve). Newtonian models consider predominately mantle flow with low viscosity ($2.5 \cdot 10^{18}$ Pa s, dotted curve) and an order of magnitude higher viscosity ($2.5 \cdot 10^{19}$ Pa s, dashed curve) that match early and late time-series slopes, respectevely. The curve associated with the high-viscosity newtonian model has been raised to show where the slope matches the observed time series. From Freed and Burgmann (2004).

One of the first attempts to explain postseismic deformations following large earthquake via modelling with a power law rheology was performed by Nur and Mavko (1974). Then Freed and Burgmann (2004) (Figure 1.8) used Maxwell's approximation for the upper mantle to show that power law rheology with $n=3.5$ can successfully explain spatial

and temporal evolution of surface deformation following large earthquakes. Their findings are consistent with laboratory experiments with wet olivine – likely the most abundant mineral in the upper mantle bellow lithosphere.

Currently modelling of power law rheology is quite complex problem in numerical simulation due to numerical instabilities related to strong sensitivity to stress change.

1.1.3 Modelling of Seismic Cycles

Since recurrence time of giant earthquakes can be estimated in centuries, many questions arise about their nature and mechanics. What are the necessary conditions for giant earthquakes? What is the mechanism of preparation of an earthquake? What amount of accumulated elastic deformations is necessary? What can trigger earthquake and so on. One of the way to answer these questions is to model seismic cycles in self-consistent way.

The seismic cycles at strike-slip faults have been modeled using generic elastic models in the studies which we mentioned above (Rice (1993), Rice and Ben-Zion (1996), Ben-Zion and Rice (1997), Lapusta et al (2000) etc.)

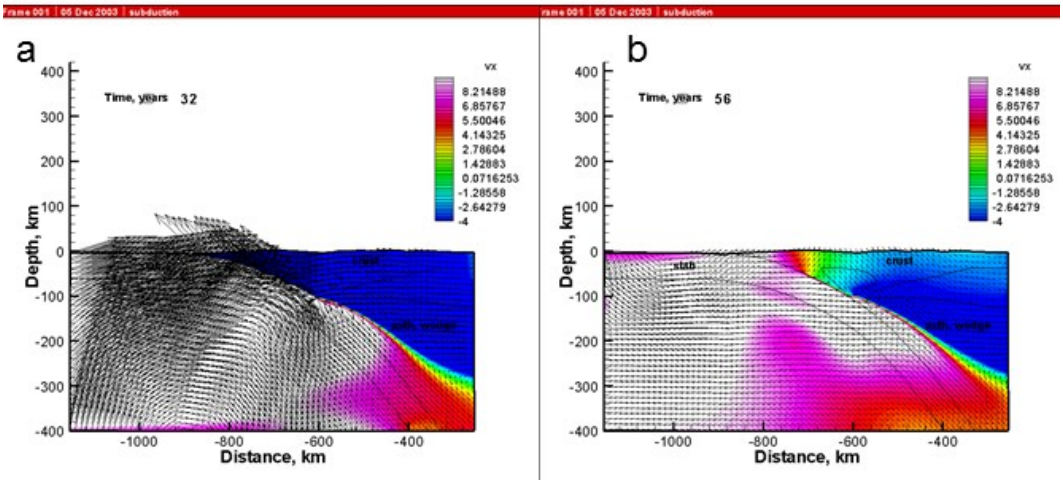

Figure 1.9 Model of subduction zone seismic cyclce by Sobolev and Babeyko (unpublished work from 2003, provided by S. Sobolev) (a) snapshot of velocity distribution during seismic event, (b) snapshot of velocity distribution during locking event.

Perhaps the first attempt to model subduction zones seismic cycles with realistic visco-elasto-plastic rheology was performed by Sobolev and Babeyko (2004 and unpublished data) (Figure 1.9). They have used model similar to their long-term geodynamic model of Cenozoic subduction orogeny in Central Andes (Sobolev and Babeyko, 2005) as an initial setup for the modeling of seismic cycles. The model included elasticity, non-linear, temperature and stress

dependent viscous rheology, Drucker-Prager plasticity and true free surface. They also implemented steady state version of the rate and state friction law at the interface between the plates and run the model for several 100 years. The example of the velocity distribution in their model is shown in Figure 1.9.

However, they did not manage to fully stabilize their solution with the rate and state friction and small time steps with the code available at that time. In the present study we are following their approach but with much more advanced modeling technique.

Another attempt to model the seismic cycle in viscoelastoplastic media was performed by van Dinther et al. (2013). For this purpose, they have developed a 2-D, continuum, visco-elasto-plastic numerical code. Model uses finite difference method on a fully staggered Eulerian grid in combination with a Langrangian marker-in-cell technique. Method includes stress- and temperature-dependent viscous flow. The momentum equations include the inertial term. Time step equals to 5 years. This study explores quasi-static seismic cycle model that includes Drucker-Prager plasticity with following rate-weakening friction law:

$$\mu = \mu_s(1-\gamma) + \mu_s \frac{\gamma}{1+\frac{V}{V_c}} \tag{1.14}$$

where γ denotes the amount of rate-induced weakening equivalent to $1 - \mu_d/\mu_s$, V denotes velocity, V_c denotes characteristic slip velocity. μ_s and μ_d are the static and minimal dynamic friction coefficients.

Figure 1.10 exemplifies van Dinther (2013) model setup and evolution. The model setup mimics the 2D projection of the trench-normal section in Southern Chile. Subduction slab of age 40 Ma was driven at velocity of 7.5 cm/yr under the overriding continental plate. This movement has produced corresponding distribution of stresses and temperatures.

Free-slip mechanical boundary condition acts at the top and side boundaries and sticky-air technique allows to simulate free surface at the top boundary. The lower boundary is vertically penetrable and assumes external free slip is satisfied at the depth of 500 km (Gorczyk et al., 2007). The resulting quasi-periodic pattern of quasi-characteristic *M*8-*M*9 megathrust events compares quantitavely well with the observed recurrence. Surface displacement during earthquakes agree with GPS observations for 2010 *M*8.8 Maule earthquake (Figure 1.11).

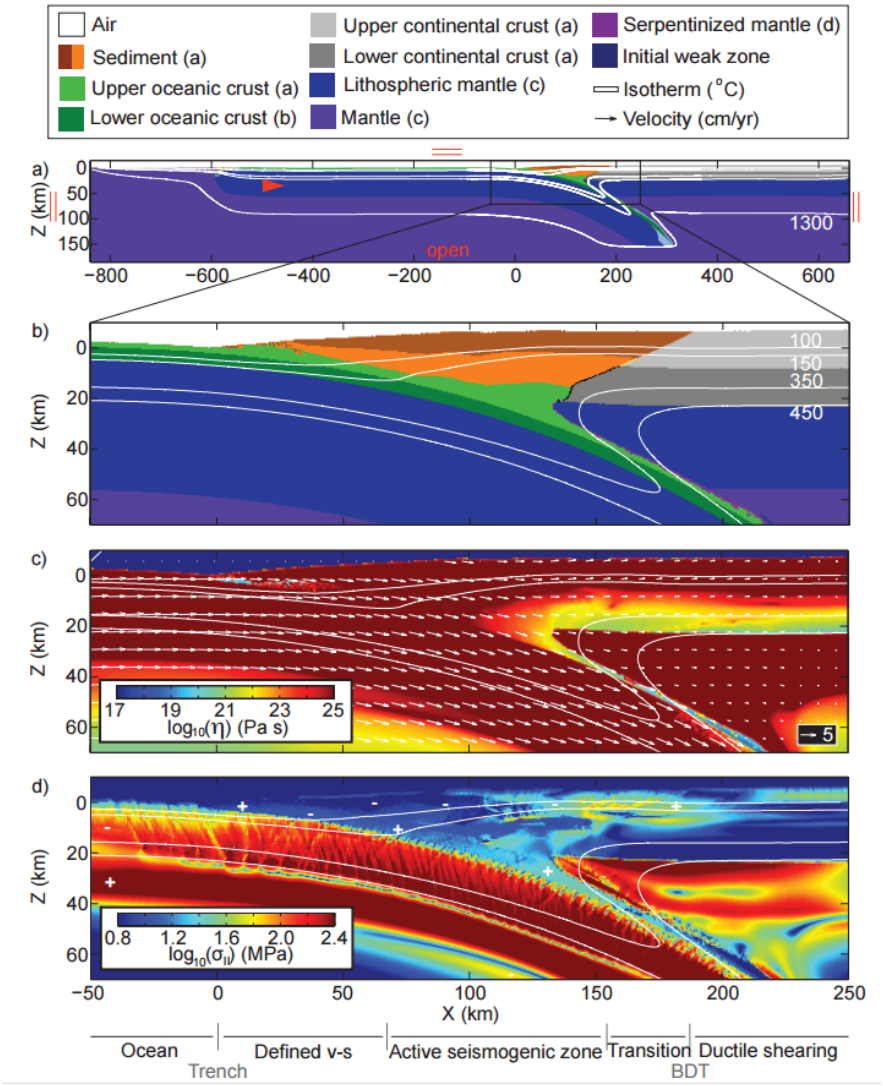

Figure 1.10 Initial model configuration after ~5.1 My of subduction, depicting rock compositions (colors) and isotherms (white contours) both for (a) entire model domain, including mechanical boundary conditions (red), and (b) for a zoom of the region of interest, for which (c) effective viscosities and (d) second invariant deviatoric stresses are depicted as well. Parenthesis in legend indicate the depicted flow law; a=wet quartzite, b=plagioclase, c=dry olivine, d=antigorite. Interseismic locking regions are apparent from white velocity arrows in c). Bottom figurations clarify different characteristic regions on the thrust ('v-s' = velocity strengthening friction, 'BDT' = brittle-ductile transition; van Dinther et al. (2013)). X is distance landward from the trench, Z is depth below the trench. White "+" and "-" indicate regions with horizontal extension and compression ,respectively. From Y. van Dinther et al., 2014.

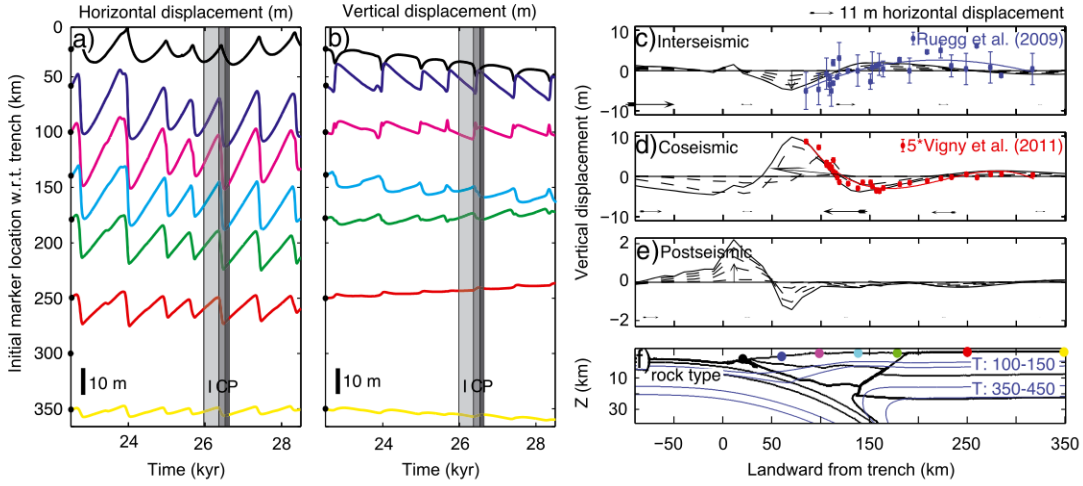

Figure 1.11 Surface displacements both depicted in time, (a) in horizontal (+ = landward) and (b) vertical (+ = upward) directions, and in space, as accumulated vertically (dashed lines are intermediates; solid line is total) and horizontally (arrows show total) during the (c) interseismic (I), (d) coseismic (C), and (e) 110 yr postseismic (P) period of the reference event. In Figures a and b displacements are ordered according to distance to the trench but show displacements in meters according to the inset. Figures c and d are overlain by GPS data points obtained in Southern Chile between 35°S and 37.5°S with respect to a stable South America for the interseismic period (blue: Ruegg et al. [2009]; extrapolated to 390 yr assuming constant locking) and 2010 M8.8 Maule earthquake (red: Vigny et al. [2011]). The line colors in Figures a and b correspond to different locations shown as colored circles in figure f. From van Dinther et al., 2013.

The model of van Dinther (2013) demonstrated feedback between long-term subduction dynamics and short-term seismogenesis. It also includes the three key ingredients for seismic cycle modelling in subduction zones: rate-dependent friction, slow tectonic loading and viscoelastic postseismic relaxation. Nevertheless, one can also mention the two serious drawbacks. First, van Dinther (2013) employed rate-dependent friction law which cannot represent natural behavior of rocks. Especially absence of state parameter in friction. Second, usage of constant time step value of 5 years is not consistent with the natural time scale of earthquakes of minutes. Moreover, this large time step does not allow modeling postseismic relaxation in its full temporal resolution.

Liu and Rice (2007) employed the technique of Lapusta et al. (2000) mentioned above for seismic cycle modeling. Since the method of Lapusta et al. (2000) is able to resolve rupture nucleation and propagation, Liu and Rice (2007), studied effects of different parameters on the slip regimes on the fault. In this research they had shown how non-dimensional parameter $\frac{W}{h^*}$, where W denotes seismogenic width and h^* is critical cell size from equation 1.1, controls

regime of sliding in subduction zone: interchange between seismic and aseismic regimes (Figure 1.12).

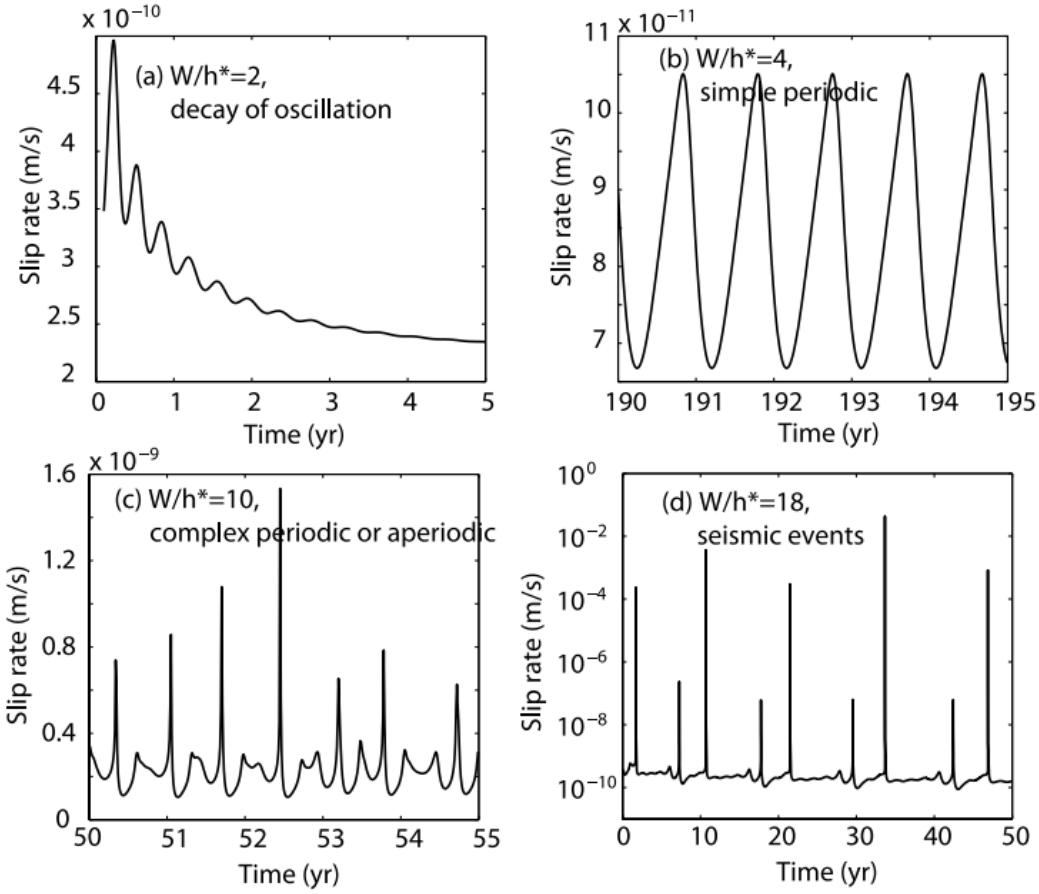

Figure 1.12. Slip rate at the bottom of seismogenic zone for different response patterns with increasing W/h^*: (a) $W/h^*=2$, oscillatory decay, (b) $W/h^*=4$, simple periodic, (c) $W/h^*=10$, complex periodic or aperiodic, and (d) $W/h^*=18$, seismic response. From Liu and Rice, 2007.

Varying seismogenic zone width *W,* effective normal stress on interface of fault $\bar{\sigma}$, and characteristic slip distance *L* and keeping ratio W/h^* constant, they obtained the same behavior of slip for different W/h^*. Similar approach was used in other studies (Veedu and Barbot, 2016; Cubas et al, 2016) to investigate necessary conditions for natural seismic cycles in specific areas. A shortcoming of this modeling approach is the neglecting of viscous behavior of lower crust and upper mantle which definitely affects parameters of seismic cycles. Moreover, the method relies on flat interfaces only which also limits its application to the natural examples.

1.1.4 Summary

Method of Lapusta et al., 2000 resolve details of the nucleation of rupture, its propagation and arrest, and the transient afterslip postseismic slip. But serious drawbacks of this approach is the lack of viscous rheology, free surface on the top of the model and inability of using non-flat interfaces for faults which makes use of this method quite limited. Also, this method is extremely computational expensive.

Deformation mechanisms operating in a rock and determining its constitutive behavior during postseismic relaxation depend on phase content, chemical composition, and various thermodynamic variables (Burgmann and Dresen, 2008). Experimental data from wide range of conditions are well fit with following constitutive equation 1.13 of power-law rheology. Despite Maxwell's approximation with linear viscosity has a very good fit to postseismic deformations after large earthquakes (Hu et al, 2004; Suito and Freymueller, 2009) this approximation is useful only after some years after earthquakes. Freed and Burgmann, 2004 used Maxwell's approximation for the upper mantle to show that power law rheology with n=3.5 can successfully explain spatial and temporal evolution of surface deformation following large earthquakes. Their findings are consistent with laboratory experiments with wet olivine – the most abundant mineral in the upper mantle. Later laboratory, geodesy and field observations (Burgmann and Dresen, 2008; Freed et al, 2010) shown the necessity of transient rheology with two modes of relaxation and power-law dependency between viscosity and stress.

The first approach to model the seismic cycle in viscoelastoplastic media was suggested by Sobolev and Babeyko (2004) but was for the first time fully realized by Y. van Dinther et al., 2013.The model of van Dinther (2013) demonstrated feedback between long-term subduction dynamics and short-term seismogenesis. It also includes the three key ingredients for seismic cycle modelling in subduction zones: rate-dependent friction, slow tectonic loading and viscoelastic postseismic relaxation. Nevertheless, one can also mention the two serious drawbacks. Employed rate-dependent friction law which cannot represent natural behavior of rocks. Also, usage of constant time step value of 5 years is inconsistent with the natural temporal scale of the earthquakes and does not allow modeling of postseismic relaxation in its full temporal resolution.

1.2 SLIM 3D

1.2.1 Numerical Modeling Techniques

Here, the focus lies on the numerical tool SLIM3D – Semi-Lagrangian Implicit Model for 3 Dimensions. While we do this in a rather brief way, an in-depth description of SLIM3D and benchmark demonstrations can be found in Popov and Sobolev (2008). SLIM3D is a coupled thermo-mechanical, finite-element, particle in cell code. As an advantage, it allows for realistic elasto-visco-plastic rheology, a free surface and diffusion, dislocation and Peierls creep mechanisms. In the following sections, we describe the properties of the underlying physical model which involves the constitutive equations as well as details of their numerical implementation scheme in SLIM3D. Furthermore, the capabilities of SLIM3D are shown in examples of previous studies done with this code. Finally, we describe the extensions and improvements added in scope of this work.

1.2.2 Physical Model

The outer shell of our planet is the lithosphere which exhibits elastic, viscous and brittle properties (Burov, 2011). Elasticity is an instantaneous and recoverable type of deformation and occurs in the upper part of lithosphere for instance during bending of slabs in subduction zones. Finally this type of deformation is responsible for accumulating of strain which is released then during earthquakes. High temperatures enable viscous deformation which can be observed in the asthenosphere and subduction channel. Brittle deformation is active in cold regimes, when stresses are high and failure of rocks occurs.

At low stress and temperature levels rocks behave elastically. The principles of elasticity are based on Hooke's law (Landau and Lifshitz, 1986) – named after Robert Hooks (1635–1703). This law states that the stress is proportional to the strain in the medium. As a consequence, one can write the strain rate $\dot{\varepsilon}^{elastic}$ as follows:

$$\dot{\varepsilon}^{elastic} = \frac{1}{2G}\dot{t} \tag{1.15}$$

where $\dot{t}$ is the objective stress rate and G is the elastic strain modulus.

Viscosity is highly nonlinear and depends on temperature, pressure, stress and the rheological properties of the involved material. Following the approach of Kameyama et al. (1999), we divide the solid state viscous flow itself into three types: diffusion, dislocation and Peierls creep.

These mechanisms are modeled as Arrhenius type of equations, based on empirical observations and results of high pressure experiments (e.g. Rybacki and Dresen, 2000). Each of the three mechanisms is dominating in a different pressure – temperature regime as

displayed in Figure 1.13. Diffusion and dislocation creep occurs at high temperatures (above $\sim 0.5T_m$ – where T_m is melting temperature) making them the main mechanism for high temperature deformation. In contrary, Peierls creep is active at low temperatures ($< 0.3T_m$) and high stress (Kameyama et al., 1999).

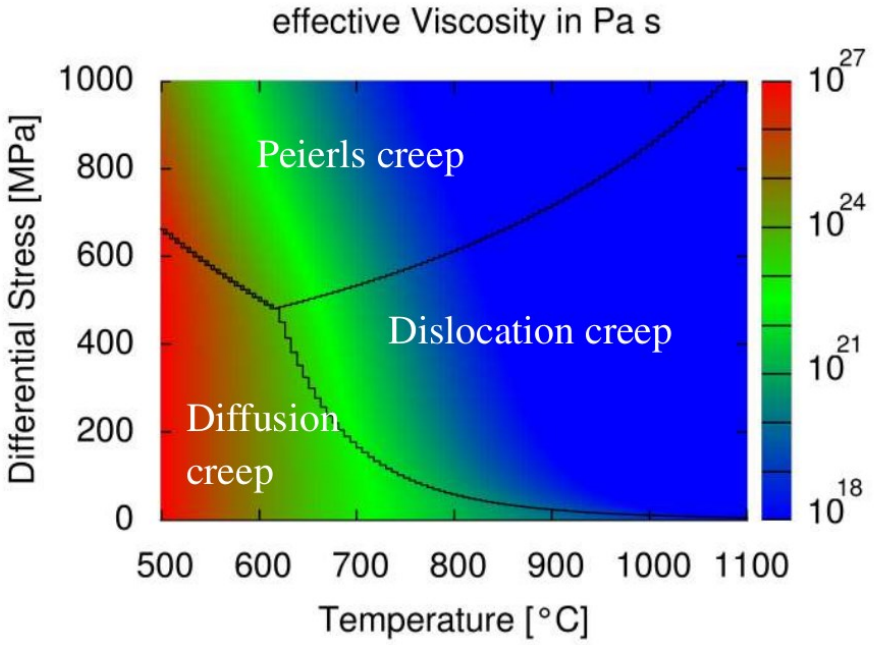

Figure 1.13 Logarithm of effective viscosity for dry olivine depending on differential stress and temperature in Pa s as calculated by SLIM3D. Black lines separate the regions of dominating deformation mechanism.

Strain rate for diffusion creep is linearly depended on stress – hence we use the subscript L. Also it decreases with grain size. To simplify this rheology, we assume that grain size is constant and hence imply its effect into the creep parameter B_L. Thereby the strain rate for diffusion creep is

$$\dot{\varepsilon}_L = B_L \cdot \tau_{II} \cdot exp\left(-\frac{E_L - pV_L}{RT}\right) \tag{1.16}$$

where $\tau_{II} = \left({}^{1}/_{2}\,\tau_{ij}\tau_{ji}\right)^{\frac{1}{2}}$ being the second invariant of the effective differential stress. E_L and V_L are the activation energy and volume, respectively, T denotes temperature, p pressure and R is the universal gas constant.

Dislocation creep component of the strain rate depends highly non-linearly on the stress – therefore we use the subscript N. The strain rate is proportional to the stress to the power n. Consequently, the mechanism is also known as power-law creep. We have

$$\dot{\varepsilon}_N = B_N \cdot \tau_{II}^n \cdot exp\left(-\frac{E_N - pV_N}{RT}\right) \tag{1.17}$$

where E_N and V_N are the activation energy and volume, respectively and n is the power law constant ($n = 3{\sim}3.5$) (Kameyama et al., 1999).

Peierls creep is also called low temperature plasticity – therefore we use the subscript P. SLIM3D uses the asymptotic approximation after Kameyama et al. (1999) with the strain

$$\dot{\varepsilon}_P = B_P \cdot exp\left(-\frac{E_P \cdot (1-\beta)^2}{RT}\right) \cdot \left(\frac{\tau_{II}}{\beta \tau_P}\right)^{2\beta(1-\beta)\cdot\frac{E_P}{RT}} \tag{1.18}$$

where, τ_P is the Peierls stress, E_P is the activation energy and β is the adjustable approximation parameter is set to β = 0.08.

Finally, the sum of all strain rates (equations 1.16, 1.17 and 1.18) provides the strain rate for the viscous deformation:

$$\dot{\varepsilon}^{viscous} = \dot{\varepsilon}_L + \dot{\varepsilon}_N + \dot{\varepsilon}_P \tag{1.19}$$

In order to calculate the effective viscosity for diffusion, dislocation and Peierls creep, SLIM3D follows the additive decompose approach by Kameyama et al. (1999). The effective creep viscosity η_{eff} is given by

$$\eta_{eff} = \frac{\tau_{II}}{2(\dot{\varepsilon}_L + \dot{\varepsilon}_N + \dot{\varepsilon}_P)} \tag{1.20}$$

Together with equation 1.19, we find for the viscous strain rate

$$\dot{\varepsilon}^{viscous} = \frac{1}{2\eta_{eff}}\tau \tag{1.21}$$

Brittle (or plastic) deformation is described by the standard Mohr–Coulomb plasticity model (see e.g. Vermeer (1990)). The model is named in honor of Charles-Augustin de Coulomb (1736–1806) and Christian Otto Mohr (1835–1918). The Mohr–Coulomb yield surface A is defined as

$$A = \frac{1}{2}(\sigma_{max} - \sigma_{min}) + \frac{1}{2}(\sigma_{max} + \sigma_{min}) \sin\varphi - c\cos\varphi \leq 0 \tag{1.22}$$

where, σ_{max} and σ_{min} are maximum and minimum principal stresses, φ is the material angle of friction and c denotes cohesion. The friction angle $\varphi = \varphi_0 D(\kappa)$ depends on the accumulated plastic strain κ through the piece-wise linear function $D(\kappa)$.

As a final step we model visco-elasto-brittle behavior of the lithosphere in SLIM3D with the approach from (Simo and Hughes, 2000). With equations 1.15, 1.21 and 1.22 the deviatoric strain rate is decomposed in its elastic, plastic and viscose components as follows:

$$\dot{\varepsilon}_{ij} = \dot{\varepsilon}_{ij}^{elastic} + \dot{\varepsilon}_{ij}^{viscous} + \dot{\varepsilon}_{ij}^{plastic} = \frac{1}{2G}\dot{\tau}_{ij} + \frac{1}{2\eta_{eff}}\tau_{ij} + \dot{\lambda}\frac{\partial Q}{\partial \tau_{ij}} \tag{1.23}$$

Here, $\dot{\lambda}$ is the plastic multiplier and the potential plastic function Q is given by $Q = \tau_{ij}$ in Prandtl-Reuss flow.

1.2.3 Constitutive Equations

Equations that describe the lithospheric-scale deformations are conservative laws for momentum, mass and energy. Lithospheric deformations characterized with relatively slow deformations so inertial forces can be ignored.

Assuming a continuous media approximation, stress gradients are balanced by gravity forces and the equation for conservation of momentum can be derived following the assumptions, that mass flux can only change due to transport and mass itself cannot be created or destroyed. Thus, we have

$$\frac{\partial \sigma_{ij}}{\partial x_j} + \rho g \hat{z}_i = 0 \tag{1.24}$$

where σ_{ij} is the Cauchy stress tensor, ρ denotes density, g is gravity and $\hat{z}_i$ is the unit vector of the vertical axis pointing downward. For the Cauchy stress tensor we may write the Cauchy stress deviator τ via $\sigma_{ij} = \tau_{ij} + p\delta_{ij}$ with $p = -\frac{1}{3}\sigma_{ii}$ being the hydrostatic pressure.

The presence of variation of stresses and temperatures with depth requires to deal with the density ρ as a function of pressure p and temperature T, i.e.,

$$\rho = \rho_0[1 - \alpha(T - T_0)] \cdot \left(1 + 4 \cdot \frac{p}{K}\right)^{\frac{1}{4}} \tag{1.25}$$

here, K denotes Bulk modulus, α is the thermal expansion coefficient and ρ_0 is the density of the reference temperature T_0.

The conservation equation of energy is derived from the first principle of thermodynamics. It relates temperature changes due to the generation of radiogenic heat H, with advective and conductive heat transport, i.e.,

$$\rho C_p \frac{DT}{Dt} = \frac{\partial}{\partial x_i}\left(\lambda \frac{\partial T}{\partial x_i}\right) + \tau_{ij}\dot{\varepsilon}_{ij} + \rho H \tag{1.26}$$

here, C_p and λ denote heat capacity and conductivity, respectively. The strain rate $\dot{\varepsilon}$ is given by equation 1.23.

SLIM3D includes the effects of elastic compressibility and thermo-elasticity. Thus, continuity equation can be conveniently coupled with constitutive equation for hydrostatic pressure:

$$\frac{1}{K}\frac{Dp}{Dt} - \alpha \frac{DT}{Dt} + \frac{\partial v_i}{\partial x_i} = 0 \tag{1.27}$$

here v being the velocity.

1.2.4 Algorithm in SLIM3D

In next paragraphs we pursue the aim to demonstrate the general principles of calculation scheme used in SLIM3D rather than give full explanation of code. Nevertheless adequate description can be found in Popov and Sobolev (2008), and Popov (2009).

The code is based on the finite element method (Hughes, 2012) and the Galerkin procedure (Belytschko et al., 2013). SLIM3D employs hexahedral finite elements with linear interpolation functions (e.g. Zienkiewicz and Tylor, 2000). Disadvantage of that linear scheme is the lack of stability of the mesh to artifacts (e.g. locking and hourglass). To exclude expensive quadratic interpolation, SLIM3D circumvents the issue by replacing material density with differential density. A Lagrangian–Eulerian kinematic formulation was chosen to account for material advection. A clear advantage of this method over pure Eulerian formulations is the possibility to keep track of free surfaces. Moreover, the Lagrangian method does not put a limit on the time step size. In order to solve the coupled system of discretized residual equations, the Newton–Raphson iterative method is applied. Furthermore, a particle-in-cell approach (e.g. Gerya and Yuen, 2007) confines spurious numerical diffusion.

Figure 1.14 represents the overall computational flowchart of SLIM3D. The algorithm can be divided in two recurring sections: “Newton-Raphson solution” and “Regridding and Remapping” – each with several necessary iterations. Initially, the temperature distribution inside the model is described via prescription of the thermal boundary layer (TBL). The TBL marks the Lithosphere-Asthenosphere transition at ~ 1350°C. SLIM3D then calculates a first steady state temperature distribution. In this step, radiogenic heat production, thermal diffusivity and the geometry of the material distribution are taken into account. Afterwards, the first Newton-Raphson cycle takes place. The most expensive part is here the solving of the linear system, which incorporates the constitutive equations and model assumptions stated

above. These steps are followed by “Regridding and Remapping”. At the end of “Regridding and Remapping”, the output files are generated for post processing. Finally, the time step is advanced and the procedure starts anew.

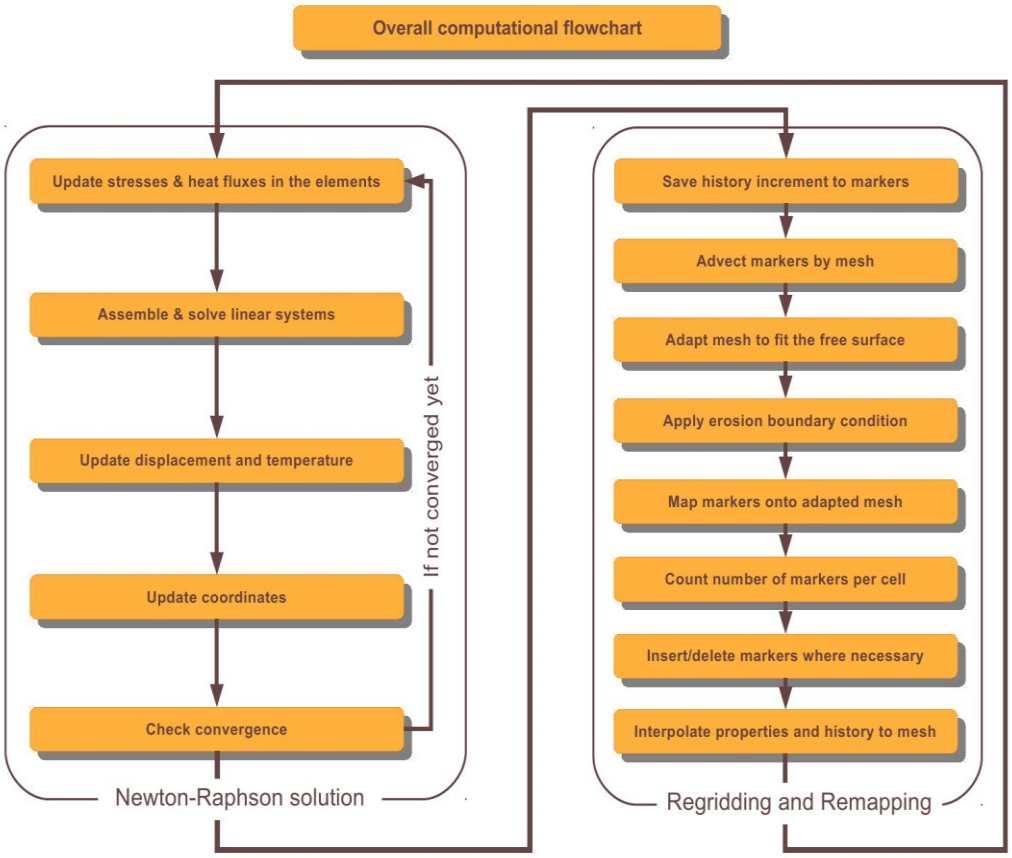

Figure 1.14 The overall computational flowchart of SLIM3D, (cf. Popov and Sobolev (2009)). In each step first the Newton-raphson solution is computed, then regridding and remapping takes place. From Tympel (2014).

1.2.5 Previous Modeling of Subduction in SLIM3D

SLIM3D was introduced and thoroughly described in Popov and Sobolev (2008). Five benchmark tests to verify the applicability of the adopted physical models and numerical techniques were performed: (i) bending of an elastic plate, (ii) sinking of a rigid cylinder in a viscous fluid, (iii) initiation of shear bands in the brittle crust, (iv) triaxial compression test and (v) lithospheric transpressional deformation. The first two tests are designed to test ability of the code handle elastic and viscous rheological mechanisms. (iii) and (iv) problems show

quasi-brittle elasto-plastic strain localization. And the final benchmark test demonstrates simulation of complete elasto-visco-plastic rheology. All simulations performed sufficient accuracy for practical applications.

Quinteros et al. (2010) applied SLIM3D to investigate effect of viscosity in transition zone and lower mantle on penetration of slab. There is no consensus about the viscosity in transition zone and shallower lower mantle. Hence, using a numerical self-consistent subduction model allows to find a characteristic viscosities which result in evolution of different subduction styles that can actually be found in nature.

Tympel and Sobolev (2011) employed SLIM3D to investigate Cenozoic lithospheric deformation in the Himalaya-Tibet-Pamir-Tien Shan orogen. In this study they model Pamir-Tien Shan mountain range, which hosts the Earth's most important active intra-continental subduction zone. Leading goal of the modeling is to find lithospheric scale models consistent with all major observations as well as to find controlling factors for the extreme Cenozoic shortening in the Pamir-tien Shan orogen.

Quinteros and Sobolev (2012a) used SLIM3D to mimic the subduction in the Marianas and try different blocking temperatures for the olivine/spinel transformation. Along with non-linear elasto-visco-plastic rheology based on laboratory data, model includes phase transformations, latent heat, proper coupling between stress and thermal state of the slab and force balance of the system. The calculations identified a blocking temperature for the olivine/spinel transformation of approximately 725°C. The inclusion of shear heating in the model was vital to mimic the subduction in Marianas.

Quinteros and Sobolev (2012b) employed SLIM2D in order to explain the rapid changes in the convergence rate (increase and then decrease) between the Nazca and south America plates during the past 25-20Myr. The simulation showed that slab penetration in the transition zone speed up the Nazca plate, while the negative Clapeyron slope at 660km depth results in the observed slow down. In contrary, the presence of the Andes does not significantly affect the convergence rate.

1.2.6 SLIM3D as Used in this Thesis

As it was mentioned in the previous part modeling of subduction processes was already performed in different studies. Perhaps first problem we were faced was design of the subduction with certain geometry and specific temperature profile. To do so, we managed lots of experiments to eventually make procedures in code which can control boundary conditions. Routines which helped as design different geometry setups described in the 2.1.1.

Originally code SLIM3D was design to simulate processes which take place in lithosphere and upper mantle in geological time scale. Thus, key difference between all previous applications of SLIM3D and our models is using large range of time scales (from 40 seconds to mln years). Abrupt change from geological time scale to seismic time scale requires

some additional procedures for stabilization of solution as well. Necessary procedures are described in the part Turning Model from Long-Term to Short-term.

In order to generate earthquakes we introduced rate-and-state friction law which affects the strength of material (Rheology Modification: Rate-and-State Friction Law). To resolve earthquakes and following postseismic processes in a proper way we included adaptive time step procedure (2.1.5). This procedure tracks rate of deformations in the subduction channel and changes time step according to average accelerations. Our technique recognizes moment of earthquakes on one hand and allows us to observe post seismic relaxation in details on the other hand.

Since we model post seismic relaxation with appropriate time resolution we had to modify dislocation creep viscosity to add transient rheology (2.1.3) which can occur during giant earthquakes.

Finally, after implementing a set of modifications in the code to model earthquakes we designed a script for collecting different statistical information about earthquakes and changes in our models (2.2.4). Procedure is able to recognize geometry of the rupture and then measure all necessary parameters (e.g. slip along the fault, stress drop, total displacement, seismic moment and so on). In cooperation with adaptive time step procedure this routine helps us tracking evolution of the slip at the fault with time.

1.3 Rate-and-State Friction Law

Since cause of earthquakes is the sudden release of elastic strain in the Earth's lithosphere, mechanism of accumulating and release of strain is the essential problem to study.

Earthquake mechanism is based on observations that tectonic earthquakes seldom occur by the sudden appearance and propagation of a new shear crack, but rather by sudden slip along a pre-existing fault or plate interface (Scholz, 1998). In consequence of this fact earthquakes are frictional, rather than fracture, phenomenon. In 1966 Brace and Byerlee referred earthquakes as stick-slip frictional instability. Hence earthquake is the "slip" and interseismic period is "stick". Afterwards, constitutive law of rock friction was derived from laboratory experiments. Nowadays there are a few different forms of rate-and-state friction laws which are used to model laboratory observations. In our study we use Dieterich-Ruina formulation (Dieterich, 1972) of rate-and-state friction law which is in best agreement with experimental data (Beeler et al, 1994).

1.3.1 Dieterich-Ruina Rate-and-State Friction Law

$$\tau = c + \mu \times \bar{\sigma} = c + \left[\mu_0 + a \times ln\left(\frac{V}{V_0}\right) + b \times ln\left(\frac{V_0\theta}{L}\right)\right] \times \bar{\sigma} \qquad (1.28)$$

$$\frac{d\theta}{dt} = 1 - \frac{V\theta}{L} \tag{1.29}$$

Where τ is shear stress, μ is friction, $\bar{\sigma}$ is effective normal stress (applied normal stress minus fluid pore pressure). V is the slip velocity, V_0 is reference velocity, μ_0 denotes steady-state (or base) friction at $V = V_0$, a and b are material properties and L is the critical slip distance. θ is the state parameter (often interpreted as average contact lifetime).

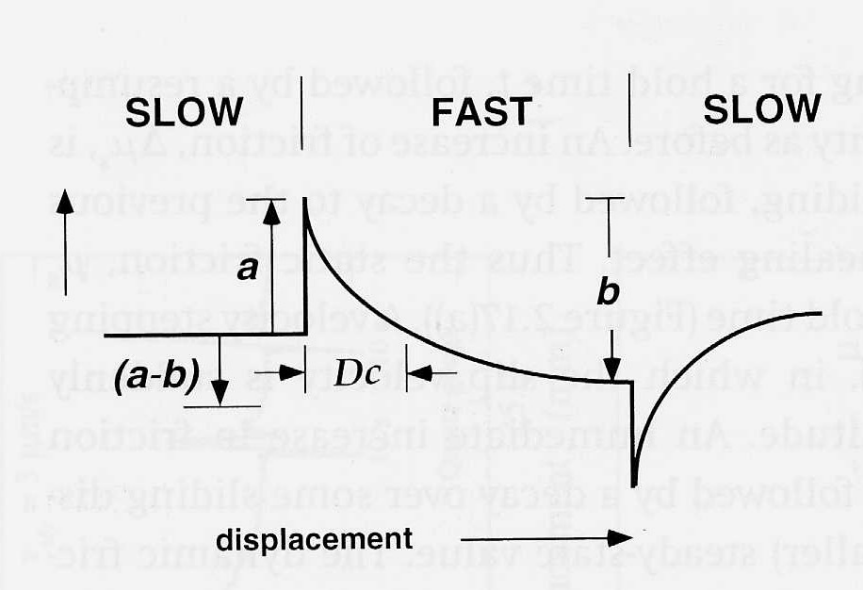

Figure 1.15 Frictional response to a suddenly imposed e-fold increase and then decrease in sliding velocity (from Scholz, 1998).

Just after initial application of slip friction raises by magnitude a. This is followed by exponential decay with magnitude b. Assuming friction at steady state, we obtain:

$$\tau = c + \left[\mu_0 + (a - b) \times ln\left(\frac{V}{V_0}\right)\right] \times \bar{\sigma} \tag{1.30}$$

1.3.2 Stability Regimes

Consider a classic experiment with a simple spring-slider. Where block produces normal stress $\bar{\sigma}$ with its weight, slider obeys rate-and-state friction law, spring has a stiffness k and undergoes pull τ (Figure 1.16).

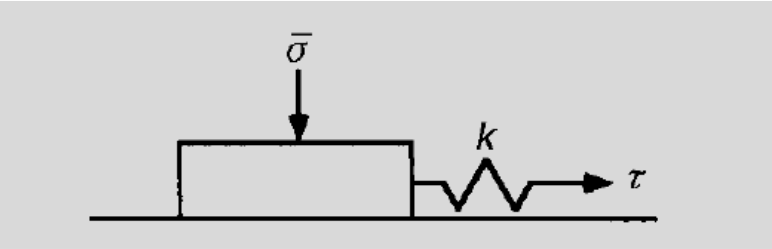

Figure 1.16 Regime of sliding entirely depends on $\bar{\sigma}$, τ, k, *rate-and-state parameters* $(a-b)$ *and L while completely indifferent to base friction* μ_0. *From Scholz (1998).*

In case of positive $(a-b)$ parameter we obtain velocity-strengthening behavior which is essentially stable. On the other hand, negative $(a-b)$ parameter may bring system to unstable state. Considering material parameters of the system constant the bifurcation occurs at a critical value of effective normal stress $\bar{\sigma}_c$:

$$\bar{\sigma}_c = \frac{kL}{-(a-b)} \tag{1.31}$$

If $\bar{\sigma} > \bar{\sigma}_c$ sliding is unstable under quasistatic loading. However in conditionally stable regime ($\bar{\sigma} < \bar{\sigma}_c$) unstable behavior can occur with the help of finite velocity kick or stress change. Following Walsh (1971), Dieterich et al. (1978) propose that for confined slip on the interface with size W the stiffness scales as $k = \frac{\eta G}{W}$ where G is the shear modulus and η is a geometric constant with value about 1, we can rewrite equation above as:

$$W_c = \frac{G\eta L}{(b-a)\bar{\sigma}} \tag{1.32}$$

This implies that instability regime occurs when the size of slider reaches critical size W_c.

1.3.3 Uncertainties and Problems of Rate-and-State Friction Law Applications

In spite of reliable results of numerous laboratory experiments with rocks there are still a lot of problems with application of rate-and-state model to real faults.

Firstly, full reproduction of stress, temperature and fluid pressure cannot be obtained in laboratory during tests. While experimental estimations for a and b match observations for real faults, important parameter L remains uncertain. In expereiments L is ~10μm, while various attempts to estimate its value for natural faults, assuming that it is a property of the contact interface of fault (Scholz, 1988) or the gouge zone thickness (Marone and Kilgore, 1993), suggest that it might be much larger in nature (cm or even up to one meter).

Another problem in modelling of earthquakes is the value of effective normal stress and its distribution at the faults. Different studies (Irwin and Barnes, 1975; Audet et al., 2009; Liu and Rice, 2007 etc) have shown big range of possible effective normal stresses in fault (from 1 MPa to 50 MPa). Therefore all these uncertainties complicate the modelling of real faults.

1.3.4 Introduction of Rate-and-State Rheology to SLIM3D

Since SLIM3D is finite elements method code with uniform mesh we cannot introduce interface with rate-and-state friction law. In our modelling we employ this law on markers, thus we have a layer with certain parameters. We then approximate velocity of slip V by shear strain rate of material in a finite element in subduction channel multiplied by the element size Δx:

$$V = \Delta x \cdot \dot{\varepsilon} \tag{1.33}$$

Normal stress σ_n is approximated by dynamic pressure (-I/3, where I is first invariant of stress tensor), in the same way as that has been done by van Dinther et al. (2013).

Substituting $\overline{\sigma_n} = \sigma_n - p_f$ into equation 1.28 and modifying it we obtain:

$$\mu\left(1 - \frac{P_f}{\sigma_n}\right) = \mu^* = \mu_{st}^* - (b-a)^* \cdot \ln\left(\frac{V}{V_{st}}\right) + b^* \cdot \ln(\frac{\Theta V}{L}) \tag{1.34}$$

$$\mu_{st}^* = \mu_{st}\left(1 - \frac{P_f}{\sigma_n}\right);\ (b-a)^* = (b-a)\left(1 - \frac{P_f}{\sigma_n}\right);\ b^* = b\left(1 - \frac{P_f}{\sigma_n}\right) \tag{1.35}$$

where τ is shear stress, c is cohesion, P_f is fluid pressure, σ_n is normal stress, μ, μ^* and μ_{st}^* are friction, effective friction and effective static friction respectively. $(b-a)$, b are parameters for rate and state friction law and $(b-a)^*$, b^* are effective parameters for rate and state friction law, V is velocity of slip on the fault, V_{st} is quasi-static (or reference) velocity i.e. the velocity at which $\mu^* = \mu_{st}^*$. L is the critical slip distance and Θ is the state variable.

Assuming that velocities are constant at any integration time-step, we can integrate state equation 1.29 and define an updated value of state parameter at the end of the time step (θ_{n+1}) through its value at the end of the previous time step (θ_n).

$$\theta_{n+1} = \frac{L}{V_{n+1}} + (\theta_n - \frac{L}{V_{n+1}}) \cdot \exp(-\frac{V_{n+1}\Delta t}{L}) \tag{1.36}$$

where θ_{n+1} and θ_n are state variables for current and previous time steps respectively, L is the critical slip distance, V_{n+1} is velocity of slip on the fault and Δt is the current time

step. Further, by substituting equation 1.36 in 1.34 we obtain the final relation for the effective friction and shear stress in the channel.

Chapter 2 Seismic Cycles Modeling

2.1 Preparing of the 2D Model

2.1.1 Long-Term Subduction Model

We use 2D version of thermomechanical finite element numerical code SLIM3D (Popov and Sobolev, 2008) that solves conservation equations of mass, momentum and energy. The technique employs non-linear rheology assuming that the cumulative strain rate is linear combination of elastic strain rate, viscous creep strain rate and plastic stain rate components. The steady-state creep parameters for diffusion and dislocation creep are determined by laboratory experiments with major rock types and all models have true free-slip upper boundary condition. The table with rheological parameters used in this study is presented in. The model is 2D, has horizontal dimension of 900 km and vertical (depth) dimension of 300 km. Finite element size in routine models is 3 km, but we have also tested models with 2 times lower resolution.

The model is aimed to reproduce lithospheric structure of the South Andes where the Great Chile Earthquake occurred in year 1960. It consists of oceanic subducting slab with the basaltic crust and harzburgitic lithospheric mantle; overriding plate with two-layer continental crust and lithospheric mantle and asthenospheric mantle. For the asthenospheric mantle we use olivine diffusion and dislocation creep parameters corresponding to the water content of 1000 ppm H/Si (Hirth and Kohlstedt, 2003). We consider as a “subduction channel” a top layer of the oceanic crust at the depth less than 100 km and prescribe to it a special type of rheology. This includes very low effective static friction coefficient of 0.015-0.02 in accord with the long-term evolution models of South Andes (Sobolev and Babeyko, 2005) and the weakest wet quartz dislocation creep rheology (Ranalli, 1997).

We “prepare” the long-term model by running the two-plates model for about 10 Mln years with the fixed no-slip upper 80 km of lithosphere at right (continental) boundary and rest of right boundary flow-open (Figure 2.1). Characteristic time step during subduction is 10 thousand years.

We generate subduction by advancing oceanic lithosphere in direction of continental lithosphere with the 30° dipping low-strength fault between oceanic and continental lithospheres like it is usually done in long-term subduction models. The bottom boundary is flow-open and left boundary is kinematicaly prescribed. Horizontal velocities at the upper 55

Table 1. Rheological parameters of the material phases.

Material	**ρ, (g/cm³)**	**K, kbar**	**G, Kbar**	**Log(B_d), (1/(Pa s))**	**E_d, (kJ/mol)**	**V_d, (cm³)**	**Log(B_n), (1/(Pa s))**	**E_n, (kJ/mol)**	**n**	**V_n, (cm³)**	**Log(B_p), (1/(Pa s))**	**E_p, (kJ/mol)**	**τ, MPa**	**μ_0**	**c, MPa**	**α, 10^{-5}/K**	**C_p, (kJ/(kg K))**	**k, (W/(m K))**	**A, (nW/kg)**
Subduction channel	3.270	1200	400	0	400	7	-17.3	154	2.3	0	0	223	5000	0.015	2.0	3.7	1.2	2.5	0.02
Oceanic crust	3.270	1200	400	0	400	7	-27.0	154	2.3	0	0	223	5000	0.5	2.0	3.7	1.2	2.5	0.02
Oceanic lithosphere	3.275	1220	740	-10.59	300	5	-15.2	530	3.5	13	11.76	515	8500	0.5	10.0	3.0	1.2	3.3	0
Upper continental crust	2.800	550	360	0	400	7	-28.0	223	4.0	0	0	223	5000	0.5	10.0	3.7	1.2	2.5	1.50
Lower continental crust	3.000	630	400	0	400	7	-14.75	356	3.0	0	0	445	5000	0.5	20.0	2.7	1.2	2.5	0.20
Continental lithosphere	3.300	1220	740	-10.59	300	5	-14.7	480	3.5	8	11.76	515	8500	0.5	2.0	3.0	1.2	3.3	0
Asthenosphere	3.330	1220	740	-10.59	300	5	-14.7	480	3.5	8	11.76	515	8500	0.5	10.0	3.0	1.2	3.3	0

km of the left boundary were fixed at 7 cm/yr. Velocities at the left boundary deeper than 55 km are chosen by trial and error to achieve geometry of the subducted slab consistent with the seismic observations (Dzierma, Y. et al., 2012).

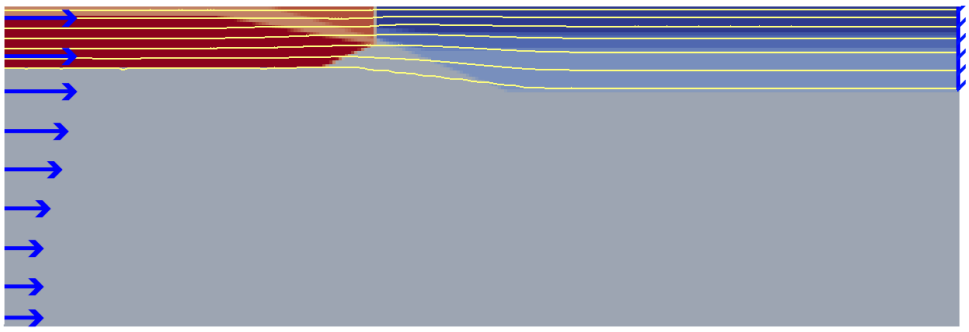

Figure 2.1 Initial setup of 2D model for Chile subduction zone at 38° latitude. Model has prescribed temperatures (yellow lines represent temperature in the range from 100°C to 1300°C every 200°C) depending on depth. Continental plate has a fixed velocity boundary till the depth of 80 km, rest of the right boundary and bottom boundary have a flow-open surface. Left boundary has a fixed kinematic condition with velocity of 7 cm/yr loading in upper 55 km, and decreased velocity till 2 cm/yr below.

The resulting long-term model is demonstrated in Figure 2.2-5. It has slab geometry consistent with the seismic data (Dzierma, Y. et al., 2012) and upper plate structure and temperature consistent with observations and previous thermal models (Currie and Hyndman, 2006). The resulting viscosity structure is strongly variable with the lowest viscosity slightly lower than 10^{18} Pa s in the asthenospheric mantle wedge.

During 10 My of subduction spatial distribution of temperature comes to appropriate static state. Importance of the creating subduction from the beginning lays in proper distribution of stress but not only temperature. Also we needed to obtain adequate velocities in every part of the model. As we got necessary state of the model we turned kinematic conditions on the left borders to free flow surface. At the same moment we fixed and recorded velocities at the right and bottom borders. Hence, in our limited by 300 km depth model subduction is controlled by pulling force, which is more natural behavior for subduction. The same result could be obtained by extending model's depth to at least transition depth (~660 km), to produce pulling force caused by negative buoyancy of sinking slab. But this approach is expensive in terms of calculating time and was refused.

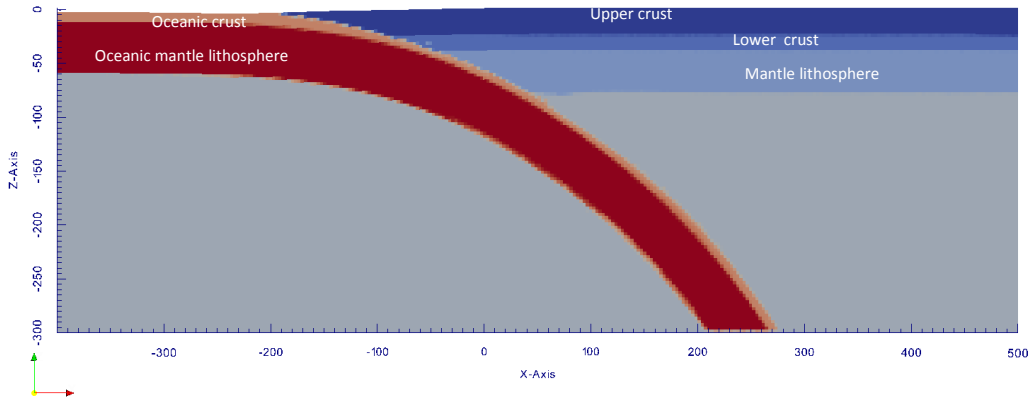

Figure 2.2 Resulting long-term model with spatial distribution of materials.

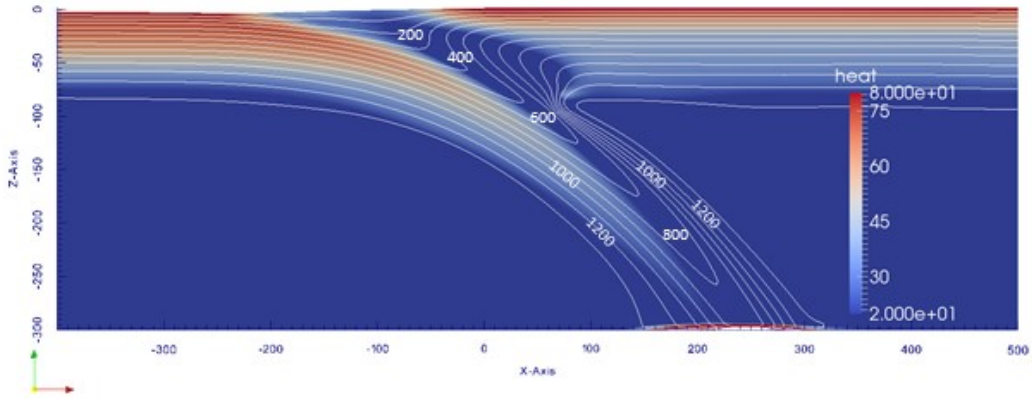

Figure 2.3 Resulting long-term model with spatial distribution of heat flow and temperatures.

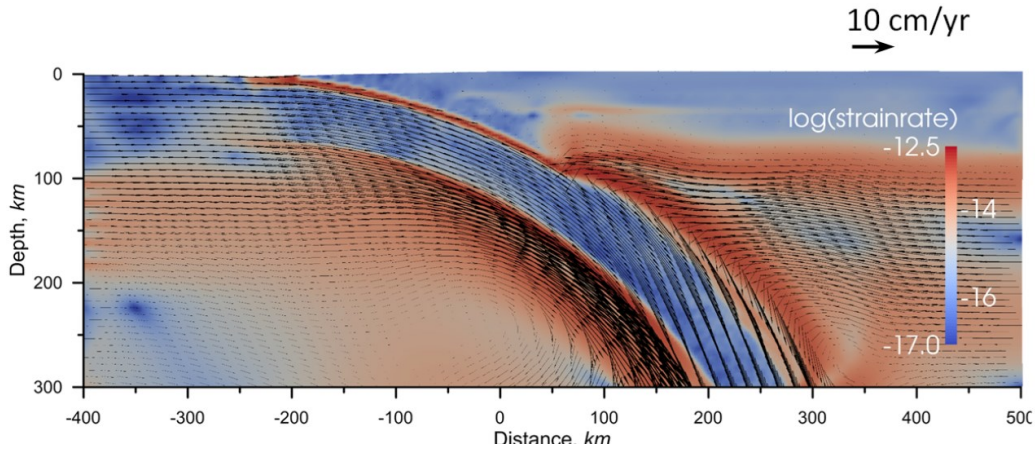

Figure 2.4 Resulting long-term model with spatial distribution of strain rates and velocities.

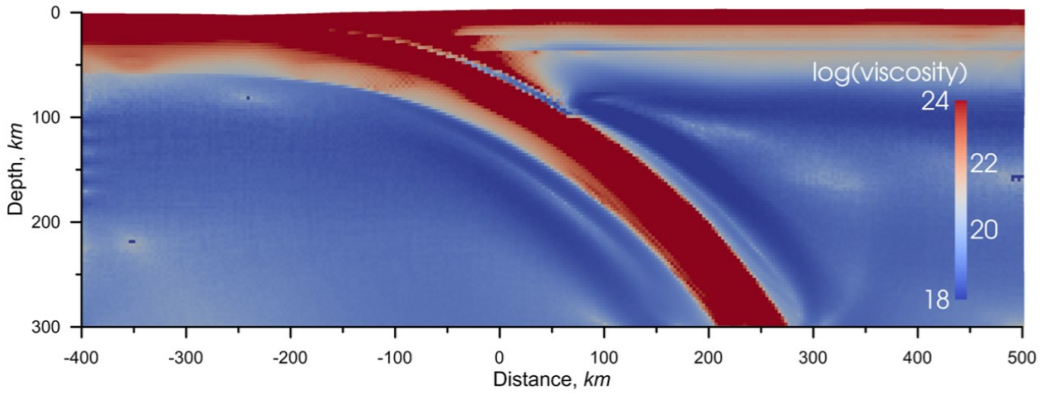

Figure 2.5 Resulting long-term model with spatial distribution of viscosity.

2.1.2 Turning Model from Long-Term to Short-Term

Unlike subduction, modeling of seismic cycles requires much smaller time steps. The long-term model was taken as an initial condition for the short-term model. Adaptation to small time-step of 5 years requires special procedure.

The typical integration time step in the long-term model is 10 thousand years, while the maximal time-step required for our short-term model is only few years, so the time step change of more than 1000 times is required. While in the model with visco-plastic rheology change of time-step does not lead to the change of the stress field, in the model with elasto-visco-plastic rheology the stress is changing. To take that into account we perform the following “time zoom-in” strategy. First we fix kinematic boundary conditions at all

boundaries except the surface (remaining to be a stress free boundary) using the velocities from the last time step of the long-term model. Then we decrease time-step to 5 years and run model till the velocity field becomes identical to the velocity field of the long-term model at its last time step. Empirically we have found that 300 to 500 5-years time-steps are enough to get reasonable consistency of the velocity fields of long- and short-term models.

2.1.3 Rheology Modification: Transient Creep

For long-term tectonic deformation it is suitable to use steady-creep rheology with parameters provided by laboratory experiments, like those for the olivine-dominated rocks (Ruina, 1983), see also Table 1. In our long-term geodynamic models we routinely use both (competing) diffusion creep and dislocation creep steady rheologies, but in the active subduction zone setting and at the depth range of less than 300 km, the dominant steady creep process is dislocation creep. Whether dislocation density will change during postseismic period or not depends on the magnitude of the stress increase imposed by the elastic strain during the earthquake. When the stress increase is significant (say doubling of stress) then dislocation multiplication occurs (S. Karato, Personal communication, 2016). Sudden changes of the stress field during the earthquakes lead to the transient rheological behavior (Karato, 2008). We use model for transient dislocation creep rheology based on the ideas of Karato, 1998:

$$\dot{\varepsilon} = \dot{\varepsilon}_{ss}(1 + (\beta - 1)\exp(-\frac{\varepsilon_{ss}(t)}{\varepsilon_{el}^{eq}})) \tag{2.1}$$

$$\dot{\varepsilon}_{ss} = B \cdot \sigma^n \exp(-\frac{H_a}{RT}) \tag{2.2}$$

where $\dot{\varepsilon}$ is power-law creep strain rate, $\dot{\varepsilon}_{ss}$ is steady state power-law creep strain rate, ε_{el}^{eq} is elastic strain induced by earthquake, $\varepsilon_{ss}(t)$ is an accumulated viscous creep strain at time t after the earthquake, β is a constant about 10 for peridotite (Bai et al., 1991), σ is square root of the second invariant of stress deviator, n is power law exponent, H_a is an activation enthalpy of the dislocation creep, R is gaze constant and T is an absolute temperature.

Equation 2.1 has more general form than original equation in Karato, 1998 as it does not assume linear dependency of viscous strain on time. If this dependency is linear, i.e. $\varepsilon_{ss}(t) = \bar{\dot{\varepsilon}} \cdot t$ (where $\bar{\dot{\varepsilon}}$ is an average strain rate) then equation 2.1 reduces to the form from Karato, 1998 also used in Freed et al., 2012, where relaxation time $\tau = \varepsilon_{el}^{eq}/\bar{\dot{\varepsilon}}$. The advantage of our more general formulation is that it contains only one parameter (apart from the steady-state rheological parameters), which is β and all other quantities are calculated.

The transient rheology is applied to the finite elements, where square root of the second invariant of the stress deviator is changing by more than two times at one time step. Due to

this condition, the transient deformation in our models is almost completely restricted to the asthenospheric mantle wedge, where viscosity and long-term stresses are low.

2.1.4 Rheology Modification: Rate-and-State friction Law

We employ classic aging rate-and-state (RS) rheology, discussed previously in the introduction chapter, in the subduction channel. Note that in the original version of the RS law cohesion is absent. In our model we use a very small value of cohesion of 2 MPa in subduction channel to avoid destabilization of the uppermost elements in the model. Our tests show that changing this parameter by two times in any direction does not affect modeling results.

We introduce RS friction rheology in subduction channel. Following common ideas (Scholz, 1998) we implement rate strengthening (b-a) <0 regime in the upper 9 km of the channel. Deeper in the channel we apply rate weakening RS regime (b-a)>0 and in one series of models we do not limit it at depth (Figure 2.6). In another series of models we implement rate strengthening (b-a) <0 regime deeper than 350°C isotherm (Figure 2.7) following the classic ideas about the origin of afterslip (Scholz, 1998; Marone et al., 1991; Perfettini and Avouac, 2004) . We call this latter series of models afterslip models and the model that belongs to this series but has all other parameters as our reference model we call the afterslip reference model.

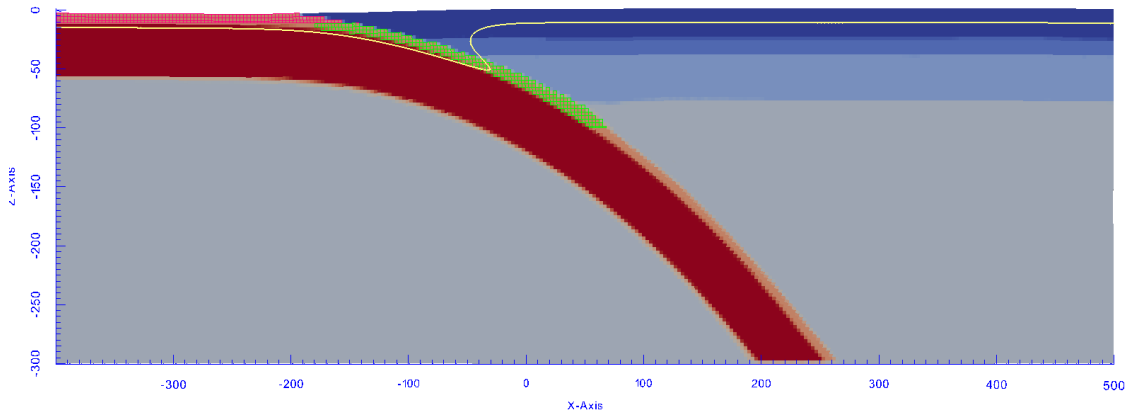

Figure 2.6 Setup of the model with highlighted RS rheology elements. Magenta colored elements till the depth of 10 kilometers denote velocity-strenghtening material (b-a)<0. Green colored elements after depth of 10 kilometers denote velocity-weakening material (b-a)>0. Yellow line represents 350°C isotherm.

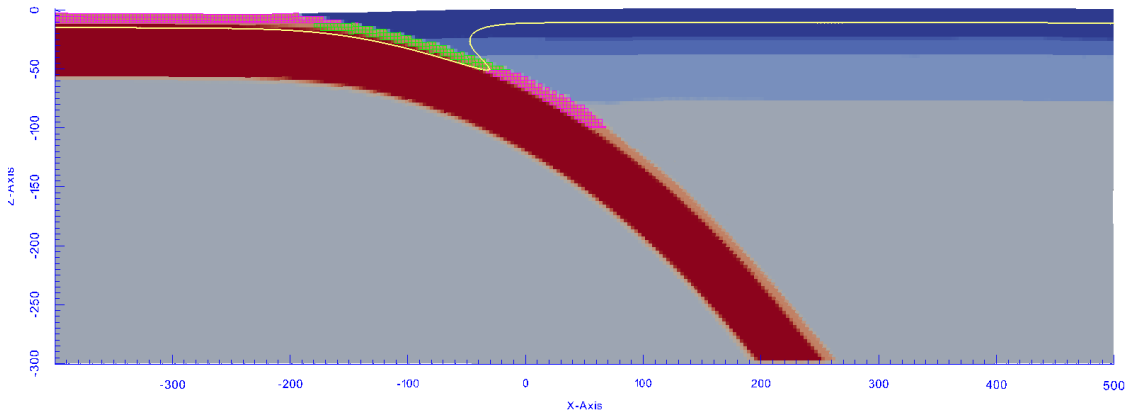

Figure 2.7 Setup of the model with highlighted RS rheology elements. Magenta colored elements till the depth of 10 kilometers and lower 350°C isotherm denote velocity-strenghtening material (b-a)<0. Green colored elements in range of depths from 10 kilometers to 350°C isotherm denote velocity-weakening material. Yellow line represents 350°C isotherm.

According to out tests, we need at least 3 elements to resolve channel, so it is 9 km thick in our typical models. In preparation of our 3D models we have also tested models with 6 km elements and therefore 18 (!) km thick channel with no much changes of the results. The reason why model is not very sensitive to the channel thickness is plastic rheology where shear stress does not necessary depend on the thickness of the shear zone. Viscous flow in the lower part of the channel does depend on the thickness, but this effect is relatively moderate.

To make subduction possible, subduction channel must cross the entire lithosphere and 100 km is the maximal thickness of the lithosphere in our models. Possible penetration of the channel into the asthenosphere does not affect results as deformation in the asthenosphere is, anyway, viscous during most of the seismic cycle and in long-term.

There is no any stress concentration in the deepest parts of the channel due to brittle-ductile transition. Stress becomes very low there, because of the low viscosity. Stress in the channel is concentrated at the down-dip end of the locking zone, which is typically located in our models at depth of 40-50 km and never deeper than 60 km.

2.1.5 Adaptive Time Step Procedure

The maximum time step in our short-term model is 5 years, which is suitable at the late stage of the postseismic and for the interseismic periods, but is much too long for the earthquake itself and following early stage of the postseismic period. See below (2.2.2) the

criterion to define the maximum time step. In order to resolve different stages of the postseismic period we implement the following adaptive time step procedure.

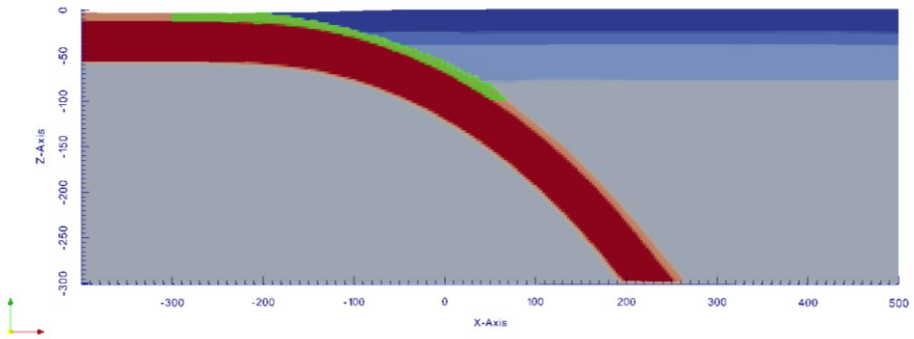

Figure 2.8 Setup of the model with green colored reference zone of strain rate observations.

At each time step we calculate an average shear strain rate in reference zone of subduction channel (Figure 2.8). If its value increases by more than certain critical amount (CA) during step, we decrease the time step and if it decreases by CA the time step is increased. The CA value is defined to detect mostly the largest earthquakes. Empirically found suitable CA values are 25 % to 150 %. If CA is lower, the algorithm starts to detect many smaller earthquakes together with the large ones, which does not change much the final result but drastically increases computation time. If CA is higher than some 150% we start to miss large events. Figure 2.9 illustrates variation of the average slip over the interseismic period for model with CA=100%. As it is seen adaptive time step algorithm ignores small velocity perturbations and recognizes major instability and then starts to decrease time step.

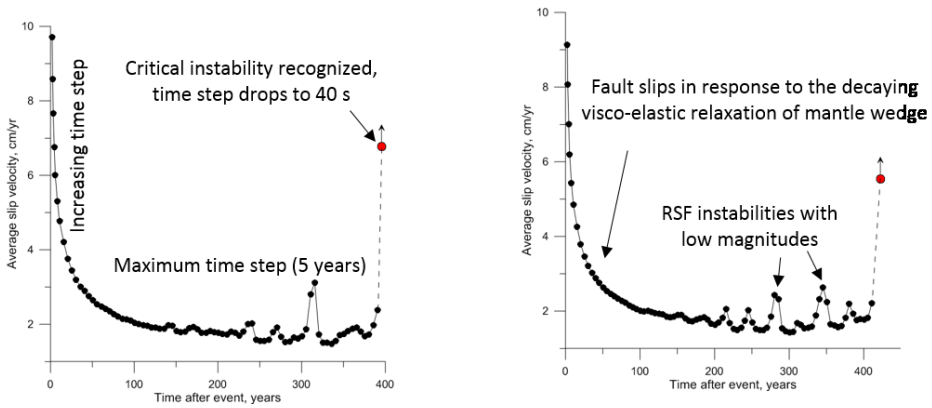

Figure 2.9 Average slip velocity at the entire fault versus time for two randomly chosen events. Red points show velocities at the moment when critical instabilities are recognized. Model is then recalculated with the smaller time step.

The procedure works as following. If at one of the time steps average strain rate in the channel increases by more than (1+CA) times the time step is then decreased by 2 times and calculation is repeated. If required, the stepwise decreasing continues till the time step reaches its smallest value of 40 sec, which happens at the earthquake. The smallest time step (40s) in our 2D model corresponds to the rise time for a great earthquake.

After the earthquake the time step begins to increase incrementally (by 2 times) following decreasing strain rate in subduction channel until it reaches its maximal value of 5 years. . If at one of the time steps average strain rate in the channel decreases by less than 10% the time step is then increased by 2 times. Hence, we keep small time step if change of average strain rate is large. In this way we can follow in details rapidly changing deformation during the entire seismic cycle. Evolution of the time step is shown in Figure 2.10 and Figure 2.11.

Discussed adaptive time step procedures varies time steps for over 6 orders of magnitude. Smooth increasing of time step after earthquake allows to model viscoelastic relaxation in details.

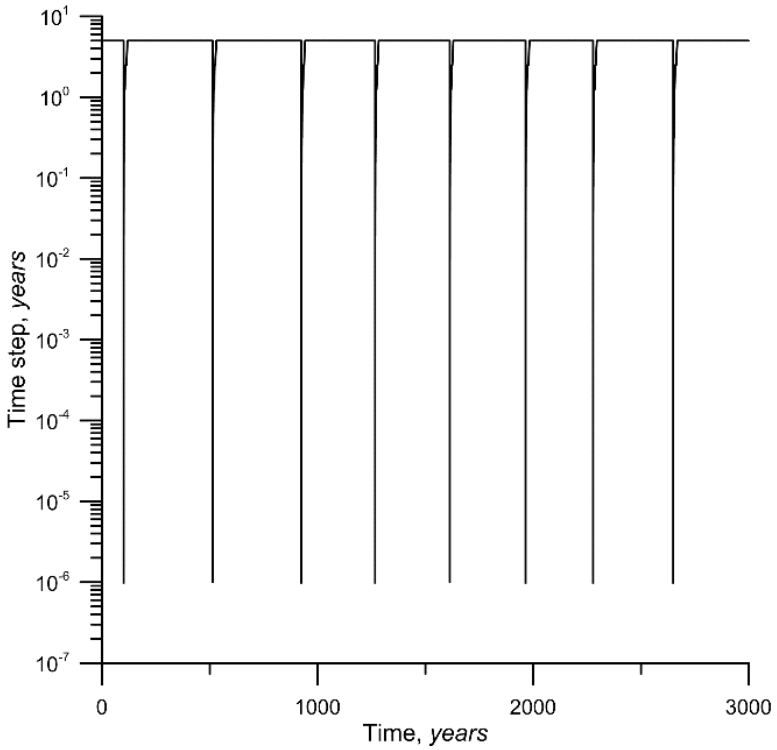

Figure 2.10 Evolution of modelling time step with time for multiple seismic cycles. Time steps vary from 40 seconds (during earthquake) to 5 years (late postseismic or interseismic period).

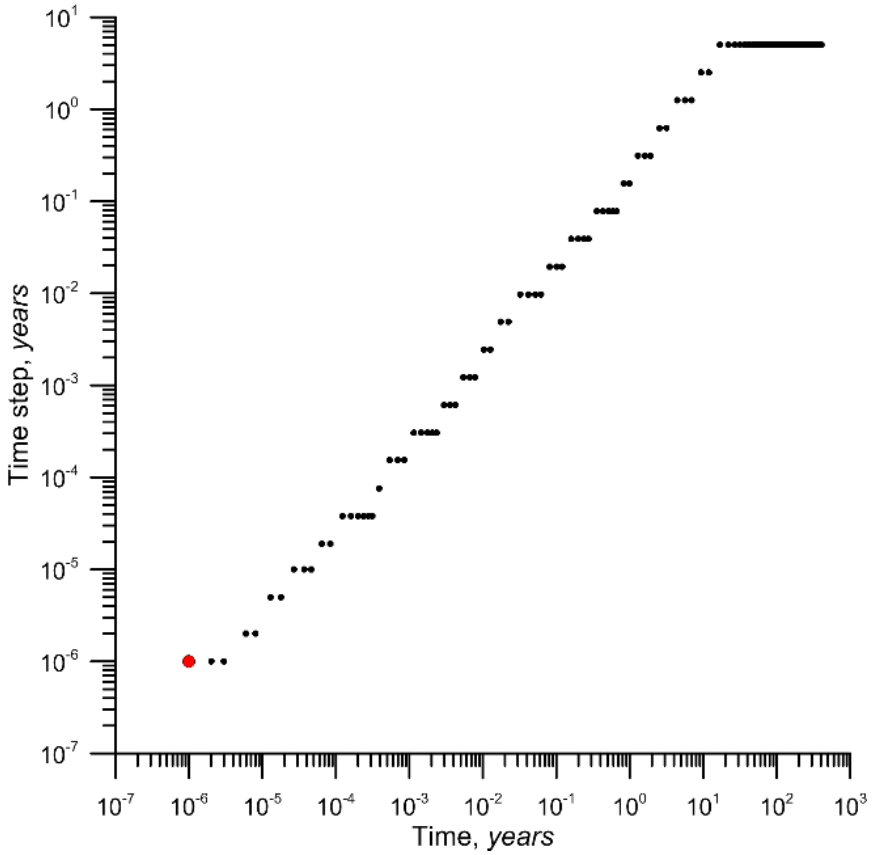

Figure 2.11 Evolution of modeling time step with time for a single seismic cycle (note that time axis is in logarithmic scale) Red circle denotes earthquake moment. Time steps vary from 40 seconds (during earthquake) to 5 years (late postseismic or interseismic period).

2.2 Modeling of Earthquakes: Method

Although focus of our modeling is at postseismic processes at variable time scales and at long-term evolution, it is obvious that reasonably good modeling of the earthquakes is required. In the previous modeling studies (Lapusta et al, 2000; Lapusta and Barbot, 2012) it was demonstrated that in order to resolve properly processes of nucleation and propagation of rupture, the nucleation length h* must be resolved by at least few tens of grid points. With our element size of 3 km and RS parameter L=1-5 cm, h* defined as in Lapusta et al, 2000, is about 2-10 km, so we have only 0.7 to 3 grid points at nucleation length, which is by more than an order of magnitude less than required. From this consideration it is clear that it makes no sense to model rupture propagation with the current model resolution. However, for our purposes, precise modeling of rupture propagation is not required. Instead, what is necessary for modeling of the postseimic transients is (1) to recognize the onset of the largest instability (i.e. great earthquake) and (2) to reasonably reproduce the cumulative slip distribution along the fault.

2.2.1 Earthquake Modeling Procedure

Our modeling procedure is based on the following idea. During an earthquake, the local stress in the channel drops. This is accompanied by dramatic decrease of slip velocity. During the postseismic and interseismic phases stress builds up but slip velocity remains low until instability (i.e. earthquake) occurs. While approaching the instability the average slip velocity at the fault rises and begins to fluctuate if maximum time step is enough small. The instability shows up as a large fluctuation of the slip velocity. By constant monitoring strain rate changes at the fault, we are able to recognize this moment and to drop our time step, till the smallest time step (here- 40s) is achieved. Our rupture typically takes one or two of the smallest time steps; after that we gradually increase the time step to simulate postseismic processes. Note that this algorithm is aimed to model the largest events, so we may miss the small ones.

2.2.2 Criterion for Maximum Time Step

The maximum time step is defined to be enough small, that RSF instability can develop. Assume for simplicity steady state RSF regime. In this case, change of slip velocity from slow velocity V_{sl} to fast V_{ft} at time step Δt will cause stress drop $\Delta\sigma$

$$\Delta\sigma = \sigma_n \cdot (b-a)^* \cdot \ln\left(\frac{V_{ft}}{V_{sl}}\right) \tag{2.3}$$

Which in turn can be related to the slip at the fault

$$\Delta\sigma = C \cdot G \frac{V_{ft}\cdot\Delta t}{W} \tag{2.4}$$

Where C is constant of the order of unity, G is shear modulus and W is characteristic rupture distance (width). Combining (2.3) and (2.4) obtain following simple equation for $Y = V_{ft}/V_{sl}$

$$\gamma Y = \ln Y \text{ , where } \gamma = C \cdot G \frac{V_{sl}\cdot\Delta t}{W\cdot\sigma_n\cdot(b-a)^*} \tag{2.5}$$

Equation (2.5) has solution only if value of γ fulfills the following condition:

$$\gamma = C \cdot G \frac{V_{sl}\cdot\Delta t}{W\cdot\sigma_n\cdot(b-a)^*} \leq \frac{1}{e} = \frac{1}{2.72} \tag{2.6}$$

That defines a maximum value of the time step at which RSF instability can develop

$$\Delta t < \frac{W \cdot \sigma_n \cdot (b-a)^*}{2.72C \cdot G \cdot V_{sl}} \tag{2.7}$$

2.2.3 Definition of Minimum Time Step

As we do not model rupture propagation, we must assume some value for the minimum time step, Δt_{min}. For 2D model a reasonable guess for Δt_{min} would be earthquake rise time scaled with the rupture width. For the great megathrust earthquakes that should be about several tens of seconds and much smaller for the strike-slip earthquakes. It is important that the modeling results do not depend much from the choice of Δt_{min}, as it follows from the analysis below.

If in (2.6) $\gamma \ll 1/e$, then (2.6) has two clearly separated solutions

$$Y_1 \cong 1 \text{ (slowly creeping fault) and } Y_2 \cong \frac{1}{\gamma}\ln(\frac{1}{\gamma} ln \frac{1}{\gamma}) \tag{2.8}$$

The second solution in (2.8) represents fast slip during an earthquake. According to (2.8), in first approximation the fast slip velocity is inverse proportional to the value of Δt_{min}. It means that stress drop during the earthquake (2.3) depends on Δt_{min} only as logarithm and it changes only by about 5% if Δt_{min} changes by e times.

2.2.4 Calculation of Earthquake's Parameters

In order to calculate parameters of earthquake we introduced special procedure. First, at the moment of earthquake it spots all elements with strain rate more than 10^{-5}1/s. So rupture zone is determined with zone were slip during 40 seconds step in channel was more than several cm. Hence, we can calculate rupture width. Having control area we measure slip of closest nodes with respect to channel on the left and right side of the channel at every depth. Thus, we obtain distribution of slip at every depth along the channel, average slip in rupture and average slip velocity of the rupture.

Knowing rupture width and average slip we can calculate 2D seismic moment and later using scaling relations for subduction zones earthquakes from Strasser et al. (2010) we can calculate moment magnitude.

Then at every depth of the defined rupture we look for elements with the largest strain rates. We measure stress drop on these elements to calculate the average stress drop of the earthquake. During giant earthquakes rupture can propagate to the viscous regions were values of stress drop are negative. Also, in setups where we employ velocity-strengthening rheology below 350°C isotherm, stress drop is negative in area of velocity-strengthening material.

For convenience we track all mentioned parameters during postseismic and interseismic periods till the next earthquake. With registration of the new earthquake we

recognize observation area again and repeat all mentioned before procedures. Figure 2.12 illustrates example of procedure measurements.

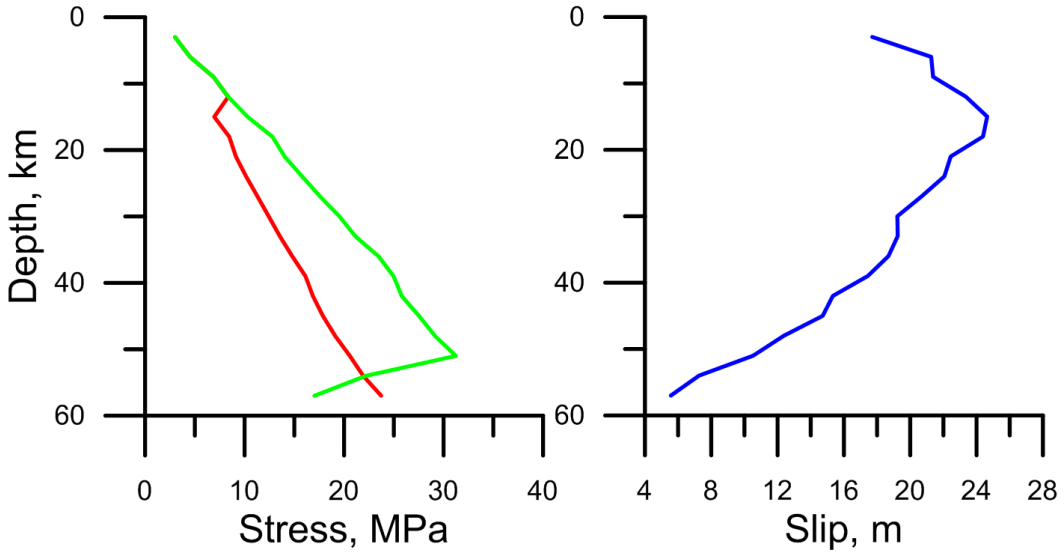

Figure 2.12 Example of measuring of earthquake in reference model with Mw 9.32. (a) Distribution of stress with depth before earthquake (green line) and after (red line). Average stress drop is 4.72 MPa.(b) Slip distribution along the fault with depth during earthquake. Average slip is 17.8 m.

2.2.5 Calibration of the Model

We calibrate RS parameters, mostly (b-a), and L in order to replicate an average slip (about 20 m (Moreno et al., 2009)), stress drop of 5 MPa (Seno, 2014) and recurrence time (about 400 years (Cisternas, 2005)) of the Great Chile Earthquake of year 1960. Figure 2.13 presents results of some calibration experiments showing dependencies of average static stress drop, seismic moment and earthquakes recurrence period on (b-a)* parameter.

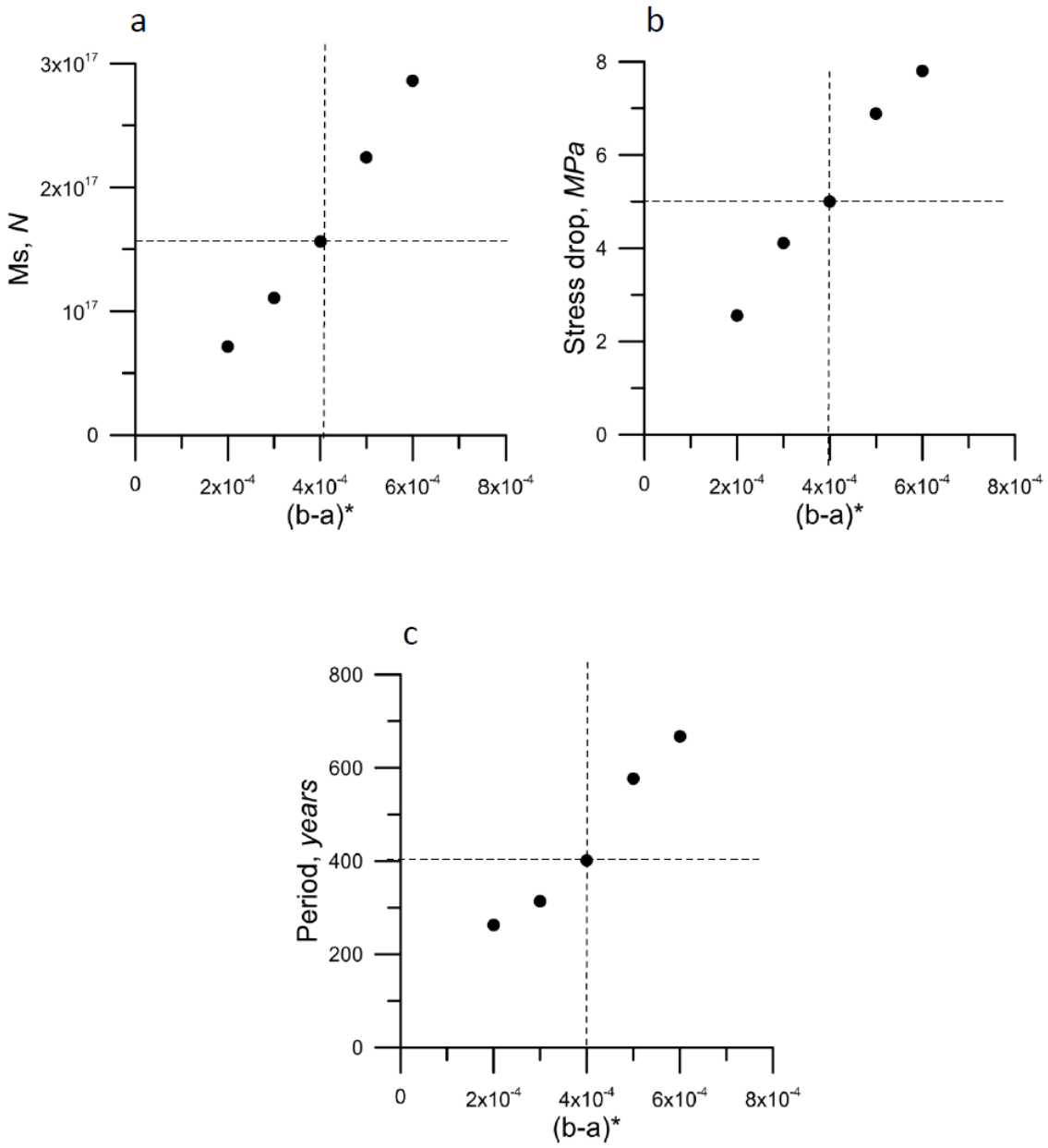

Figure 2.13 Mean (a) 2D seismic moment, (b) Stress drop, and (c) recurrence time (period) of the earthquakes generated by the reference non-linear transient model with different RS (b-a) parameter. Horizontal dashed lines correspond to the estimated values of stress drop of 5 Mpa (Seno, 2014) and recurrence time of 400 years (Cisternas, 2005) for Great Chile 1960 Earthquake. Vertical lines correspond to appropriate values of RS (b-a)* parameter.*

At the values of the RS parameters $(b-a)^*=4*10^{-4}$ and L<18 cm at b/(b-a)=3 and L<10 cm at b/(b-a)=5 a spontaneous instabilities are generated leading to the stick-slip deformation process with the average recurrence times of earthquakes of 350-430 years and average 2D seismic moments of $1.5\text{-}1.8*10^{17}$N, and average static stress drops of 4-6 MPa. Both recurrence times and moment magnitudes (Mw=9.3-9.35 assuming rupture length of 800 km) are close to the geodesy-based estimates for the Chile 1960 event (Moreno et al., 2009; Cisternas, 2005). The magnitude of stress drop is also close to the estimation for Chile 1960 event of 5 MPa (Seno, 2014).

2.2.6 Seismic Cycles

After implementation all procedures discussed in Chapter 2.2 we model earthquakes and multiple seismic cycles (Figure 2.14).

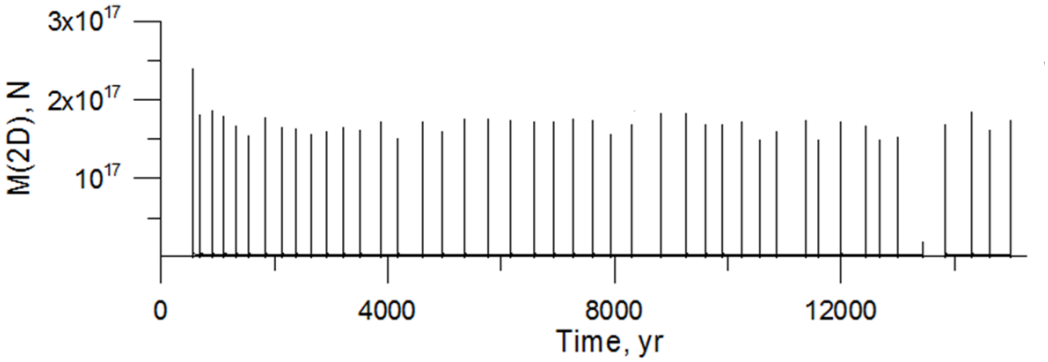

Figure 2.14 Sequence of the earthquakes (2D seismic moment) generated by the reference non-linear transient model.

On the Figure 2.15a we show spatial distribution of strain rate and velocities during interseismic coupling. One can clearly see the locked zone which ends at the depth around 60 kilometers where brittle-ductile transition takes place. In the part of the fault deeper than brittle-ductile transition relative velocities on interface of the fault are similar to the velocity of subduction, around 7 cm/y.

During modeled earthquakes (Figure 2.15b) rupture propagates much deeper than locking zone while largest displacements occur at the bottom of the locking zone.

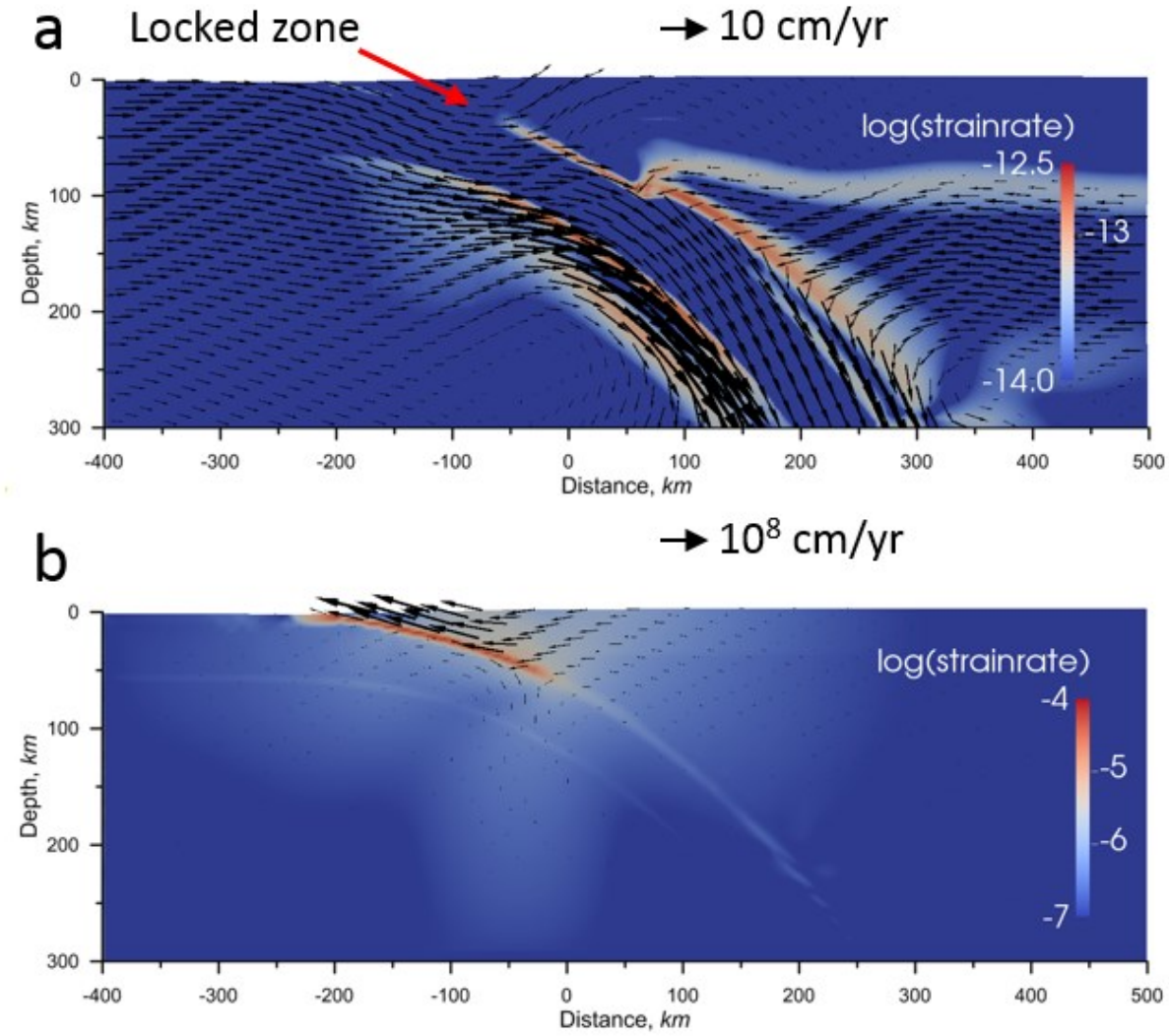

Figure 2.15 Snapshots of the spatial distributions of strain rate (background colors) and velocities (vectors) for the interseismic coupling (a) and for the moment of earthquake (b) generated by the reference non-linear transient model.

2.3 Verification of the Method

2.3.1 Test of Modeling Procedure by Comparison with Known High Resolution Solution

We test our modeling procedure by simulating seismic cycle at a strike-slip fault in a setup similar to study by Lapusta et al. (2000) (Figure 2.16). Original setup (Figure 2.16 left) includes two elastic plates separated by weak zone (fault) with implemented rate-and-state rheology. We employ static velocity boundary conditions on the left and right borders of the model to initiate loading. Since setup is anti-symmetrical we don't need to model whole geometry, and use simplified version which contains "half" of the model (Figure 2.16 right).

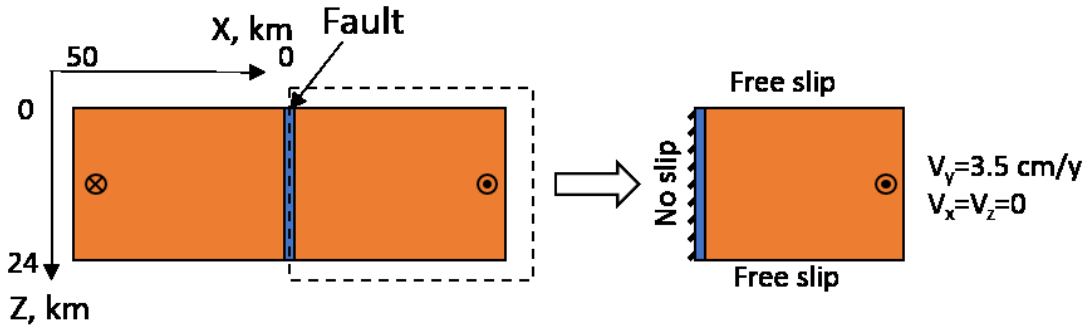

Figure 2.16 Model setup (left) approximating model of strike-slip seismic cycle by Lapusta et al., 2000. Model is antisymmetric in respect to YZ plain at X=0, which allows considering only half of the model (right) in the computations.

We aim to reproduce solution for the case of small h*=0.235 km, when the authors obtain large events with a recurrence time of 70-80 years accompanied by much smaller events occurring some 20 years after the large events. We assume depth distribution of RSF parameters a, b and L and distribution of normal stress (Figure 2.17) as in study Lapusta et al. (2000). Model finite element size is 0.2 km, which makes only about 1 grid at h* length and 75 grids at seismogenic zone of 15 km, similar to our models for the megathrust earthquakes. The maximum time step is defined as 1 year which fulfils (2.7). We test two options for the smallest time step, of 7.5 and 15 s. In order to recognize appearance of instability we monitor strain rates at the entire 24 km of fault. We run models with two values of CA parameter, 100 and 200%. Note that because of different dimensions of the monitoring regions in strike-slip and megathrust models, the corresponding values of CA defer by about two times, so CA=100-200% for strike-slip model correspond to about CA=50-100% for megathrust models.

Evolution of average slip velocity at the fault before, during and after strike-slip event is demonstrated in Figure 2.18. Time step remains constant (1 year) till the moment when calculated slip velocity increases at one time step by certain amount according to CA criterion. At this moment potential instability is identified and model is recalculated with 2 times smaller time step and velocity is again checked according to the instability criterion. The procedure is repeated until either instability criterion is not fulfilled or minimum time step is achieved. In practice this procedure in most cases leads to the drop of time step right to its minimum value (15 s in this case).

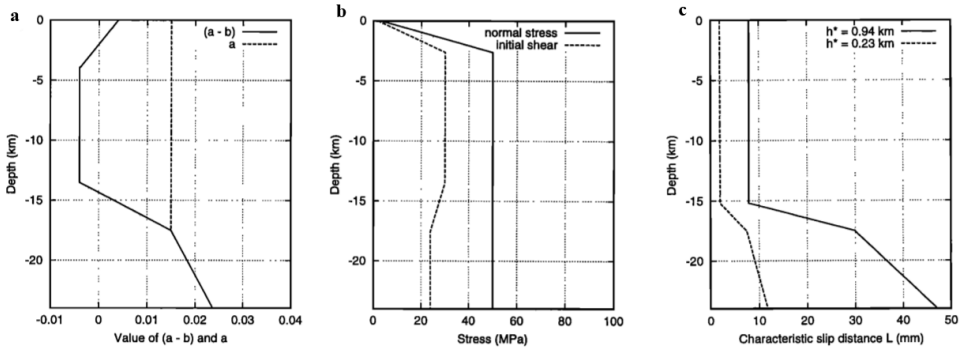

Figure 2.17 (a) Depth-variable distribution of frictional parameters (a-b) and a, consistent with the measured temperature and inferred depth variation of (a-b) of Blanpied et al., (1991, 1995) for granite under hydrothermal conditions; (b) Depth-variable distribution of the effective normal stress and initial shear stress. (c) Depth-variable distribution of the characteristic slip distance L of the friction law, for the two cases considered. From Lapusta et al., 2000.

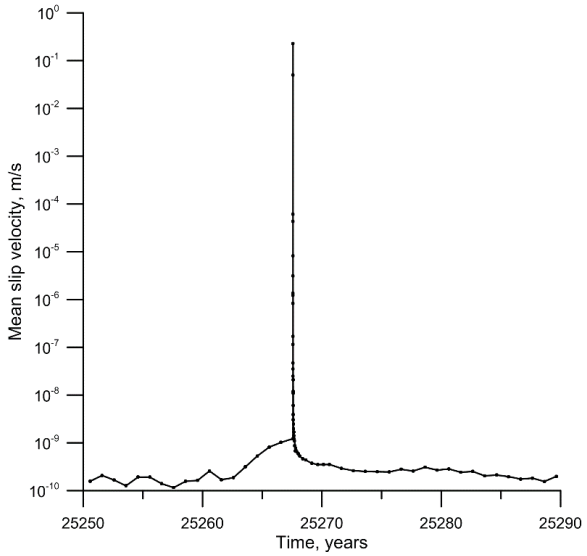

Figure 2.18 Average slip velocity versus time for an individual event.

The modeling procedure generates regular periodic sequences of large events (Figure 2.19). As expected, our algorithm is missing small events modeled in Lapusta et al. (2000) but successfully models the large events. Periods of large events are similar in all model classes with a little larger periods for the model classes with minimum time step of 7.5 s. The periods vary from 85 to 95 years, which is about 10 % longer than periods of large events in corresponding Lapusta et al. (2000).

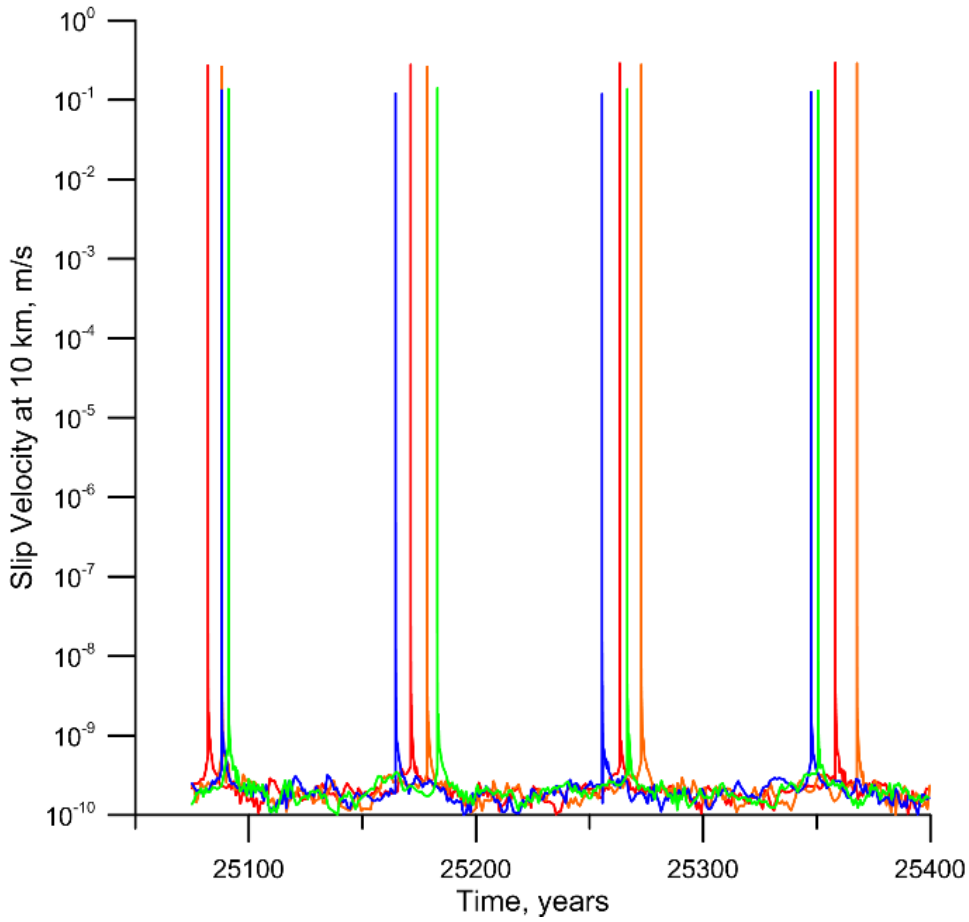

Figure 2.19 Slip velocity at 10 km depth for all events and model classes (colored curves). Red corresponds dtmin=7.5 s, CA=100%, Orange – dtmin=7.5 s, CA=200%, Blue – dtmin=15 s, CA=100%, Green – dtmin=15 s, CA=200%.

Coseismic slip distributions (Figure 2.20) are also similar for all events and all model classes (within +-5% from average) and they are by about 10 % larger than slip of the large events in Lapusta et al. (2000). Note that our solutions are almost identical to the quasi dynamic solution for the singe event model from study Lapusta et al. (2000).

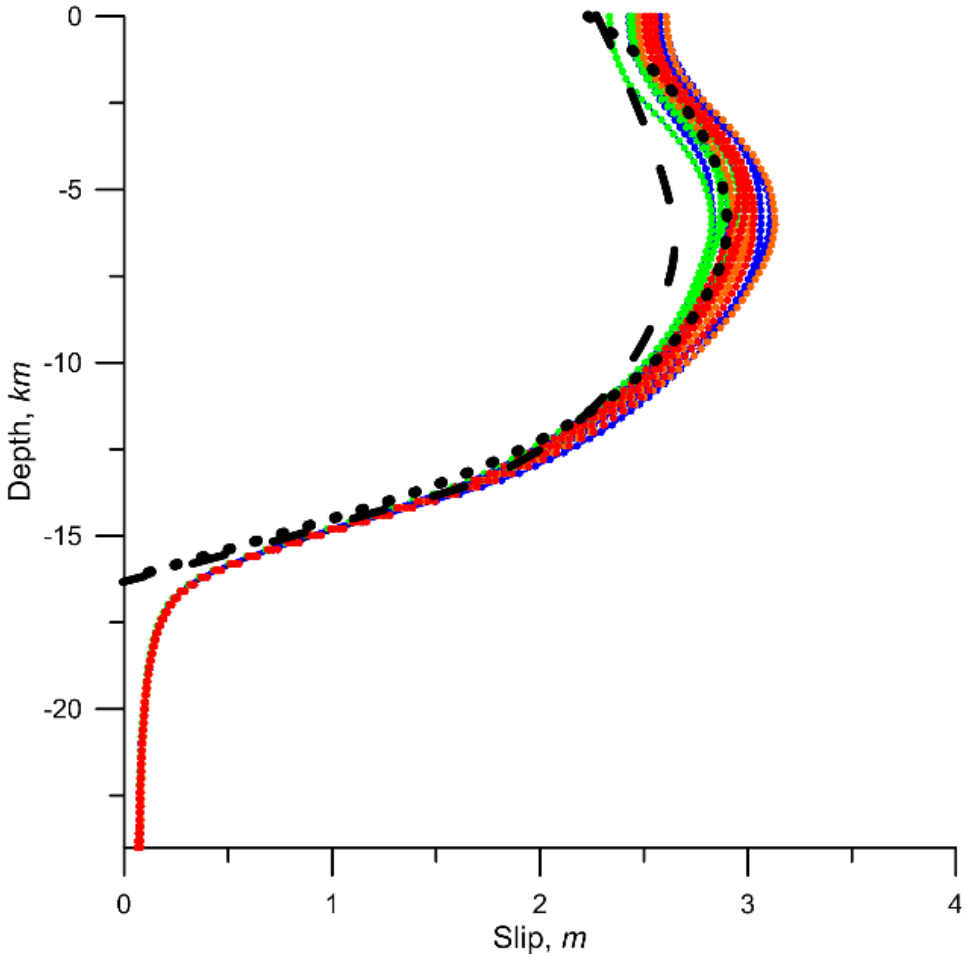

Figure 2.20 . Coseismic slip distribution for all events and model classes (colored curves) together with the slip distribution for the large event from double events (black long-dashed curve) and single event from quasi-dynamic solution (black short-dashed curve) from Lapusta et al., 2000. Red corresponds dtmin=7.5 s, CA=100%, Orange – dtmin=7.5 s, CA=200%, Blue – dtmin=15 s, CA=100%, Green – dtmin=15 s, CA=200%.

Compared to Lapusta et al. (2000), we obtain more numerical nois in interseismic period due to the insufficient spatial resolution. Having resolution of grid $\eta \approx 1$, perturbations of every single cell cannot be damped. But relatively high CA values alow adaptive time step procedure to ignore this perturbations. Also as it was shown on Figure 2.19 and Figure 2.20

relatively poor temporal resolution still allows reproducing model of Lapusta et al. (2000) reasonably well.

Thus, insufficient spatial resolution (about 40 times less than required) and temporal resolution to model details of rupture nucleation and propagation, still allows us to model such parameters of earthquakes as recurrence time and cumulative coseismic slip in reliable way. Adjusted CA parameter of adaptive time step procedure (2.1.5) ignores small events and allows to model major events in the model.

2.3.2 Robustness of the Models

Numerical tests show that change of minimum time step by two times in both directions changes average period and average moment of events by less than 4 % (larger period and moment for the shorter time step) in agreements with theoretical analysis presented in 2.2.2. Two times increasing of grid size (to 6 km, low resolution), with all other parameters fixed, decreases average 2D moment of the earthquakes from 1.57* 10^{17} N (reference resolution) to 1.27*10^{17} N (20% difference). Two times decreasing of grid size (to 1.5 km, high resolution) increases average 2D moment of the earthquakes from 1.57* 10^{17} N to 1.65*10^{17} N that makes about 5% difference, which is close to 2 standard deviations of moments distribution in the sequences of events in the reference model (Figure 2.21). Solutions with FE sizes of 1.5 and 3 km significantly overlap, while solutions with 1.5 and 3 km do not.

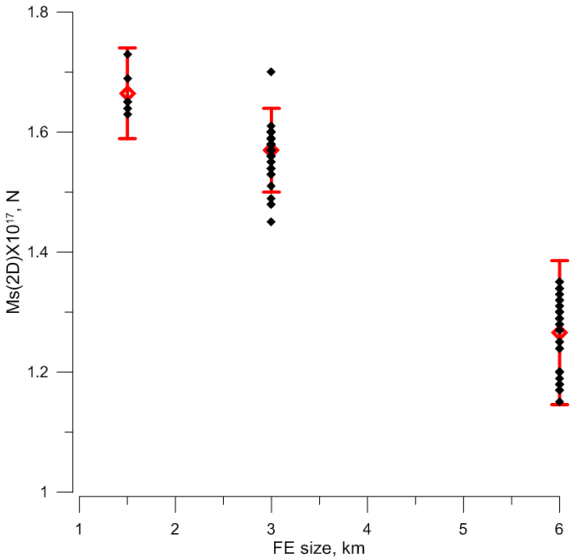

Figure 2.21 Model convergence with decreasing finite element (FE) size. Shown are moments for the sequences of events in the models with 3 sizes of elements (black symbols), their average values (red diamonds) and two standard deviations (red bars).

2.3.3 Effect of Instability Criterion (CA)

Modeled recurrence time of earthquakes, seismic moment, stress drop and distribution of slip at the fault do not depend on the value of CA criterion unless CA becomes less than some 20% or higher than some 150% (Figure 2.22). This demonstrates robustness of our procedure for identifying the appearance of instability and estimation of cumulative slip distribution.

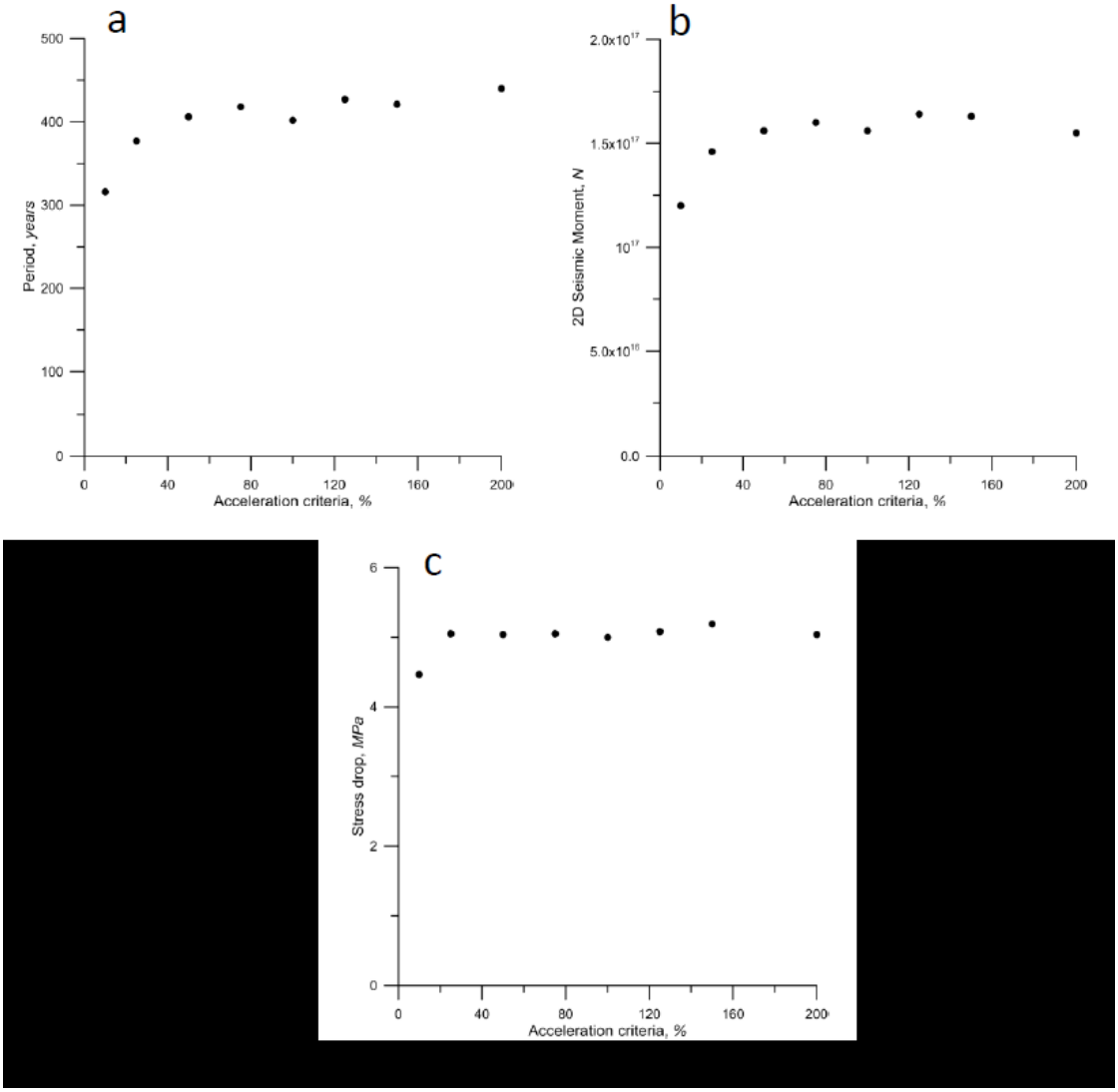

Figure 2.22 Effect of acceleration criteria (CA) for adaptive time step procedure on (a) period, (b) 2D seismic moment, and (c) stress drop.

2.3.4 Effect of Rate-Weakening Law

We also test the influence of the rate-weakening law on the earthquake parameters. We have adopted rate-weakening law from Van Dinther et al. (2013) with constant 1 year modeling time-step and calibrate its parameters to get stress drop of 5 MPa at individual events.

$$\mu\left(1-\frac{P_f}{\sigma_n}\right)=\mu^*=\mu_{st}^*-\Delta\mu_0\frac{V}{V^*}\frac{1}{1+\frac{V}{V^*}} \tag{2.9}$$

where, V is a slip velocity at the fault and $\Delta\mu_0$ and $V^*$are model parameters.

We obtained regular events with recurrence time of about 400 years and average 2D seismic moment about $1.5*10^{17}$ (Figure 2.23) for the model parameters $\Delta\mu_0 = 0.02$ and $V^* = 2.5\ m/yr$. Slip distribution for the typical event is shown in Figure 2.24 by red dashed curve. Slip distribution is similar to the RS models, but as could be expected from the larger time scale of rupture (few years versus 40 s in RS models), the rupture in this model does not penetrate as deep as in the RS models. This test demonstrates that, given magnitude of stress drop, neither cumulative slip distribution, nor recurrence time of largest events notably depend on the type of the rate-weakening law. What really matters is magnitude and depth distribution of stress drop, which, in turn, depends on depth dependence of normal stress and (b-a)* parameter (or its analog in case of rate-weakening model suggested in van Dinther et al., 2013).

These arguments support robustness of our modeling of largest earthquakes, but certainly we cannot exclude that we are missing smaller events.

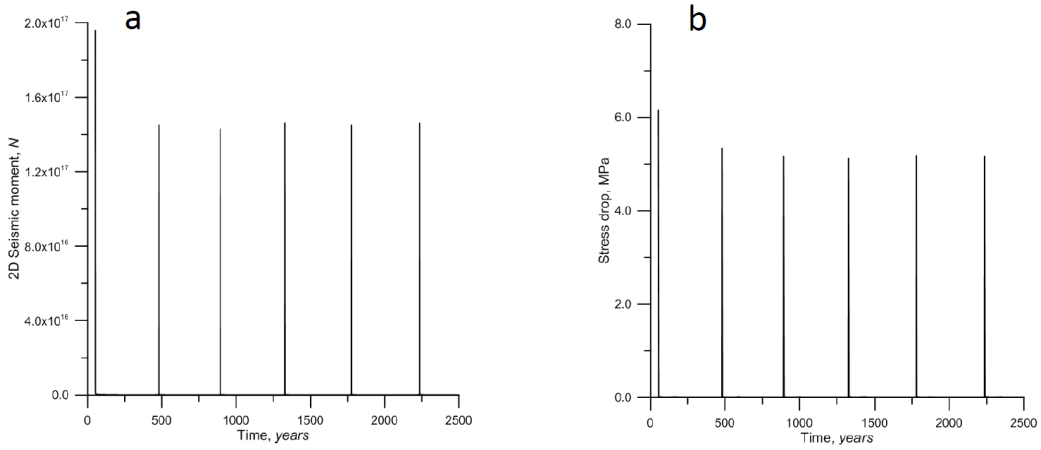

Figure 2.23 Evolution in time of (a) 2D seismic moment and (b) stress drop for the earthquakes generated by model with rate weakening friction law (van Dinther et al., 2013).

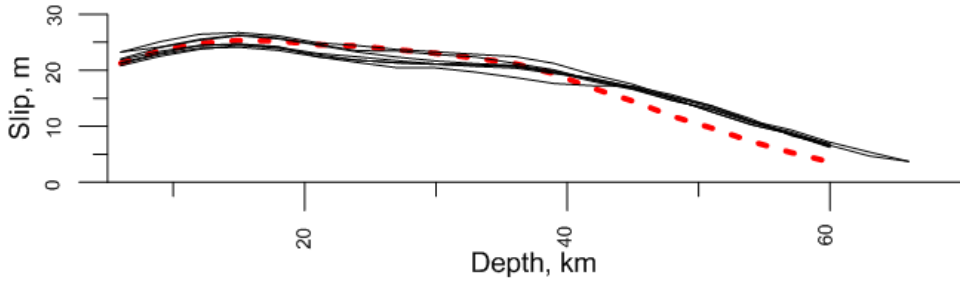

Figure 2.24 Distribution of slip with depth during earthquakes generated by reference models with different acceleration criteria (black curves) and by model with rate weakening friction law (van Dinther et al., 2013) (red dashed curve).

2.3.5 Verification of the Friction Parameter

The suitable effective (b-a)* parameter to generate the largest earthquakes in our model is $4*10^{-4}$. In order to compare this value with the laboratory derived values we need first to make corrections for the high fluid pressure effect. The fluid pressure factor can be estimated using equation 1.35, the values for effective static friction in the channel of 0.015-0.02 and friction coefficient for dry rocks in subduction channel of about 0.5. This gives us fluid pressure factor of 0.03-0.04. By dividing $4*10^{-4}$ by this factor we get our estimate of the "real", not affected by fluid pressure values of (b-a) of 0.01-0.013. These values are at the upper range of the experimental values and are about 2-3 times larger than expected average values (Scholz, 1998; Bai et al., 1991). Note, however that during the large earthquakes an additional friction weakening processes like fluid pressurization are expected and modeled (den Hartog et al., 2012). We may expect that fluid pressurization is particularly extensive at subduction faults with initially high fluid pressure like in South Chile. Therefore we find reasonable prediction of our model that for the largest earthquakes, which we consider here, about a half or more of the friction weakening is related to the processes like fluid pressurization within the fault.

As half or more of the friction weakening may be in fact related to other than RSF type of friction weakening mechanisms we have also run models with (b-a) parameters of 1/3 of (b-a)* parameter in the reference model and additional linear slip-weakening friction law.

In these models we replace equation 1.28 by the following equation

$$\mu^* = \mu_{st}^* - (b-a)^* \cdot \ln\left(\frac{V}{V_{st}}\right) + b^* \cdot \ln\left(\frac{\Theta V}{L}\right) - \Delta\mu^*(D) \quad (2.10)$$

$$\Delta\mu^*(D) = \Delta\mu_0^* \cdot \min\left(\frac{D}{D_0}, 1\right) \quad (2.11)$$

Where, D is slip at any point of the fault during one time step, $\Delta\mu_0^*$ is the maximum non RSF friction drop and D_0 is a characteristic displacement. If value of D_0 is large enough (about meter or so), the additional friction drop takes place only during a large earthquake. We have run two models similar to our reference model but with reduced (b-a)*=1.310^{-4}, and additional slip-weakening friction with parameters $\Delta\mu_0^*$=0.005, D_0 =1 m (model 1), and $\Delta\mu_0^*$=0.007, D_0 =1 m (model 2) (see Figure 2.25). These models generate seismic cycles with events with average 2D moments of 1.25 10^{17}N (model 1, equivalent to Mw=9.27 at rupture length of 800 km) and of 1.8 10^{17}N (model 1, equivalent to Mw=9.37 at rupture length of 800 km). The recurrence times are about 250 years for model 1 and 400-450 years for model 2 (Figure 2.25). Stress drop varies between 2.5 and 3.5 MPa for the events of model 1 and between 6 and 7 MPa for the events of model 2.

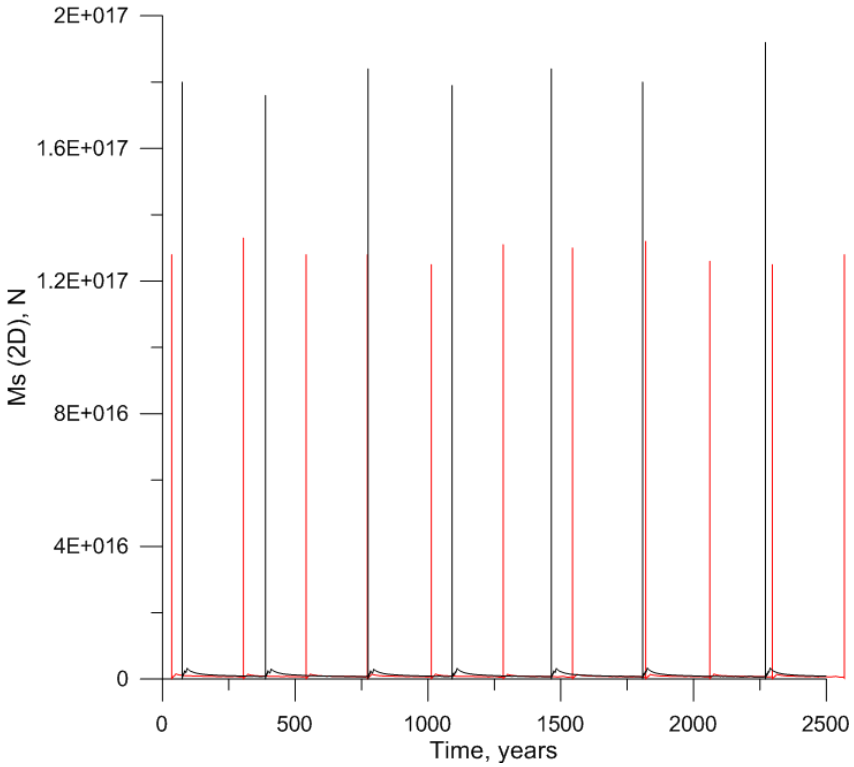

Figure 2.25 Evolution in time of 2D seismic moments in the models with RSF with reduced (b-a)=1.3 10^{-4} and additional slip weakening friction with $\Delta\mu_0^*$=0.005 (red) and $\Delta\mu_0^*$=0.007 (black).*

2.4 Conclusion

We developed technique for cross-scale modeling of great earthquakes and its multiple cycles. Technique includes preparing long-term model of subduction by running the two-plates model for about 10 Mln years in geological time-scale. Then we turn our model to seismic cycle time scale with maximum time step of 5 years.

We modified long-term rheological model by including transient power-law viscosity. We introduced rate-and-state friction law in the subduction channel which results in regular instabilities.

In order to resolve earthquake and different stages of the postseismic period we implemented the adaptive time step procedure, which gradually changes time steps in the range of 40 seconds to 5 years.

Due to long calculation time of our models we use temporal and spatial resolution much lower than it is considered in Lapusta et al., 2000. Thus, we developed our own criteria for maximum and minimal time steps in our model, which allows to run models in adequate period of time having reliable solution.

We conducted a series of experiments to calibrate our rate-and-state friction parameters for our reference model of southern Chile and Great Chile earthquake of 1960 resulting in realistic period, average displacement and stress drop.

Proper modelling of earthquakes requires to use dynamical method with minimal time steps of milliseconds, and much higher spatial resolution than we use. In order to prove that our approach is valid for modeling of earthquakes, we conducted a series of experiments to verify our method by comparison with the strike-slip model of Lapusta et al., 2000. Replicating whole setup of Lapusta et al., 2000 and using our modeling procedure we obtained similar period of earthquakes, and coseismic slip distribution.

Spatial resolution test demonstrates convergence of our modeling procedure, and test with adjustable model parameters demonstrates robustness of our modeling results.

Chapter 3 Postseismic Relaxation Modeling

In terms of postseismic relaxation we consider different models. The most interesting setup is non-linear transient cross-scale model which is our reference model. The model has the following parameters: Transient rheology parameters β =10, RS parameters: L=1 cm, b/(b-a)=3, (b-a)*=- $6 \cdot 10^{-5}$ at the depth range of 0-9 km, and (b-a)*=$4 \cdot 10^{-4}$ at depth >9 km without depth limit.

The reference afterslip model has the same parameters as the reference model but (b-a)*=- $2 \cdot 10^{-4}$ at depth > 42 km. All these models generate earthquakes with Mw about 9.3 and are called "Mw 9.3" models.

By changing (b-a) parameter to $1 \cdot 10^{-4}$ with all other parameters as in reference models we obtain earthquake with about 4 times lower seismic moment. The corresponding models are called "Mw 8.9" models.

Linear models. The linear transient model has constant viscosity of $3 \cdot 10^{18}$ Pa s in the asthenosphere, transient rheology parameter β =10 and RS parameters as in the reference model. The linear transient afterslip model (a proxy for conventional model) has constant viscosity of $3 \cdot 10^{18}$ Pa s in the asthenosphere (depth>80), transient rheology parameter β =10 and RS parameters as in the reference afterslip model.

Linear steady models have the same parameters as linear transient models, but β =1, which leads to no transient viscosity changes (see equation 2.1).

3.1 Non-Linear Transient Cross-Scale (Reference) Model

For certain values of the RS parameters (chapter calibration of the model) spontaneous instabilities are generated leading to the stick-slip deformation process with the average recurrence time of earthquakes of 350-430 years and average 2D seismic moment of 1.5-1.8*10^{17}N (Figure 3.1a). Both recurrence time and moment magnitude (Mw=9.3-9.35 assuming rupture width of 800 km) are close to the estimates for the Chile 1960 event (Moreno et al., 2009; Cisternas, 2005). In agreement with theoretical expectations (Ruina 1983; Scholz, 1998) and previous numerical models, i.e. Lapusta and Barbot (2012); Liu and Rice (2007), we observe a seismic deformation regime if the critical slip distance parameter L is sufficiently small with other parameters fixed. In particular, seismic events are generated at L<10 to 18 cm depending on other RS parameters, i.e. b/(b-a) ratio (Figure 3.1b). Interestingly, despite we cannot resolve sufficiently nucleation of the rupture we do observe change of regimes at the critical non-dimensional ratio W/h* (where W is rupture width and h* is rupture nucleation length) of the order of 10, close to the previous numerical results (Liu and Rice, 2007) with almost linear dependence of the critical ratio on the b/(b-a) parameter previously reported by

Rubin (2008). At values of L larger than 10-18 cm, our models produce slow slip events or decaying oscillations (inset in Figure 3.1b) instead of seismic events.

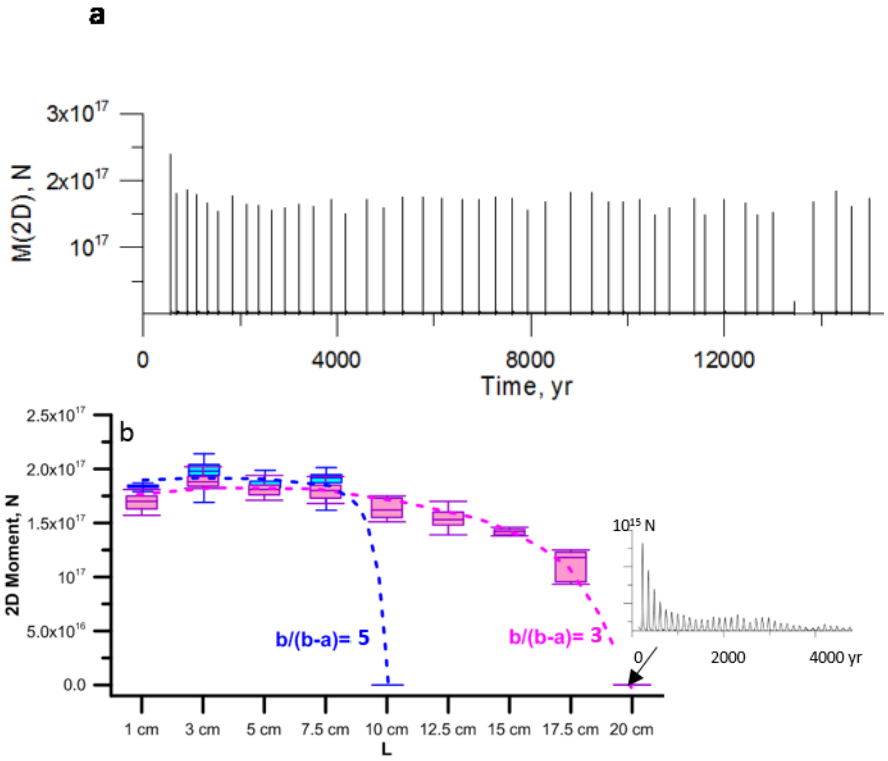

Figure 3.1 (a) Sequence of the earthquakes generated by the reference non-linear transient model with the RS L parameter of 1 cm. (b) Distribution of seismic moments of the earthquakes sequences generated by the non-linear transient models with different RS L parameters for the b/(b-a)=3 (pink boxes and curve) and b/(b-a)=5 (blue boxes and curve). Each colored box includes 50% of the calculated moments and colored bars show the entire ranges of calculated moments for the particular L and b/(b-a) values. Dashed curves approximate the results. Inset at the right side shows non-seismic solution corresponding to larger than critical values of L parameter.

Distribution of velocities and horizontal displacements during a typical modeled earthquake are shown in Figure 3.2 and Figure 3.3. Note that modeled displacements are close to the most recent estimations for the Chile 1960 event based on geodetic observations (Moreno et al., 2009). Interestingly, although in this model we do not set the depth limit for the rate-weakening RS regime explicitly, the largest ruptures do not penetrate deeper than the depths where temperature is higher than 450-500°C (Figure 3.2 and Figure 3.3), in agreement with the previous modeling results (van Dinther et al., 2013). As we demonstrate in Seismic

Cycle Modeling section, the RS parameters that allow us to model the sequence of earthquakes similar to the greatest recorded earthquake, at an extremely weak subduction fault with effective friction of 0.015, are reasonably consistent with the experimental data on RS rheology.

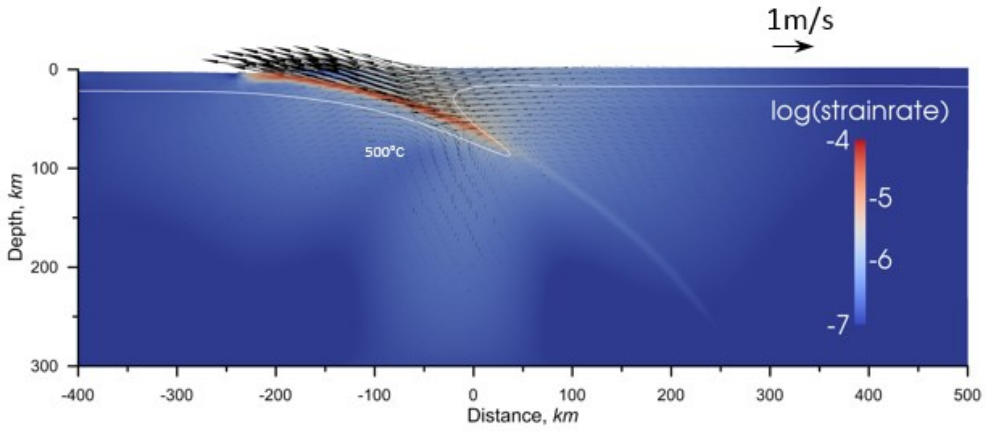

Figure 3.2 A snapshot of strain rate spatial distribution (with velocity vectors) for the typical event.

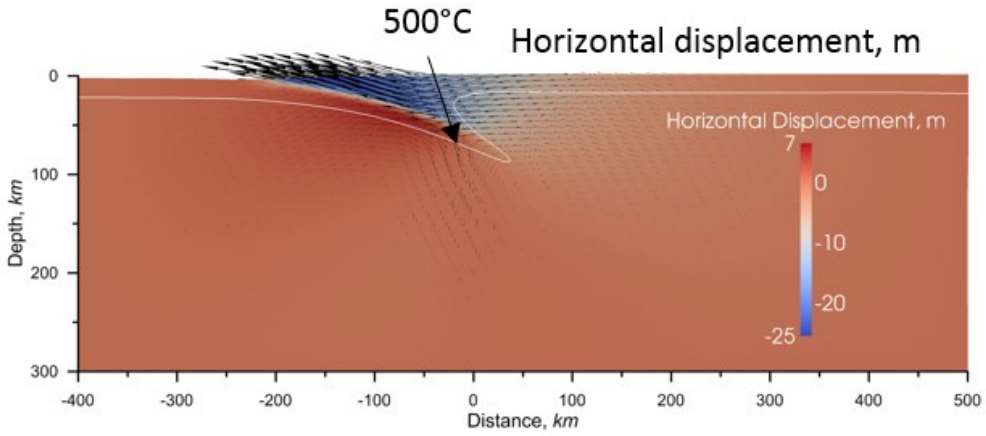

Figure 3.3 A snapshot of the horizontal coseismic slip distribution during the same event.

The model shows remarkably realistic postseismic deformation patterns (Figure 3.4). For instance, the model reproduces landward motion of the near-trench region of the upper

plate that begins early after the earthquake (Figure 3.4 b-e). Thanks to the unique ocean bottom geodetic instruments network, this phenomenon was for the first time observed and modeled for the Great Tohoku 2011 Earthquake (Watanabe, 2014; Sun et al., 2014). The model also replicates observations that the locking process of the upper plate is starting early in the seismic cycle but the trenchward motion of the upper plate continues several decades after the great earthquake6 (Figure 3.4 e-g).

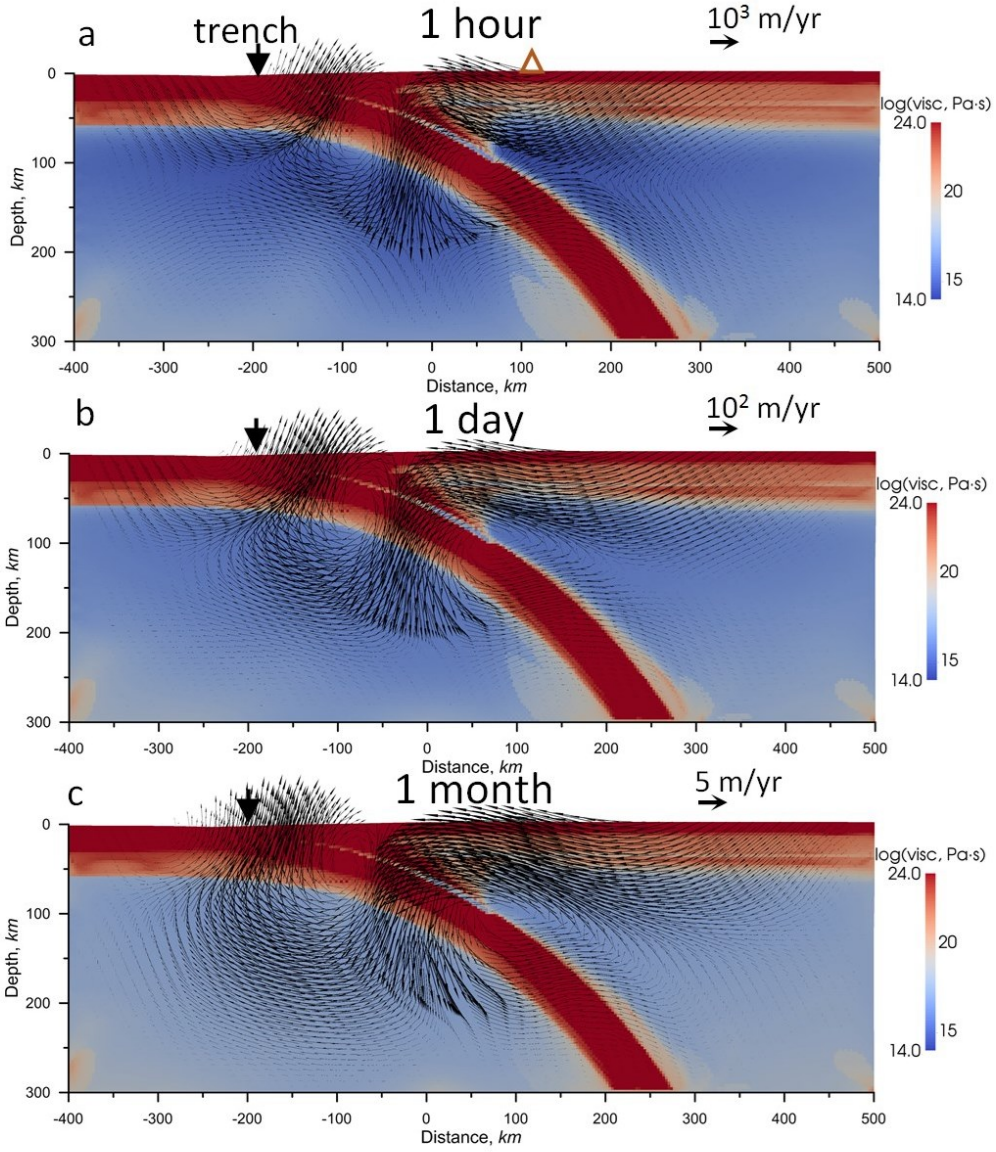

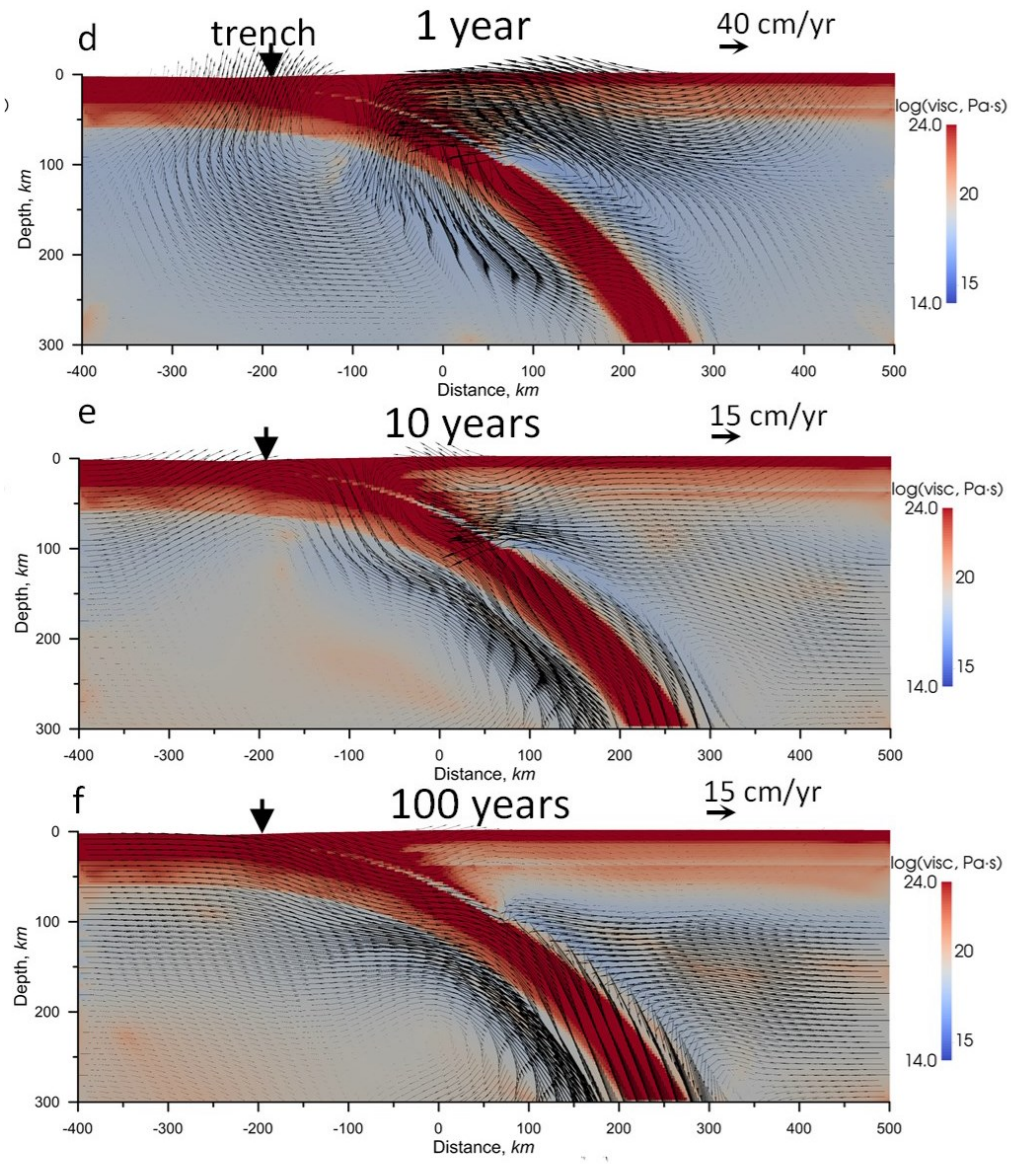

Figure 3.4 (a)-(f) Snapshots of the spatial distributions of viscosity (background colors) and velocities (vectors) for the different stages of the seismic cycle from 1 hour (a) to century (f) of the typical earthquake (Mw9.3) generated by the reference non-linear transient model. Note different scales of the velocity vectors. Red triangle at the surface indicates position of the virtual GPS station located about 300 km landwards from the trench.

However, perhaps the most striking result of the model is the dramatic drop of the viscosity in the large domain of the mantle wedge just after the onset of the earthquake. While

minimum viscosity in the mantle wedge during the inter-seismic period in our model is approximately 10^{18} Pa·s, it drops to about 10^{14} Pa·s after the earthquake. This decrease is a result of the stress imposed on the mantle wedge due to the elastic deformation of the earthquake. Stress is increasing by more than 10-15 times in the large volume of the mantle (Figure 3.5), which translates to the viscosity drop of about 3 orders of magnitude because of the power-law rheology of the mantle rocks. The additional order of magnitude decrease is due to the transient creep strain rate amplification (2.1.3). Later during the postseismic phase of the seismic cycle viscosities gradually increase following a relaxation of stress in the wedge, approaching their steady (interseismic) values about a decade after the earthquake (Figure 3.4 and Figure 3.6).

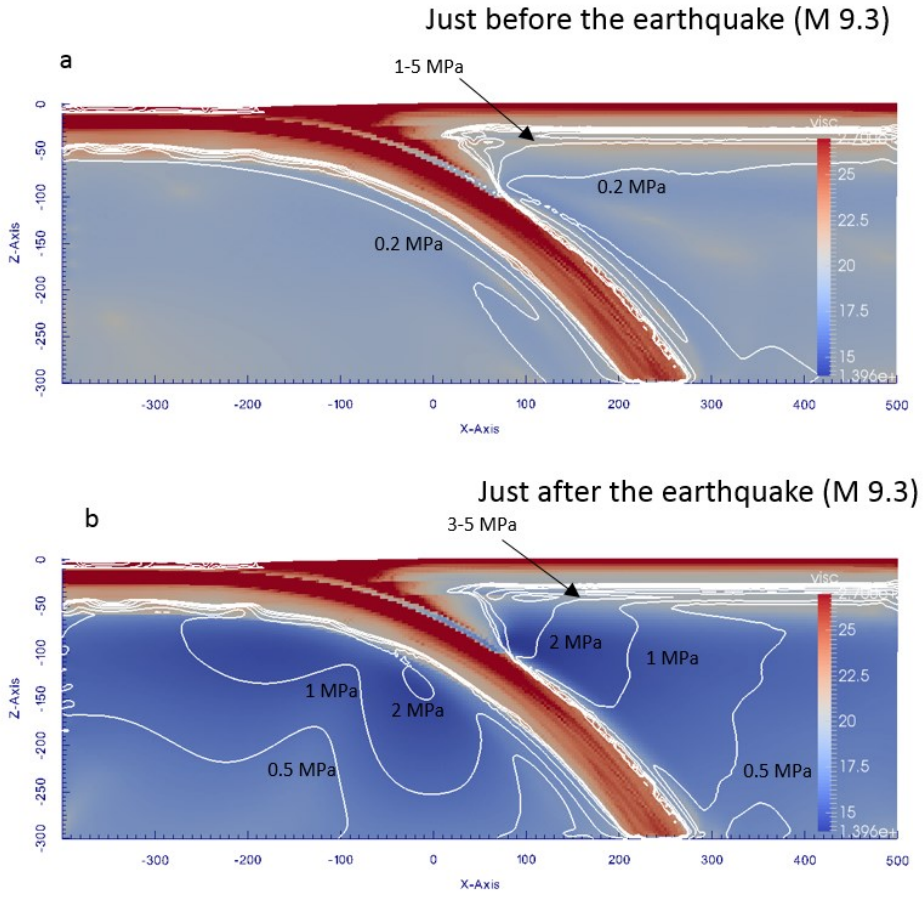

Figure 3.5 Snapshots of the spatial distribution of viscosities (background colors) and stresses (contours) in the reference model of the Mw 9.3 earthquake just before (a) and just after (b) the earthquake.

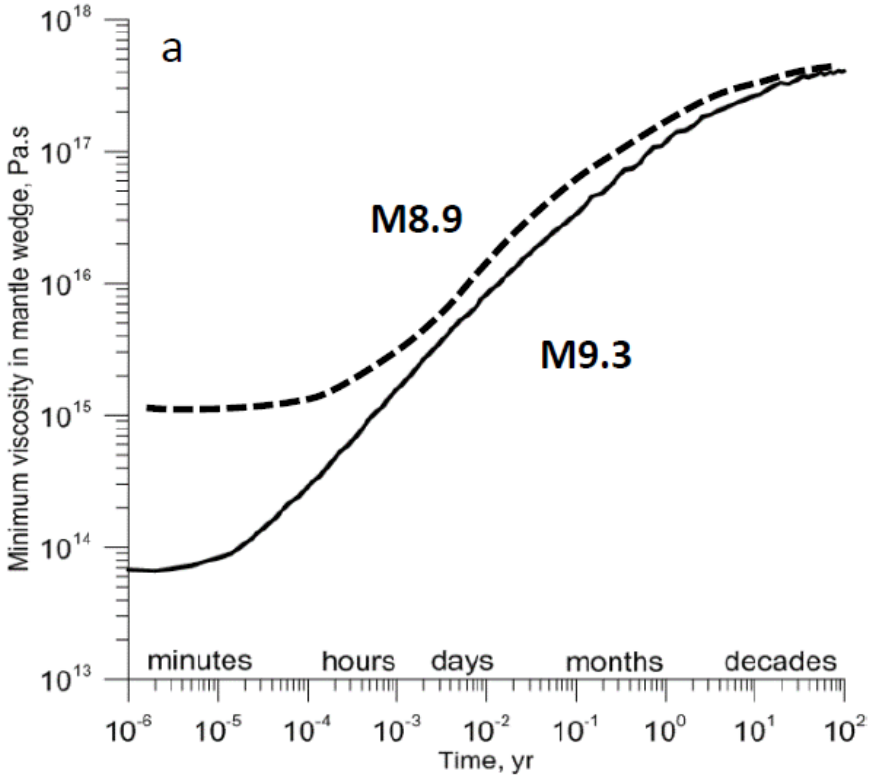

Figure 3.6 Time evolution of the minimum viscosity in the mantle wedge during the seismic cycles of the Mw9.3 (reference model solid line) and Mw8.9 (dashed line) earthquakes generated by the non-linear transient models.

For the smaller earthquake (Mw about 8.9), the viscosity drop is less because of the less dramatic stress increase (Figure 3.7), but it is still as large as 2.5 orders of magnitude (Figure 3.6). As we will see from the following analysis, this dramatic drop of viscosity results in a much earlier emergence of the large-scale viscoelastic relaxation process in the mantle wedge than it is currently believed.

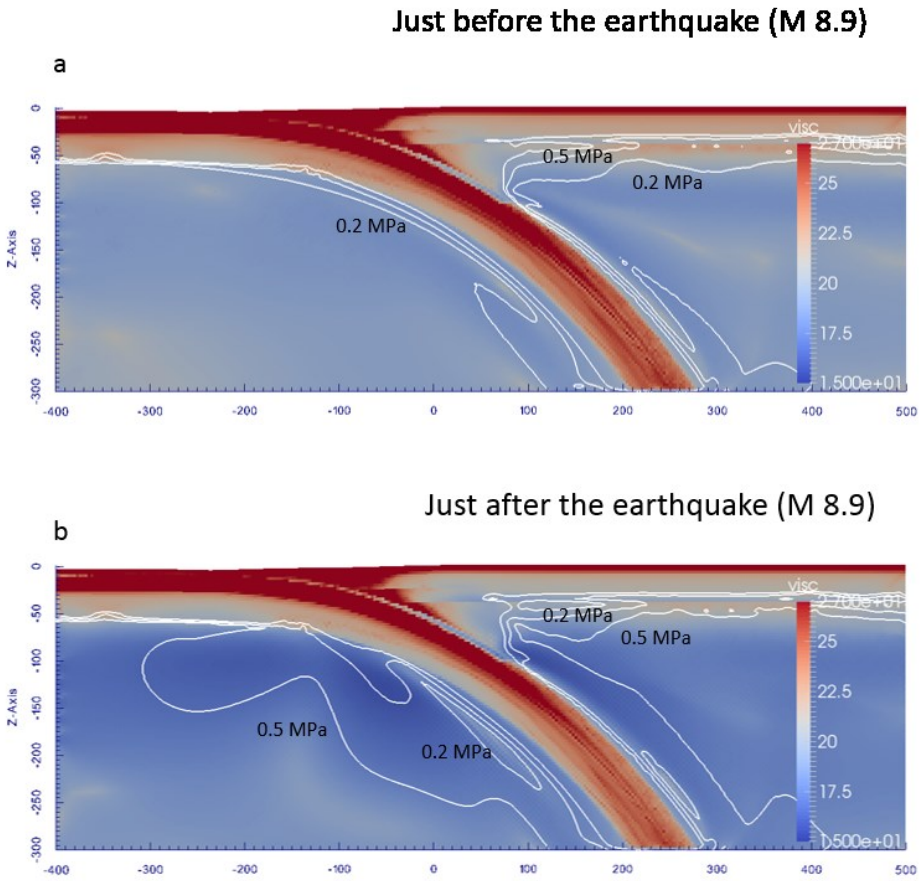

Figure 3.7 Snapshots of the spatial distribution of viscosities (background colors) and stresses (contours) in the reference model of the Mw 8.9 earthquake just before (a) and just after (b) the earthquake.

3.2 Comparison with Conventional Model

In conventional models of viscoelastic relaxation, viscosity in the mantle wedge is assumed to be either constant (linear Maxwell viscous model) or changing by up to 10-20 times according to a linear transient viscous (Burger's) model (Wang et al., 2012). In order to compare results of our model with the conventional models, we run models with the accordingly simplified rheology in the mantle but with all other parameters being the same as in our reference model. Similar to our reference model these models with simpler rheology generate sequences of earthquakes with comparable seismic moments, stress drops and recurrence times. We compare horizontal velocities for the three models at a virtual GPS station located at a distance of 300 km landward from the trench (Figure 3.8). Shown are velocities for all earthquakes in all three model types. Velocities in the reference model (black

circles in Figure 3.8), are controlled by the continuing rupture propagation, and afterslip in the shallow part of the fault during first 10 minutes after the main earthquake shock, but after just one hour following the earthquake viscoelastic relaxation in the mantle wedge becomes the dominant deformation process (see also Figure 3.4 b-f). Interestingly, in this model velocities decay with time as $t^{-0.85}$ in a large time interval, from an hour until years after an earthquake. Such a decaying behavior is similar to, and could be easily mixed with the hyperbolic decay-law typical for the fault-controlled afterslip process (Marone et al., 1991; Pefettini and Avouac, 2004).

In contrast to our reference model, which employs transient power-law rheology in the mantle wedge, in the model with linear transient rheology (purple circles in Figure 3.8) viscoelastic relaxation in the mantle wedge becomes the dominant deformation process only much later (after months) in the postseismic phase. In the model with the constant viscosity in the mantle wedge of $3 \cdot 10^{18}$ Pa·s (green circles in Figure 3.8), viscoelastic relaxation becomes dominant even later, years after the earthquake. So the clear difference of our non-linear model from the conventional linear rheological models is a much earlier emergence of the viscoelastic relaxation process.

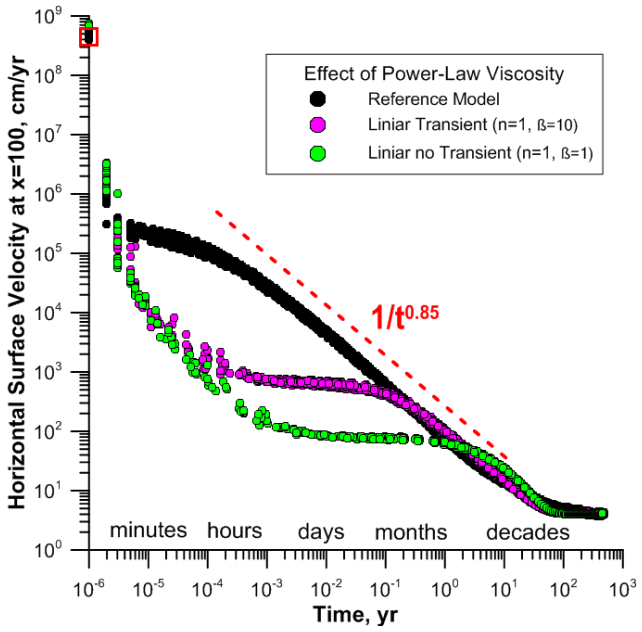

Figure 3.8 (see below) Time evolution of the horizontal surface velocities at the virtual GPS station located 300 km landward from the trench during seismic cycles of the earthquakes generated by different models. Black solid circles correspond to the reference-non-linear transient model, red solid circles correspond to the linear transient model and green solid circles to the linear non-transient model. Note log-log scale of the axes. Red dashed line shows $1/t^{0.85}$ function trend.

3.3 Comparison with Afterslip Models

All models that we have so-far presented do not contain a rate strengthening RS domain, which may exist at megathrust faults deeper than 40-45 km (Scholz, 1998) and which is believed to be responsible for the afterslip at the fault (Scholz, 1998; Wang et al., 2012; Marone et al., 1991; Perfettini and Avouac, 2004). To test its effect we have added the rate strengthening RS domain in the deep part of the fault in our reference model without changing all other parameters. The resulting model we hereafter call the afterslip reference model. In Figure 3.9 (left) we compare postseismic horizontal velocities at a virtual GPS station on the surface of the reference model (black circles) with velocities in the afterslip reference model (red circles). For this comparison we have chosen events with identical seismic moments. The models are clearly distinguishable during the first few tens of minutes following the earthquake, but become identical after an hour and later. This demonstrates that even if the classical afterslip process is acting at the fault, the viscoelastic relaxation in the mantle wedge with transient power-law rheology becomes a dominant deformation process already since an hour or so after an Mw 9.3 earthquake. The same analysis for the smaller earthquake (Mw 8.9) shows that in this case viscoelastic relaxation in the mantle wedge becomes a dominant deformation process later, but still as early as few days after the earthquake Figure 3.9 (right)).

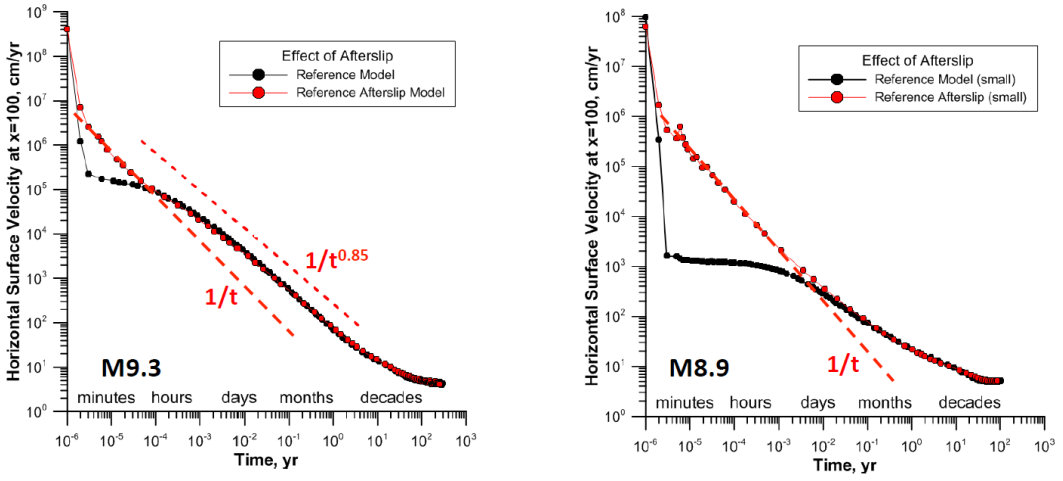

Figure 3.9 (left) Comparison of time evolution of the horizontal surface velocities at the virtual GPS station located 300 km landward from the trench during seismic cycles of the earthquakes of the same seismic moments for the two models, reference Mw9.3 model (black points) and the afterslip reference model, i.e. a model including rate strengthening interval of the subduction fault deeper than 42 km. (right) The same as (left) but for the smaller magnitude Mw8.9 model.

3.4 Application for Valdivia Earthquake, Chile 1960

In this study we do not intend to model specific events in details. To do that properly we would need to extend our 2D model to 3D. Nevertheless, we use Chile 1960 event to calibrate our parameters by reproducing its integrated characteristics like seismic moment, recurrence time and stress drop.

Interestingly our Chile 1960 model demonstrates prolonged postseismic deformations in agreement with the GPS observations (Khazaradze, et al., 2002) suggesting trenchward motion of the overriding plate 300-400 km landward from the trench 35 years after the event.

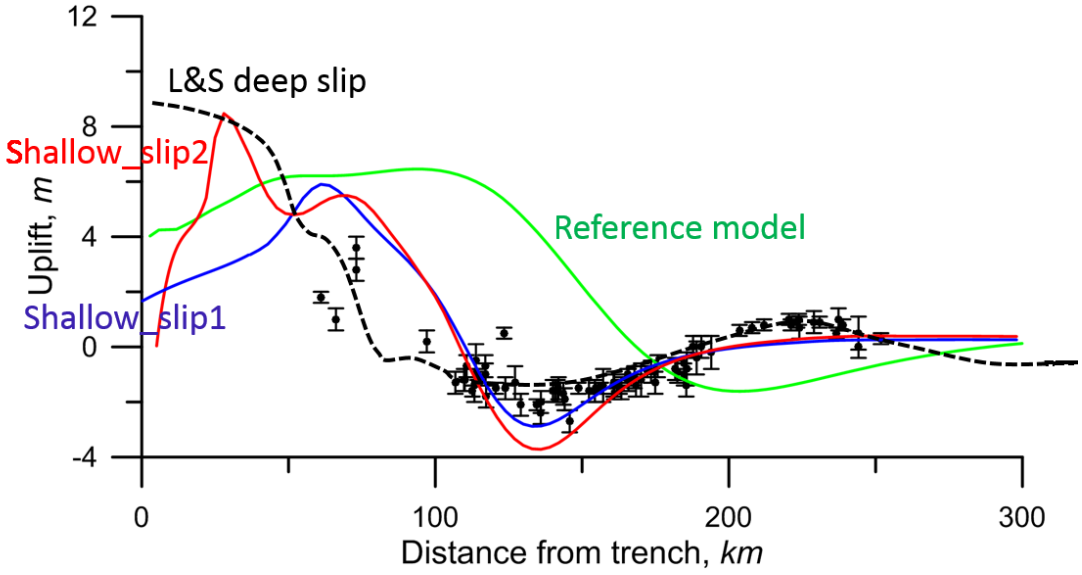

Figure 3.10 Postseismic uplift after Chile 1960 earthquake as function of distance to the trench. Black dots with error bars are geodetic data (Plafker and Savage, 1970). Curves denote predictions of reference model (green curve), shallow-slip model 1 (blue line), shallow-slip model 2 (red line) as well as deep and shallow slip model (Linde and Silver, 1989).

We have also run several models aimed to better fit the sparse geodetic data available for the Chile 1960 event (Plafker and Savage, 1970). Figure 3.10 shows observed vertical displacements from geodetic observations (Plafker and Savage, 1970) for Chile 1960 event together with models predictions. Our reference model with unlimited at depth rate-weakening regime (constant (b-a)*=4*10^{-4}), shown by green curve, correctly reproduces magnitude of the uplift, but overestimates wavelength of the surface deformation. Models with both rate-weakening and rate-strengthening regimes ((b-a)*= 0, at depth<9km, 6*10-4at 9km<depth < 33km and -1.2*10-3 at depth > 33km, blue curve and (b-a)*=6*10-4at 0<depth < 33km and -1.2*10-3 at depth > 33km,, red curve) fit observations better. These models generate more shallow slip at the fault than our reference model and therefore the viscosity drop in mantle

wedge appears somewhat lower than in reference model (3.5 orders of magnitude instead of 4 orders of magnitude). Note however, that there is a remarkable discrepancy between seismic and geodetic magnitudes of Chile 1960 event (9.5-9.7) versus 9.3. In attempt to reconcile these observations study (Sun and Wang, 2015) has suggested even deeper slip at the fault than in our reference model (black dashed curve). This model likely produces even larger viscosity drop than our reference model. Anyway it is clear that expected magnitude of viscosity drop is very high, between 3.5 and 4+ orders of magnitude for the extreme event like Chile 1960.

3.5 Interpretation and Application for Tohoku Earthquake

Our results contradict the conventional view that viscoelastic relaxation becomes prominent only months or even years after a great earthquake (Scholz, 1998; Wang et al., 2012; Burgmann and Dresen, 2008). If our model is correct, why then can conventional models successfully fit the observations? It is clear from Figure 3.8, Figure 3.9 and Figure 3.11 that surface velocities in the region above the central and deep parts of a fault during the first few months or even a year in our reference model can be easily misinterpreted as resulting from afterslip because of the similar decay laws for both processes. Note that in fact an afterslip is a dominant deformation mechanism only during the first hour in the Mw 9.3 model (Figure 3.9a) and only during first few days in Mw 8.9 model (Figure 3.9b). Note also that since a month or so after the earthquake the viscosity in the mantle wedge in our model is changing by about 10 times which is quite similar to the viscosity change required to fit observations in the conventional models of viscoelastic relaxation.

In order to minimize geometrical effects we normalize the displacements for each station by its cumulative displacement during one year after the event. Normalized displacement curves for all stations plot in rather narrow band and are shown by black curves in Figure 3.12b. Note logarithmic time scale in Figure 3.12b that highlights displacements at small times. All displacement curves show significantly higher velocities shortly after the event: More than one third of the yearly displacement occurs during first month after the event. Blue curves show the displacements at three virtual GPS stations (large blue circles in Figure 3.12a) predicted by our reference model for the event with Mw 9.3. We see that this model suggests that about half of the yearly displacement would occur already during the first month after the event, instead of the one third observed. From that we conclude that the Mw 9.3 model predicting 4 orders of magnitude drop of viscosity is clearly falsified for the case of Tohoku event. However, the predicted displacements for the model of the event with the Mw 8.9 (purple curves), more representative of the Tohoku event, fit the observations remarkably well for the entire time range including the first days to month.

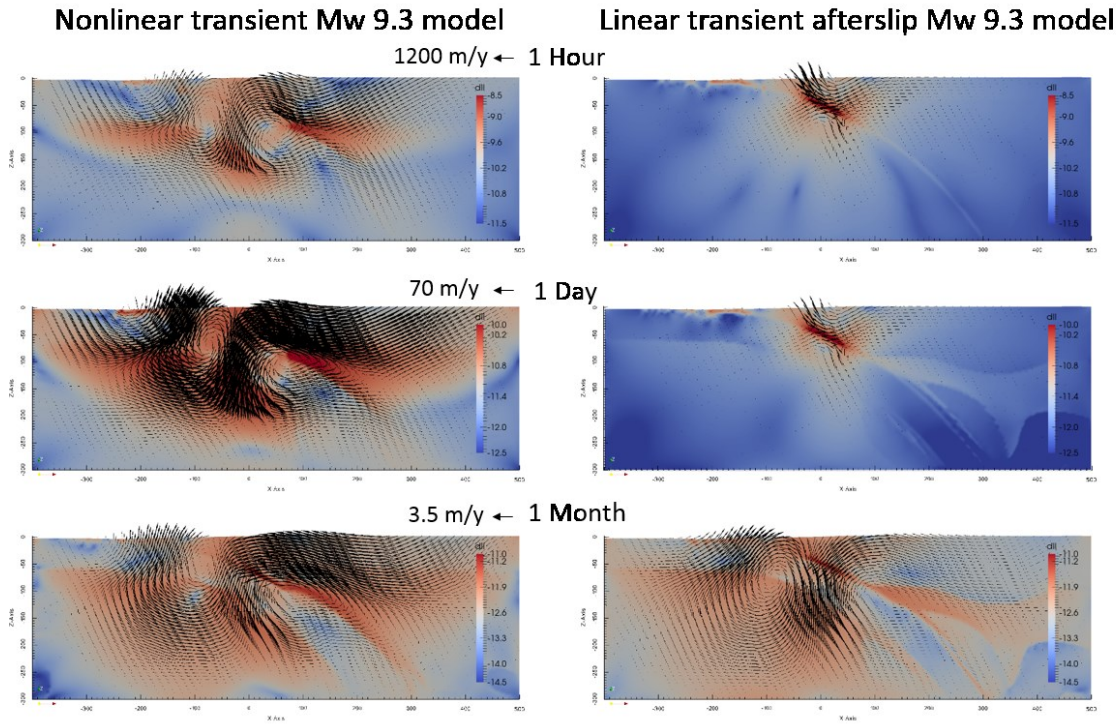

Figure 3.11. Comparison of the deformation processes after a Mw 9.2 earthquake for the non-linear transient model (left column) and linear transient afterslip model (right column). Shown are snapshots of the spatial distributions of strain rates (background colors) and velocities (vectors) for the different stages of the postseismic relaxation from 1 hour to 1 month. Note much larger actively deforming domain in the non-linear model.

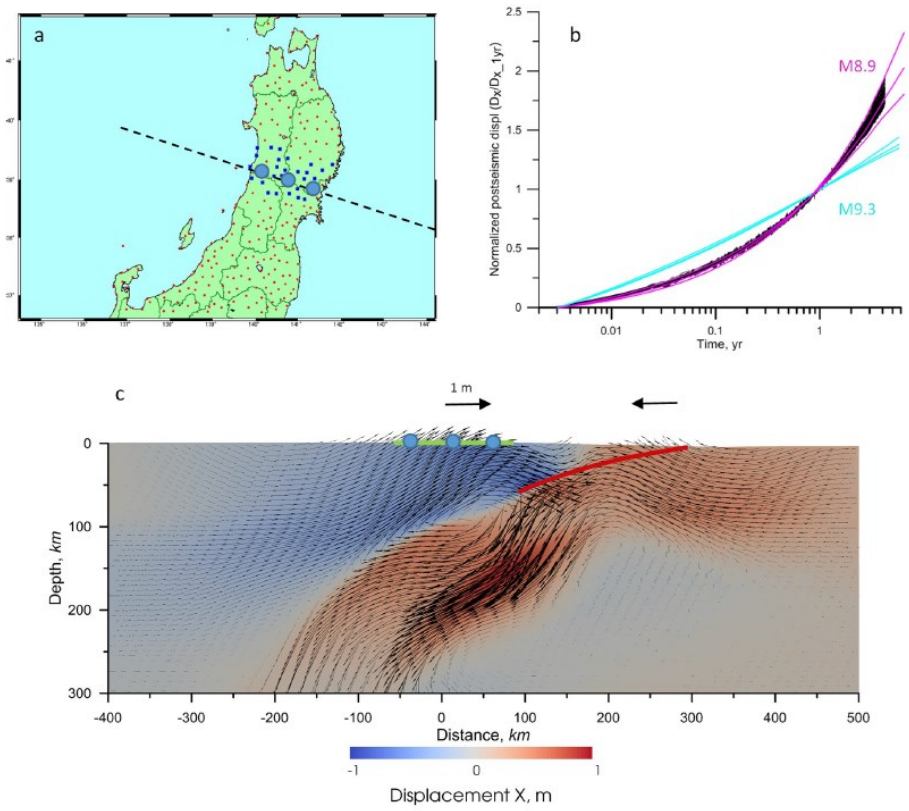

Figure 3.12. (a) Location of the GPS stations (small blue points) used for the comparison of the displacements after the Tohoku 2011 earthquake with the models. Dashed line shows the surface trace of the model 2d profile and large blue circles show virtual GPS stations on the model profile. (b) Time evolution of the normalized trench-perpendicular observed postseismic horizontal displacements (black curves) versus calculated horizontal displacements at 3 virtual GPS stations for the Mw9.3 reference model (blue curves) and Mw8.9 model (red curves). All displacements are trench-perpendicular, and are calculated relative to the position of the stations at the next day after the Tohoku 2011 event and are normalized by the displacements at 1 year after the event. We used daily solutions from ref.28. Note logarithmic scale of the time axis. Fit of the Mw8.9 model to the observations is very good for the entire 1day to 4year time range. (c) Spatial distribution of the horizontal displacements (background colors) and displacement vectors (arrows) 2.5 years after the event in Mw8.9 model. The red line shows subduction fault. Note about 0.5 m landward displacement of the upper plate domain close to the trench and about double as large displacement of the virtual land GPS stations in the opposite direction. Note also downward displacement of the surface of the upper plate some 100 km landward from the trench. All these modeling results agree well with the observations Watanabe et al., 2014; Sun et al., 2014.

In Figure 3.12c we show our model for the Mw 8.9 event at the time of 2.5 years after the earthquake. The colors represent horizontal displacements and arrows show displacement vectors. The model reproduces major features of the postseismic deformations after the Tohoku event (Watanabe, 2014; Sun et al., 2014): The landward displacement of the offshore upper plate region near the trench and downward displacement of the marginal part of this region.

3.6 Model Limitations

The largest model limitation is its two dimensionality that does not allow comparing model predictions with important details of observations. For instance, surface coseismic displacements of Tohoku 2011 event clearly show 3D effects. Postseimic deformations are more evenly distributed in space but also have some 3D features. Therefore, we are forced to use only normalized displacements to study the time evolution of mantle rheology with our 2D model.

Another important limitation of our current models is their relatively low resolution that does not allow us to resolve properly the processes of rupture nucleation and propagation. In the future, much higher resolution within the subduction channel (about 0.1 km of grid point spacing) should be implemented. Further limitation of the present modeling technique is that we calculate inertial term in explicit procedure. This works well at time steps larger than 10s, but shows bad convergence at smaller time steps. In the present modeling, where the smallest time step is 40 s this does not matter. However, for modeling of rupture propagation inertial term should be fully incorporated in implicit numerical procedure.

3.7 Conclusion

In order to study postseismic relaxation we had tested models with different setups for rate-and-state friction: 1) unlimited velocity-weakening friction all over the depth of the subduction channel and 2) with rate-strengthening friction after depth of 42 km. Also, we tested viscosity laws, i.e. transient rheology, power-law rheology and linear rheology.

Our reference model (transient non-linear viscosity) predicts that the viscosity in the mantle wedge drops by 3 to 4 orders of magnitude during a great earthquake with magnitude above 9. This drop in viscosity results in spatial scales and timings of the relaxation processes following the earthquakes that are significantly different to previous estimates. These model is consistent with the major features of postseismic surface displacements recorded after the Great Tohoku Earthquake.

The key feature of our model is non-linear viscous rheology. In this respect we follow, confirm and further develop the pioneering study (Freed and Burgmann, 2004) and its extensions (Freed et al., 2006; Freed et al., 2007), by showing that viscosity drop in the mantle

can be even larger than previously suggested. Our model is also supported by the recent discovery that the viscoelastic relaxation in the mantle has controlled postseismic deformation at least since one month after the Great Tohoku earthquake and that the afterslip downdip of the rupture zone might have been substantially overestimated (Sun et al., 2014).We infer that even at the time range from one hour to a month after the great earthquake, viscoelastic deformation may be very active and therefore the deforming domain may be much larger than previously thought and imaged with the conventional linear models.

This finding may have implications for the triggering or delayed triggering of the distant earthquakes (Freed, 2005) and volcanic eruptions. Furthermore, an increase of the stress accompanied by the increasing of dislocation density in the rocks of the mantle wedge during the earthquake may increase seismic wave attenuation (Farla et al., 2012), thus diminishing the magnitude of ground-shaking during the great earthquakes.

We also note that our results demonstrate that there is no contradiction between extremely low mechanical coupling (effective friction coefficient of 0.015) at the subduction megathrust in South Chile inferred from long-term geodynamic model (Sobolev and Babeyko, 2005) and appearance of sequence of the largest earthquakes, like Great Chile Earthquake of 1960.

Chapter 4 Estimation of Maximum Magnitudes of Subduction Earthquakes

4.1 Observations and Concepts

Giant earthquakes (GEQ; moment magnitude Mw>=8.5) are observed only in subduction zones. Even though methods of instrumental observations of earthquakes in subduction zones have been improved in recent decades, characteristic recurrence time of giant earthquakes is much larger than period of observations and does not allow to spot clearly necessary conditions for giant earthquakes. Previous hypotheses of GEQs genesis are based on observations, statistical analysis and theoretical considerations. There are different opinions about the role of subduction zone parameters in producing GEQs.

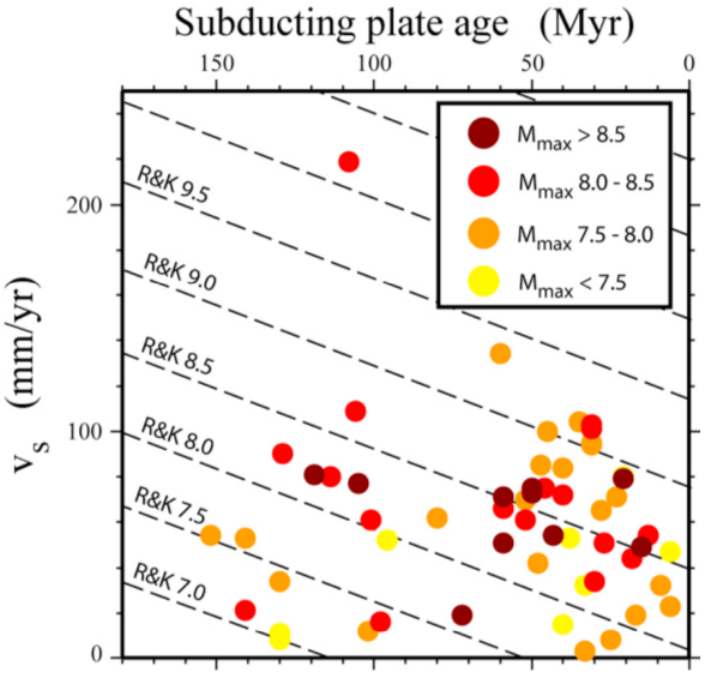

Figure 4.1 Relation between the subduction velocity v_s, slab age, and M_{max}. Dashed lines are theoretical M_{max} limits, as estimated by Ruff and Kanamori (1980). From Heuret et al., 2011.

Based on the observations available in 70-th years of 20-th century Keheller et al. (1974) has proposed that the key factor is the width of the seismogenic zone. They suggested

that slabs dipping with low angles have largest contact area with the overriding plates which allows GEQs. Ruff and Kanamori (1980) suggested that maximum earthquake's magnitude is controlled by two parameters: age of subducting plate and plate convergence rate. They based their analysis on the sparse data on the great earthquakes available at that time and previous work including study by Keheller et al. (1974) and analysis of the different types of subduction in Pacific by Ueda and Kanamori (1979). The main assumption of Ruff and Kanamori (1980) was that magnitude of earthquakes was directly related to the strength of mechanical coupling between subducting and overriding plates. Since strength of mechanical coupling depends on normal component of the stress at the fault and the area of contact, combination of relatively high rate of loading and young age of subducting plate leading to its low buoyancy, creates wide zone with the necessary high normal stress at the fault. This view was supported by many researches since then, and in a way became "classical" until a number of great earthquakes, and particularly two largest earthquakes of the last 12 years Great Sumatra/Andaman 2004 Earthquake and Tohoku 2011 earthquake have violated the suggested correlation. Figure 4.1 shows "classical" expected correlation by Ruff and Kanamori (1980) together with the observations according to Heuret et al. (2011). Very poor fit of the data to the predictions is obvious. This raises a question of what is wrong with the concept by Ruff and Kanamori (1980) that looked so logical and was so popular for the long time. Addressing this question is one of the purposes of this work.

Ruff (1989) has extended concept by Ruff and Kanamori (1980) by suggesting additional (to subduction velocity and slab age) factor controlling appearance of great earthquakes, i.e. thickness of sedimentary layer at trench. He noticed that most of the great earthquakes occurred in subduction zones with thick sedimentary cover at the trench. He interpreted these observations as an indicator of coherence/smoothness of subduction interface allowing rupture propagation to a large distance. Unlike the concept on effect of subduction velocity and slab age, the idea about effect of sediments in subduction zones on origin of great earthquakes has been confirmed by the later observations (Heuret et al., 2012 and references therein). Thus it was demonstrated (Heuret et al. 2011 and 2012), that earthquakes with Mw>=8.5 are observed only at subduction zones where the sediment thickness at trench is larger than 0.5 km (Figure 4.2). This outcome is supported by the observation that all subduction zones with registered earthquakes with magnitude more than 8.5 have rather smooth subducting sea floor (Wang and Bilek, 2014). It is inferred that thick sediments form laterally-homogeneous layer that smooth subducted sea-floor relief and strength–coupling asperities, thereby creating a large coupling zone. Another interesting observational constraint is that GEQs occur mostly in the subduction zones with neutral upper plate strain, less frequently in the zones with compressive upper plate strain and never at extensive (Heuret et al., 2012) (Figure 4.2). This was interpreted so that moderate tectonic compressive stresses acting at smooth slab surface, should be high enough to allow frictional stresses to accumulate, but low enough for rupture propagation not to be inhibited (Heuret et al., 2012).

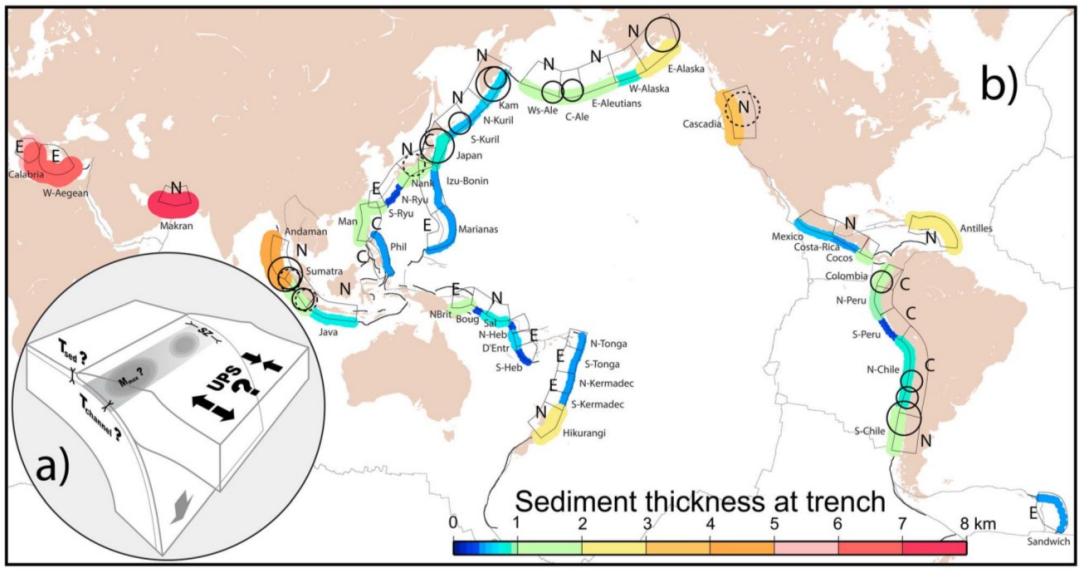

Figure 4.2 . (a) Possible relationships between subduction megathrust earthquakes, trench sediment thickness and upper plate strain. Abbreviations: Upper plate strain (UPS), thickness of sediments in the trench (Tsed), thickness of the subduction channel (Tchannel), maximum earthquake magnitude (Mmax), and seismogenic zone (SZ). (b) Map of the 44 trench segments defined by Heuret et al. [2011], showing the variability of Tsed (colors) and UPS (E = Extensional, N = Neutral, C = Compressive). Black circles show the location of Mw ≥ 8.5 subduction interface earthquakes (area scales with magnitude). Preinstrumental events are represented by dashed circles. From Heuret et al., 2012.

It is important to relate thickness of the sediments to the mechanical properties. Geodynamic analysis (Lamb and Davies, 2003, Lamb, 2006) and geodynamic modeling (Sobolev and Babeyko, 2005, Sobolev et al., 2006) suggest that sediments in subduction channel in a way lubricate subduction interface by decreasing there static friction coefficient. Sobolev et al. (2006) estimated relation between static friction coefficient in the subduction channel and thickness of the sediments. To do so they combined results of their geodynamic models with geodetic data on the depth of locking of subduction interface in Central and South Andes (Khazaradze and Klotz, 2003) and data on the thickness of sediments in the trench (Hoffmann-Rothe et al., 2006) to (Figure 4.3). They infer that effective static friction coefficient is very low (about 0.015) if thickness of the sediments in the trench is higher than about some 1.5 km and it increases to about 0.05 when sedimentary layer thins from 1-1.5 km to 0. In our model we will use this semi-empirical correlation.

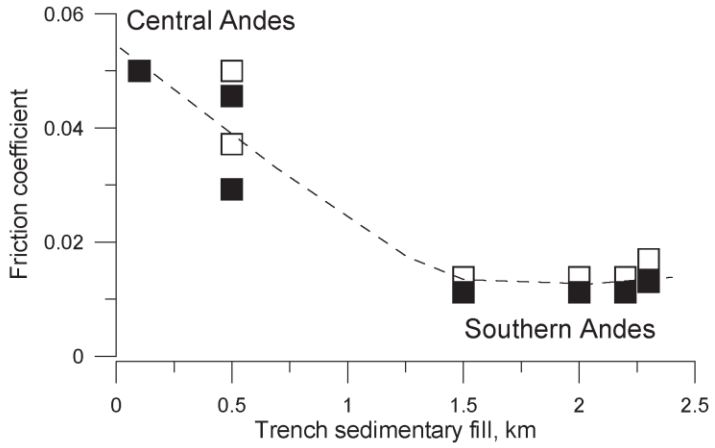

Figure 4.3 Estimated interpolate friction coefficient versus observed thickness of the sedimentary trench-fill between 20 and 40°S. From Sobolev et al., 2006.

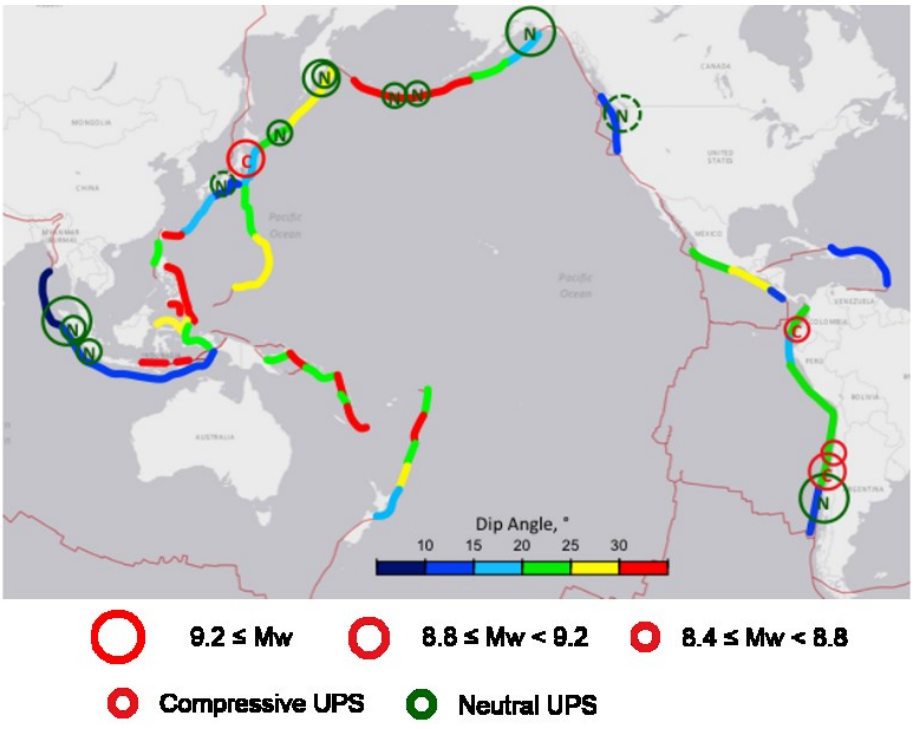

Figure 4.4 Along-trench variability of the dipping angle. Circles show the location of Mw ≥ 8.4 subduction interface earthquakes (area scales with magnitude, color denotes upper plate strain regime). Modified from Heuret et al., 2011 and 2012.

Heuret et al. (2011) and Schellart and Rawlinson (2013) found weak correlations of maximum observed Mw to inclination angle of subduction and width of seismogenic zone. However, the correlation (pointed out earlier by Keheller et al., 1974) is becoming evident if only events with magnitude higher than 8.5 are considered (Figure 4.4). In the last hundred years earthquakes with magnitude more than 8.5 occurred only in subduction zones with width more than 75 kilometers (dipping angles less than 35°), and earthquakes with magnitude more than 9.2 in zones with width more than 150 kilometers and dipping angles less than 35° degrees. All 3 mentioned sets of observation, i.e. dipping angles, sedimentary thicknesses and strain regimes in the upper plate are combined in Figure 4.5.

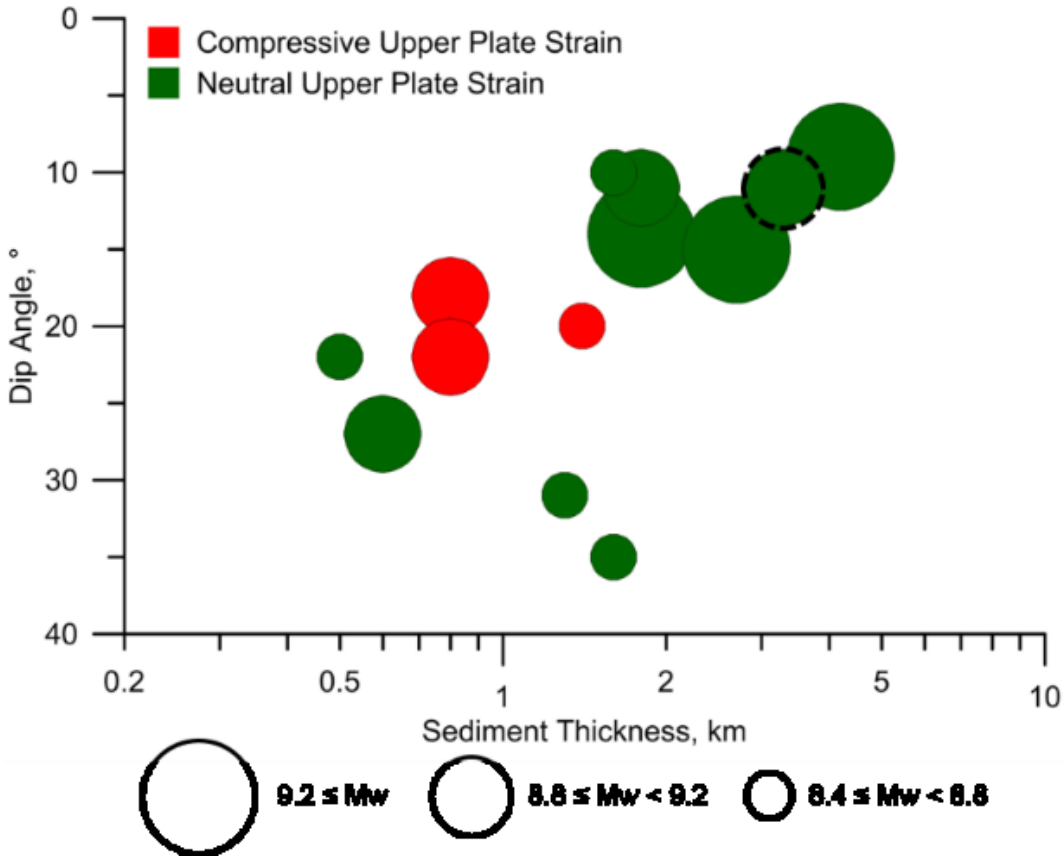

Figure 4.5 Relation between the subduction dipping angle, sediment thickness, M_{max}, and UPS regime for the largest observed earthquakes in every subduction segment. Preinstrumental event (Cascadia 1700) is represented by dashed circle.

4.2 Key Questions and Modeling Strategy

We apply our cross-scale modeling technique to study factors that control magnitude of the largest possible events at subduction zones. In particular we are going to address the following questions that arise from the accumulated observations about the GEQs that were briefly summarized above.

1. What is the effect of the subduction zone dipping angle on the magnitudes of GEQs?
2. What is the effect of static friction (sediments) at the subduction interface on the magnitudes of GEQs?
3. What is the effect of subduction velocity on the magnitudes of GEQs?
4. Why do the GEQs occur preferably in subduction zones where upper plate has neutral strain or (less frequent) compressive strain and never when strain is extensive?
5. What is the role of mechanical coupling in GEQs and what appeared to be wrong with the apparently logical and intuitive concept of Ruff and Kanamori (1980)?

Till now our RSF parameters have been calibrated for the case of South Chile and Chile 1960 event, i.e for particular effective static friction of 0.015 estimated from the long term geodynamic models (Sobolev and Babeyko, 2005; Sobolev et al., 2006). Now we must decide how to extend our models for other subduction zones with different friction in subduction channel. The equation for the effective friction in the channel is given as equation 1.35.

The static friction in the channel is controlled by the fluid pressure factor (equation 1.35). According to (Sobolev et al., 2006) it is that factor, which may change static friction from 0.015 in South Andes where subduction channel is filled with the sediments to 0.05 in Central Andes, where there is almost no sediments in subduction channel. This corresponds to 3.3 times change in the fluid pressure factor. Now there are two possibilities how to treat dynamic part of the effective friction. (1) We fix b and a RSF parameters according to our calibration for South Andes and use these particular values for other subduction zones with possibly higher fluid pressure factor. However the consequence of this modeling strategy will be changing of the dynamic part of friction coefficient and therefore also stress drop during the earthquakes proportional to the fluid pressure factor. As a result we will obtain stress drop for the events in Central Andes by 3.3 times higher than in South Andes, i.e about 3.3X 5 MPa= 16.5 MPa, which do not agree with observations suggesting similar stress drops for the great Earthquakes for all subduction zones. (2) Another strategy will be to keep constant the dynamic part of the effective friction coefficient. In this case we will automatically get similar

stress drops for the events at all subduction zones with different static frictions. Here we will take this later strategy, as it better fits observations. For all our models we will adopt the values of affective RSF parameters, which we have estimated for South Andes, case.

Similar to the case of South Andes model we consider two options for the depth dependence of RSF parameters. Option 1: depth unlimited rate weakening with constant (b-a)* and b/(b-a) parameters. Option 2: Rate weakening with constant (b-a)* and b/(b-a) parameters till the depth where temperature in the channel reaches 350°C and deeper the rate strengthening with constant (b-a)* and b/(b-a) parameters of $-4 \cdot 10^{-4}$ and 4, respectively.

4.3 Effects of Dipping Angle, Static Friction Coefficient and Subduction Velocity

We use the same procedure as that is described in 2.1 to prepare long-term subduction models with the slabs dipping at different angles. In first set of models we use the same age of lithospheric plates and same convergence velocities to exclude effects, which are not related to geometry and static friction. We consider 5 types of geometries. The corresponding long-term models are shown in Figure 4.6. For each particular geometry, we consider 5 models with static frictions of 0.015, 0.02, 0.03, 0.04 and 0. 05. For each model we simulate seismic cycles in the same way as described in 2.2. Figure 4.7 shows sets of simulated seismic cycles (2D seismic moments vs. time) for all models, and Figure 4.8 displays pares of snapshots for the models of different geometries at the time of earthquake and time of interseismic locking. Maximum and average seismic moments for the cycles for all subduction geometries and static friction angles are shown in Figure 4.9. It is clear that it is the slab geometry that has the largest effect on the seismic moment of earthquakes. The smaller is the slab's dipping angle the larger are the seismic events. Static friction has smaller, but still significant effect. The seismic moments are larger in subduction zones with lower effective friction coefficients. It is important that these results do not depend significantly on the type of the depth dependency of RSF (b-a)* parameter. We get basically the same results for the model with depth unlimited rate weakening (Figure 4.9) and with rate strengthening deeper than depth of isotherm of 350°C (Figure 4.10).

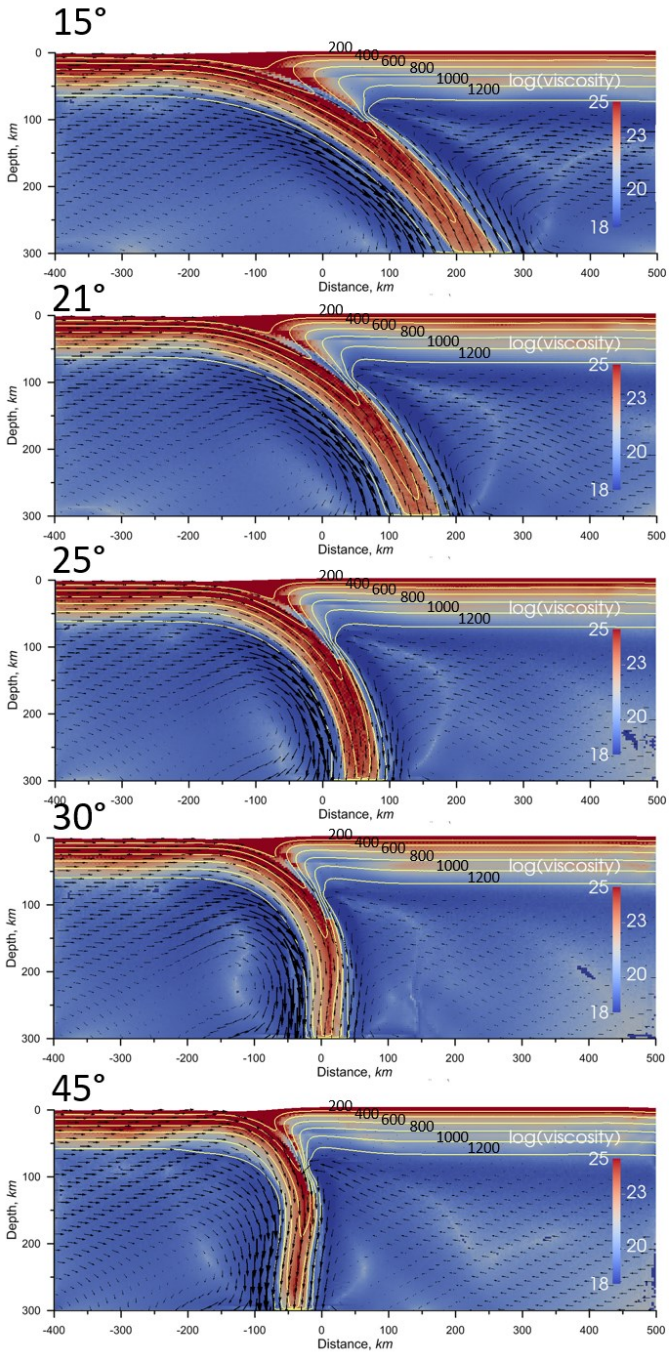

Figure 4.6 Snapshots of the spatial distributions of viscosity (background colors), temperature (yellow isolines from 200°C to 1200°C every 200°C), and velocities (vectors) in the long-term thermo-mechanical models of subduction with dipping angles 15°, 21°, 25°, 30°, and 45°.

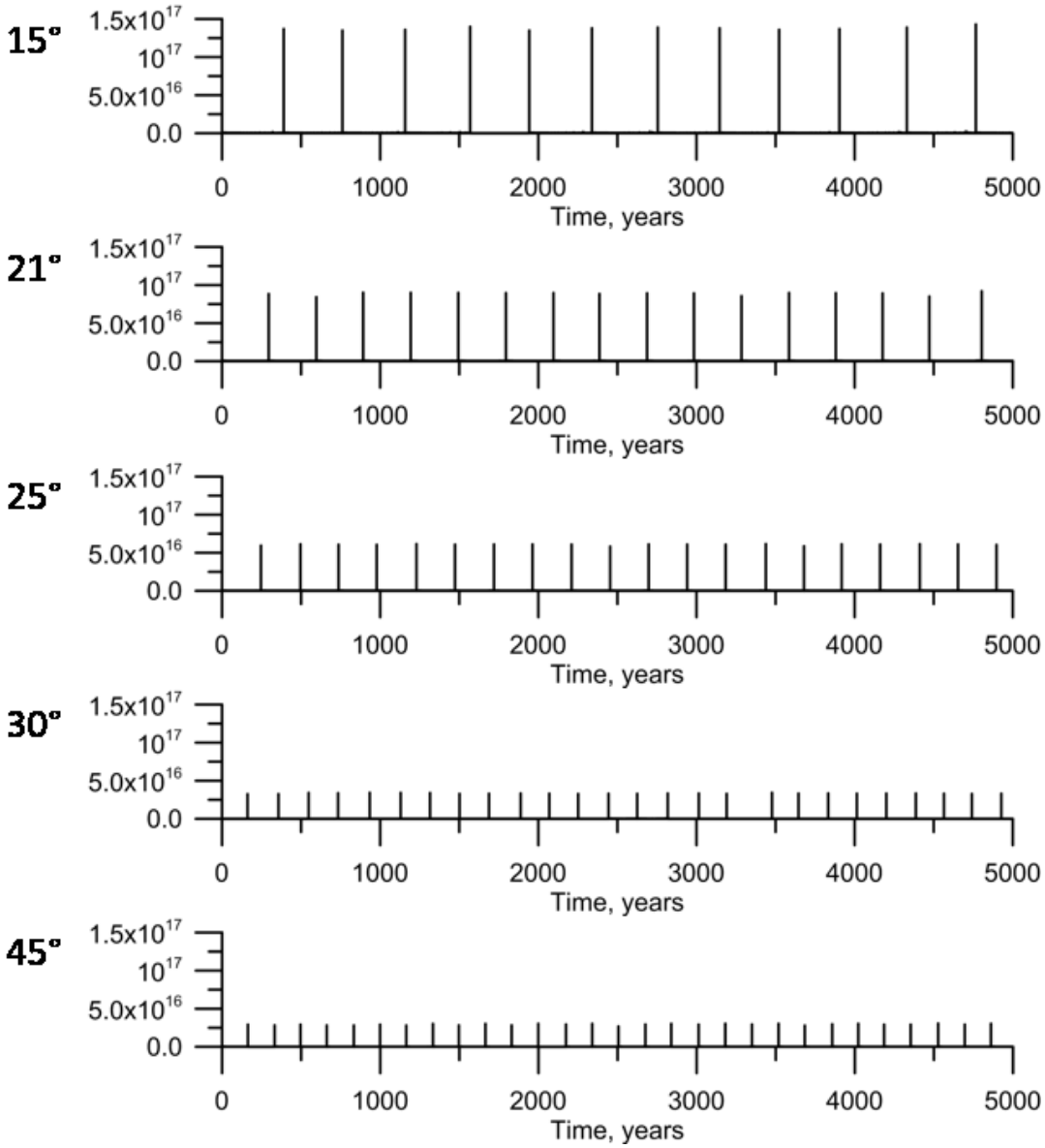

Figure 4.7 Sequence of the earthquakes (2D seismic moments) generated by the models with dipping angles 15°, 21°, 25°, 30°, and 45°.

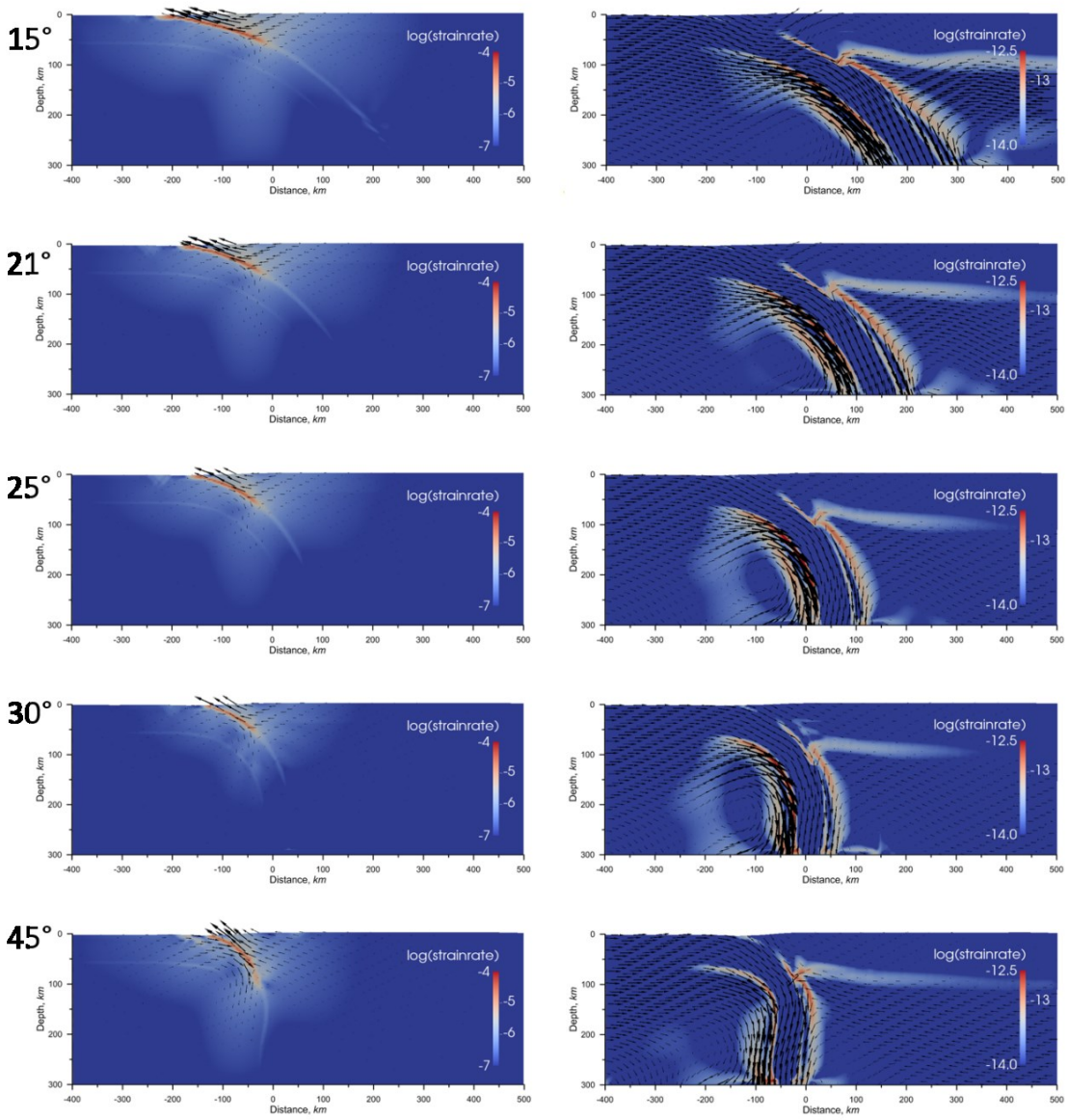

Figure 4.8 Spatial distribution of strain rate (background colors) and velocities (vectors) during earthquake (left column) and during interseismic locking in the models of subduction with dipping angles 15°, 21°, 25°, 30°, and 45°.

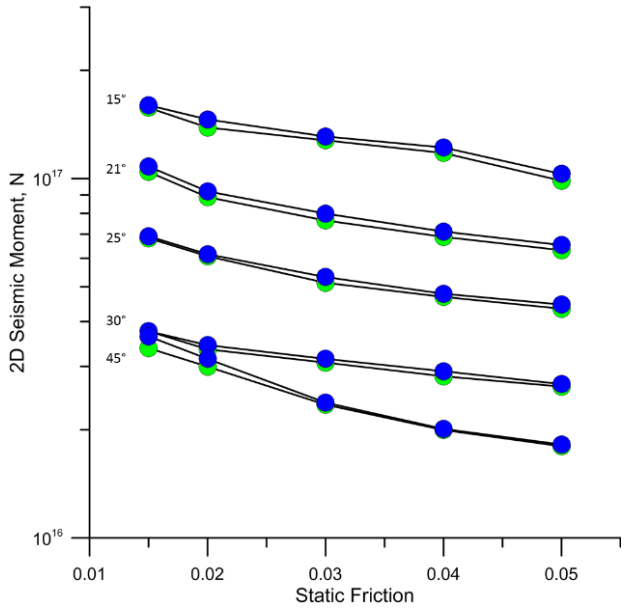

Figure 4.9 Maximum (blue circles) and average (green circles) seismic moments for the cycles versus static friction in the subduction channel in the models with dipping angles 15°, 21°, 25°, 30°, and 45°.

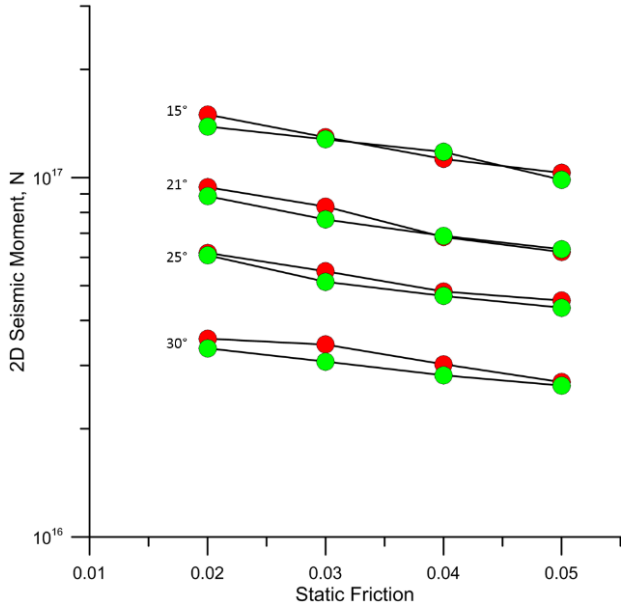

Figure 4.10 Average seismic moments for models with depth unlimited rate weakening (green circles) and with rate strengthening (red circles) deeper than depth of isotherm of 350°C versus static friction in the subduction channel in the models with dipping angles 15°, 21°, 25°, 30°, and 45°.

In another set of models we study effect of subduction velocity on the earthquake seismic moments. Figure 4.11 shows maximum 2D seismic moments for the models of seismic cycles in subduction zones with the same geometry (reference geometry for South Andes) but different static friction coefficients and subduction velocities. The seismic moments are larger for the subduction zones with higher velocities, but for the typical velocities between 3.5 and 10 cm/yr this effect is significantly smaller than effect of static friction. Therefore our modeling suggests that in the hierarchy of effects on seismic moment, the most important is slab geometry, second important is static friction and least important is slab velocity.

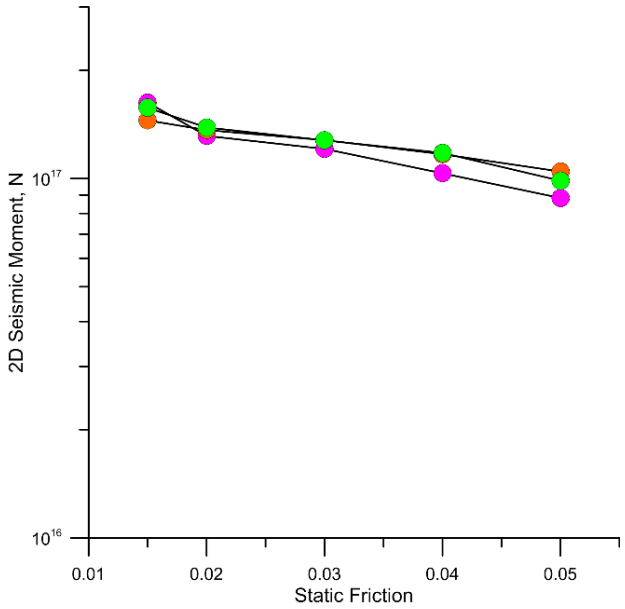

Figure 4.11 Average seismic moments for reference model with different subduction velocities (magenta circles denote 3.5 cm/yr, green 7 cm/yr, orange 10 cm/yr) versus static friction in the subduction channel.

4.4 Models versus Observations

Before we compare our modeling results with observations we must extrapolate out 2D model to 3D. To do so we use empirical scaling low for the rupture length and moment Magnitude, Mw (Strasser et al., 2010):

$$\log_{10} L = -2.477 + 0.585 \times M_W \qquad 4.1$$

Taking into account that $M_W = \frac{2}{3}(\log_{10} M_S(3D) - 9.1)$ and $M_S(2D) = L \times M_S(2D)$ we obtain the following relation between moment magnitude and two-dimentional seismic moment:

$$M_W = 1.09 \times \log_{10}(M_S(2D)) - 9.37 \qquad 4.2$$

The effects of the slab's dipping angles and static friction in subduction channel on maximum moment magnitudes are summarized in Figure 4.12. For each particular slab geometry the largest magnitudes are expected for the lowest friction coefficient. These magnitudes we consider as predicted maximum magnitudes of the subduction earthquakes and compare them with all observed events in Figure 4.13. If our predictions are correct than observed events at subduction zones of all dipping angles must have magnitudes lower or equal to our predicted values. As we see from Figure 4.13 that is indeed the case. One possible exclusion is seismological estimate of Mw=9.5 for the Chile 1960 event, that is higher then geodetic estimate for this event (Mw=9.3-9.4), which we used for the calibration of our models. From that we conclude that our model predictions for the maximum magnitudes are reasonably compatible with the observations.

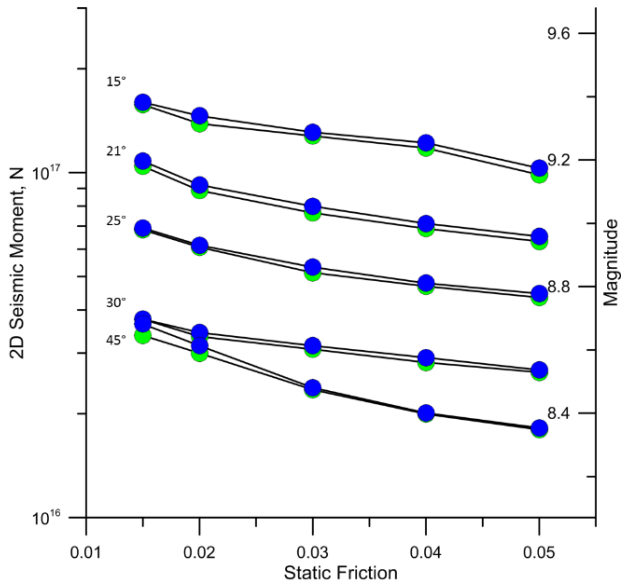

Figure 4.12 Maximum (blue circles) and average (green circles) seismic moments and scaled magnitudes (right axis) for the cycles versus static friction in the subduction channel in the models with dipping angles 15°, 21°, 25°, 30°, and 45°.

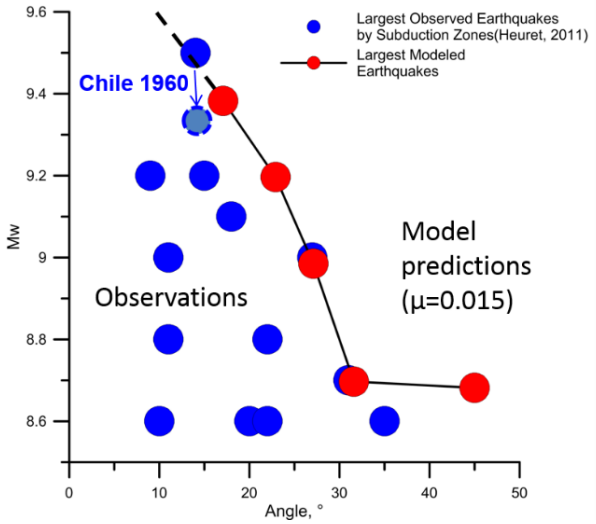

Figure 4.13 Magnitudes of predicted (red circles) and observed (blue circles) the largest earthquakes versus dipping angle of subduction.

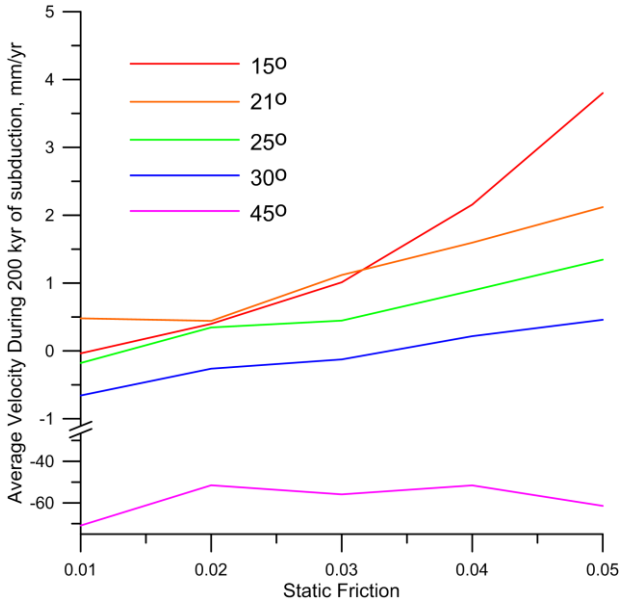

Figure 4.14 Average velocity during 200 kyr of subduction (positive value of velocity denotes compressive regime, negative denotes extensive) versus static friction in the models with dipping angles 15°, 21°, 25°, 30°, and 45°.

Our models also predict that magnitudes of the events should be lower for the subduction zones with higher friction coefficients. This prediction is consistent with the conclusions by Gao and Wang (2014) who estimated friction coefficients in subduction zones using geothermal observations.

In our cross-scale models we can also study the long-tern deformation regimes of the overriding plates for the subduction zone of different geometries and friction coefficients. Figure 4.14 shows mean shortening (positive) or extension (negative) rates of the upper plates during 200 kyr of subduction for the slabs of different dipping angle and different friction coefficients. Modeling suggests that pronounced extension of the upper plate (with more than 2 mm/yr) should be observed only for very steeply dipping slabs and otherwise strain regime should be either neutral (-2 mm/yr <V<2 mm/yr) or compressive (V>2mm/yr). The reason of the close to neutral stress in the upper plates in most of our models is low friction in subduction channel that results in low mechanical coupling between the subducted and overlying plates. Predictions of our models are consistent with the observations (Heuret et al., 2011,2012) that GEQs are observed only in subduction zones with either neutral stain in the upper plate (most frequent) or compressional (less frequent) and never in the case of extensional upper plate. Indeed, according to our models the pronounced extension is expected only for the steeply dipping slabs (Figure 4.14), but all of them are lacking sediments in the trench (see Figure 4.2) which likely prohibit large ruptures due to strong heterogeneity of the topography of the subducting plates (Wang and Bilek, 2014).

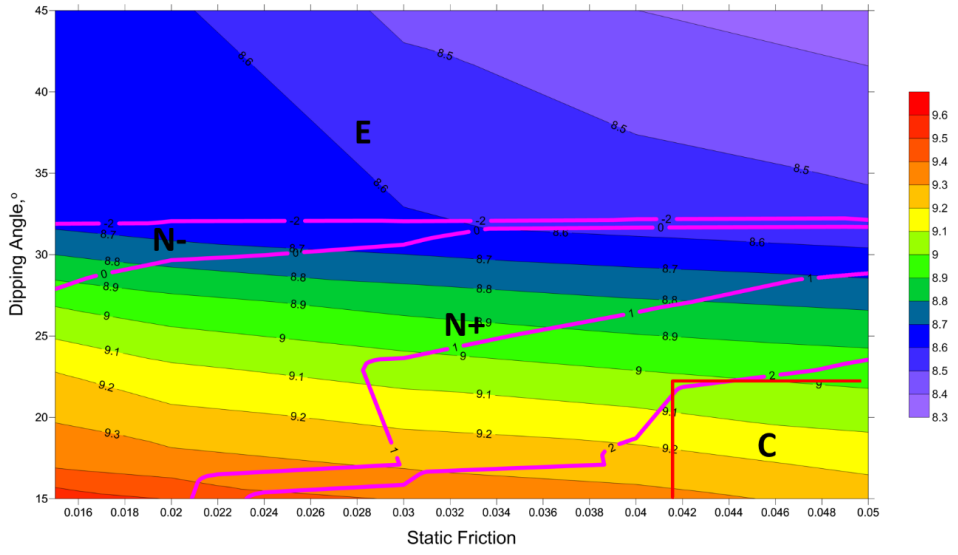

Figure 4.15 Predicted maximum magnitudes of earthquakes (background color) as the function of slab's dipping angle and static friction in the subduction channel. Magenta lines denote isolines of predicted strain regime. Red corner denotes area of compressive strain regime.

We summarize our modeling results in Figure 4.15 were we show predicted maximum magnitudes of the events versus slab's dipping angles and friction coefficients together with the strain regimes in the overriding plates. Interestingly, pronounced compressional regimes in the overriding plates are predicted only in low dip-angle—high friction corner of the diagram (Figure 4.15). This prediction corresponds to the observations (Heuret et al., 2011, 2012) displayed in Figure 4.16.

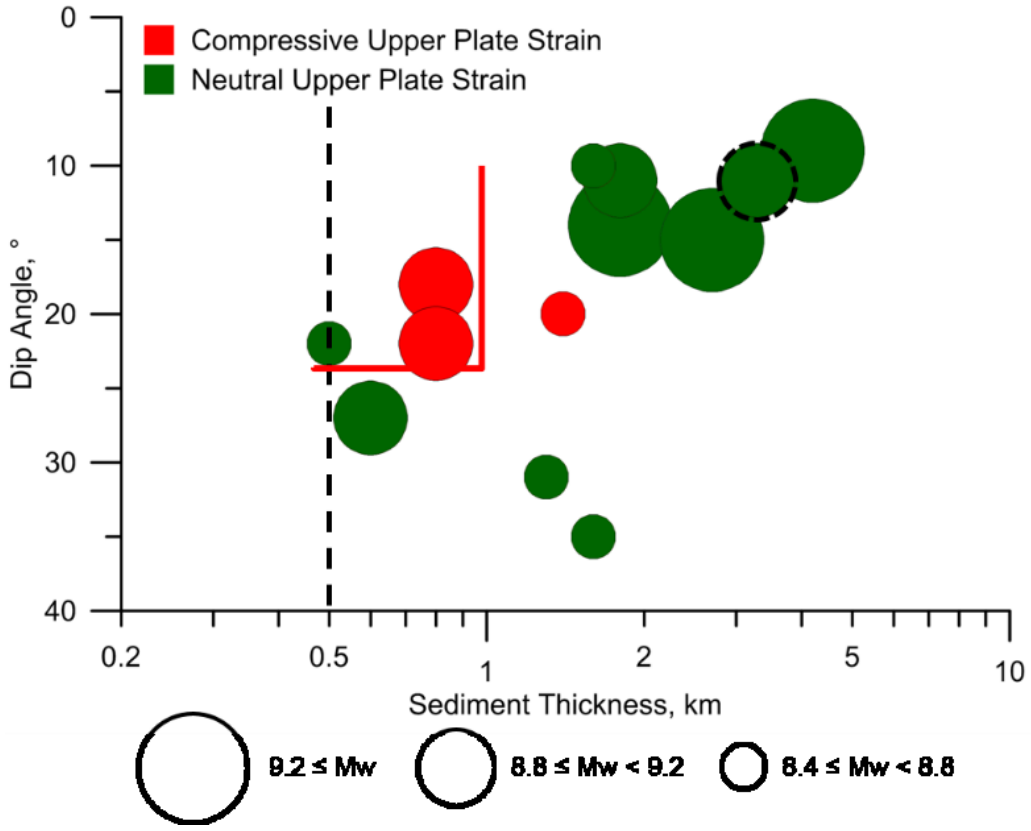

Figure 4.16 Relation between the subduction dipping angle, sediment thickness, M_{max}, and UPS regime for the largest observed earthquakes in every subduction segment. Preinstrumental event is represented by dashed circles. Red corner frames compressive strain regime.

4.5 Interpretation of Modeling Results

Modeling results presented in the previous sections and their comparison with observations already answer questions 1 to 4 stated in section 4.2. Here we show that all these results allow very simple interpretation. In Figure 4.17 we plot maximum magnitudes for all models versus modeled rupture width. The figure shows that all considered parameters, i.e. slab's dipping angles, friction coefficients and slab velocities in fact affect maximum magnitudes of events through only one parameter, which is rupture width.

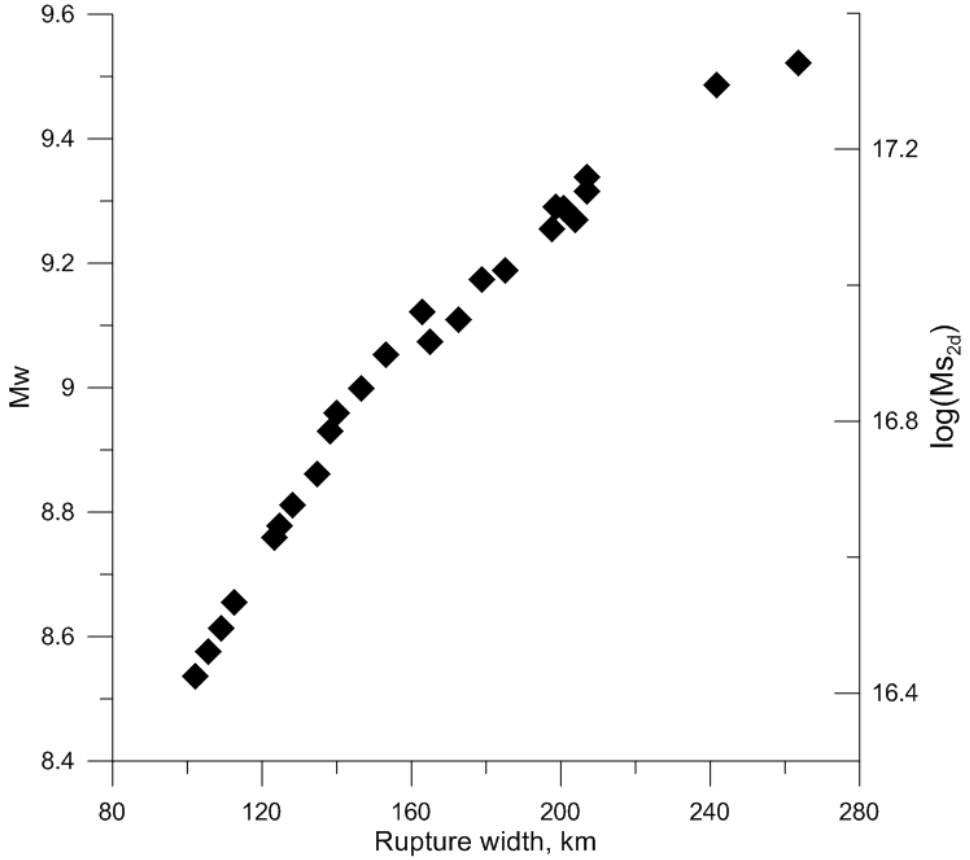

Figure 4.17 Maximum magnitudes and 2D seismic moments (right axis) for the cycles versus corresponding rupture width in the models with dipping angles 15°, 21°, 25°, 30°, and 45°.

Effect of the slab geometry on rupture width is obvious. Friction coefficient in the channel and subduction velocity affect rupture width by changing depth of brittle-ductile transition (Figure 4.18 and Figure 4.19). Interestingly influence of normal stress variations (that are different for different slab geometries) on maximum magnitudes of events appears to

be much less significant than effect of rupture width. This conclusion fully supports concept by Keheller et al. (1974) with addition of concept by Ruff (1989) that what actually is important for the high magnitude of events is large and coherent contact zone between the slab and overriding plate that could be ruptured in the single event.

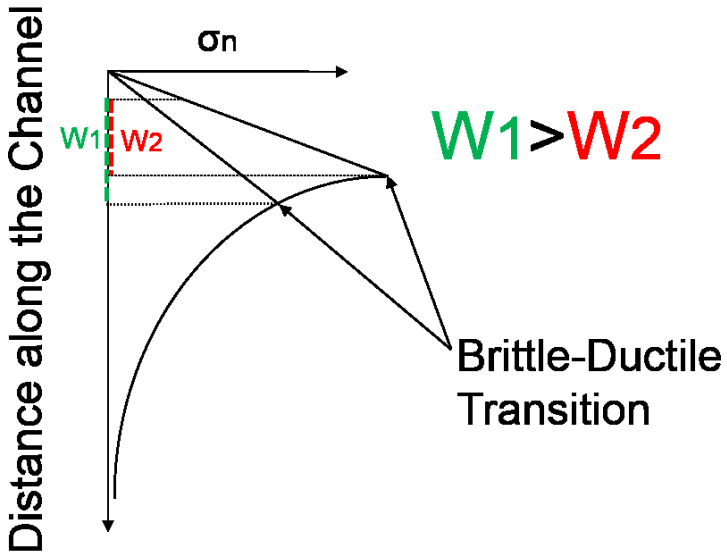

Figure 4.18 Effect of static friction in the subduction channel on seismogenic width. Lower friction results in deeper brittle-ductile transition zone.

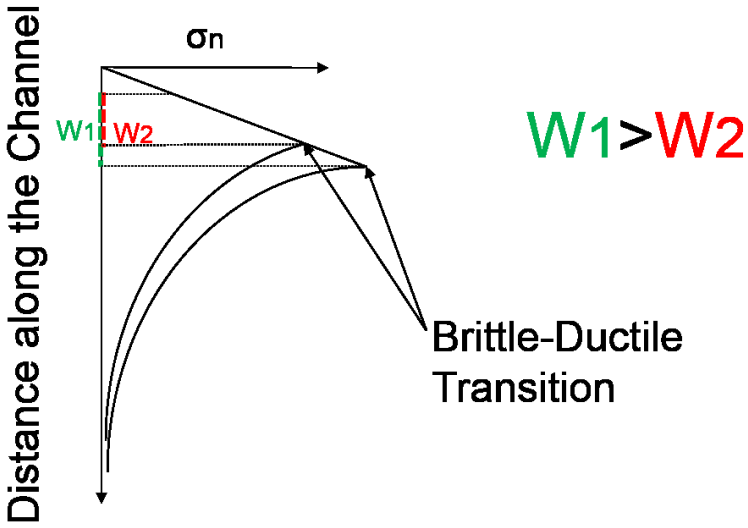

Figure 4.19 Effect of subduction velocity on seismogenic width. Faster subduction results in colder temperature in the subduction channel.

However, the concept by Ruff and Kanamori (1980), based on the idea that the event magnitude is controlled by the strength of the mechanical coupling between the plates, is not confirmed by our models. Figure 4.20 shows that magnitudes of modeled events are only marginally dependent on the magnitude of the average shear stress at the subduction interface, and the observed weak dependence is opposite to the expectations, i.e. higher moment magnitudes correspond to the lower shear stresses. This confirms again that not a shear stress at the contact zone, but its area and coherence (no barriers) is likely controlling maximum magnitude of the event.

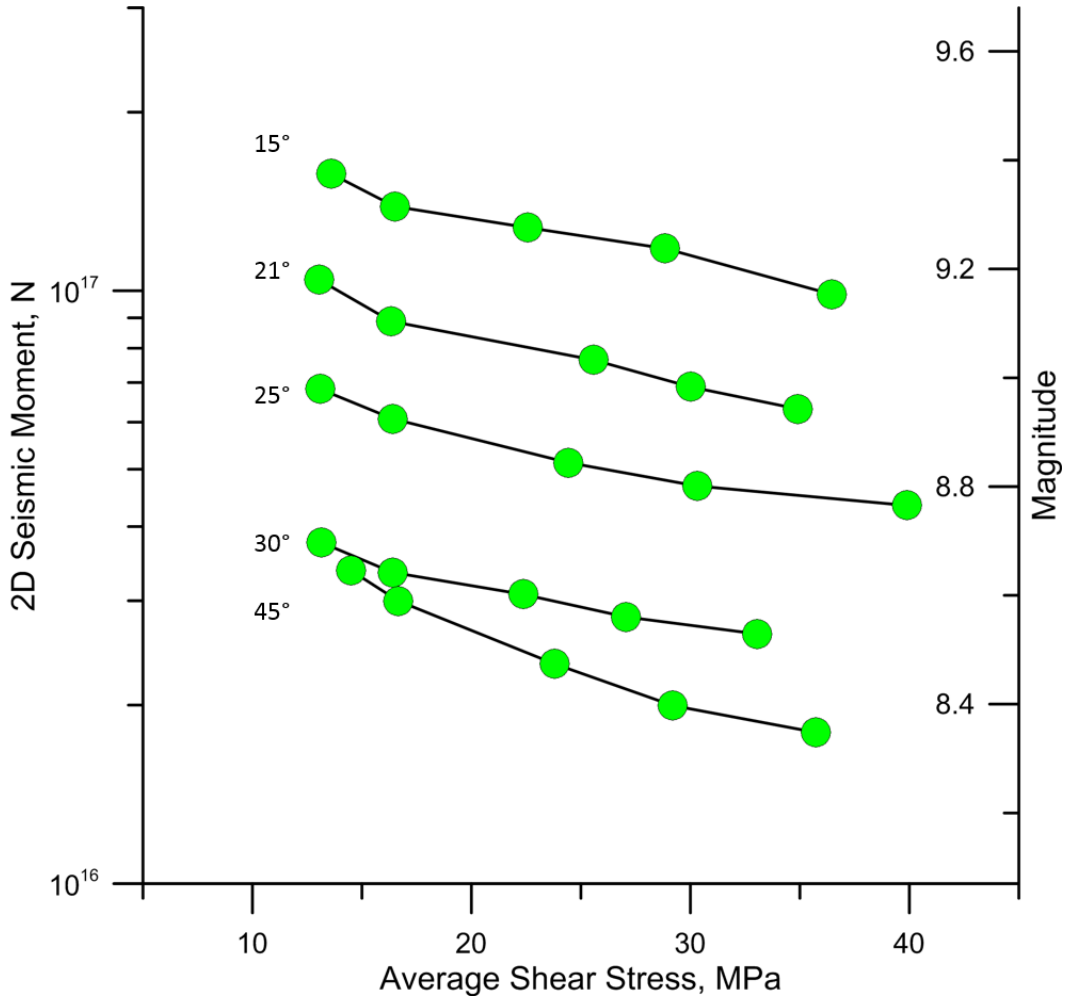

Figure 4.20 Average seismic moments and scaled magnitudes (right axis) for the cycles versus corresponding average shear stress in the subduction channel in the models with dipping angles 15°, 21°, 25°, 30°, and 45°.

4.6 Model Limitations

Most important limitation of our model is its two-dimensionality. We extrapolate our modeling results to 3D case using statistical scaling low, which actually implies that rupture length scales with the rupture width. However that must not be always a case. If there were an impermeable barrier for the rupture propagation at a distance to the hypocenter closer than rupture width, or large curvature of subduction zone segment (Schellart and Rawlingson, 2014) than this scaling would fail. In this case event magnitude will be smaller than predicted by our 2D model scaled to 3D. In the opposite case when the barrier were at a distance much larger than rupture width, the scaling would also fail and event magnitude would be larger than predicted.

4.7 Conclusions

We developed 2D models of seismic cycles for the subduction zone earthquakes with different geometries of subducting plates, different static friction coefficients in subduction channels and different subduction velocities.

Under the assumption that rupture length scales with the rupture width, our models demonstrate that maximum magnitudes of the earthquakes are exclusively controlled by the factors that increase rupture width. These factors are: low slab's dipping angle (the largest effect), low friction coefficient in subduction channel (smaller effect) and high subduction velocity (the smallest effect).

Models suggest that neither changes of normal stress in subduction zones nor shear stresses at subduction interface play an important role in controlling maximum magnitude of the earthquakes.

In agreement with observations, our models suggest that the largest earthquakes should occur in subduction zones with neutral (most frequently) or moderately compressive deformation regimes of the upper plate. This is a consequence of the low dipping angles and low static friction coefficients in the subduction zones with largest earthquakes, rather than a reason for the largest earthquakes.

The predicted maximum magnitudes for the subduction zones of different geometries are consistent with the observed magnitudes for all events.

Chapter 5 3D Subduction Model

The clear limitation of most of the models developed in the thesis is their 2D nature. Development of 3D models with comparable resolution and complexity will require significant advance in numerical techniques. While that is still in progress, we conducted a series of low-resolution 3D models to study interaction between two large asperities at subduction interface separated by aseismic gap with different width.

5.1 Setting up 3D Model

In this chapter we present results of modeling earthquakes in 3D subduction model. We use similar geometry and temperature distribution as in our reference 2D model close to southern Chile. Incorporation of the third dimension requires, of course, much more finite elements to discretize the model which, in turn, slows down calculations. We had to decrease spatial resolution to the size of seven kilometers in the plane of subduction profile. Assuming that size of great earthquake's asperities in subduction zone is measured by tens or hundreds of kilometers, we set the size of elements along the trench to 50 kilometers. The whole model box has dimension of 900 km across the trench and 300 km vertical and uniform slab geometry (Figure 5.1). The width of the model along the trench is varied from 500 km to 900 km allowing different widths of the aseismic gap (see below).

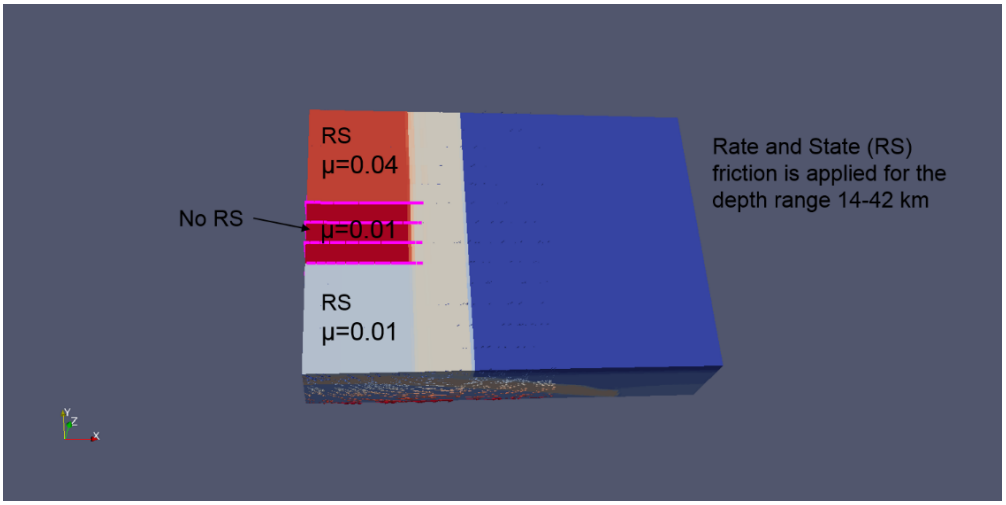

Figure 5.1 3D setup of the model with two asperities separated by a neutral gap. Southern (light blue) and northern (orange) patches obey rate-and-state friction law with different static frictions. Neutral patch in between (red) has static friction law only.

We generate subduction by advancing oceanic lithosphere in the direction of continental lithosphere with the 30° dipping low-strength fault between them: as it is usually done in long-term 2D subduction models. The bottom boundary is flow-open and left boundary is kinematicaly prescribed. Horizontal velocities at the upper 55 km of the left boundary were fixed at 7 cm/yr. Velocities at the left boundary deeper than 55 km are chosen by trial and error to achieve geometry of the subducted slab consistent with the geometry of the southern Chile.

We take the 3D geological time-scale model as an initial setup for the modeling of the seismic cycles of great earthquakes. Then we carry out the same procedures (2.1.2) as in our 2D reference model to use time steps of 10 years.

In order to decrease calculation time, we do not implement adaptive time stepping but, instead, use uniform time step of 10 years. In this case displacements in every element of the seismogenic zone become much larger than the critical displacement of rate-and-state friction law (equation 1.28), and solution of this constitution equation will be the same as in the steady state formulation. Therefore, we introduce steady state formulation (equation 1.30) to our seismogenic zone, which speeds up our model. Since earthquakes in this model occur within 10 years time step we obtain much smaller drop of viscosity which eliminates necessity of the transient rheology.

After all procedures discussed above model generates sequences of earthquakes. We consider 2 patches with rate-and-state rheology. Southern (light blue) patch has static friction $\mu_0 = 0.01$ and *(b-a)*=0.002. Northern (orange) patch has static friction $\mu_0 = 0.04$ and *(b-a)*=0.002. There is a neutral (no rate-and-state rheology) patch with static friction $\mu_0 = 0.01$. Whole oceanic plate is loaded with uniform velocity of 7 cm/yr.

5.2 Interaction between Asperities

Different static frictions control different depths for the brittle-ductile transition zone resulting in slightly different characteristic recurrence times of the two asperities. We would like to investigate if the two asperities could trigger earthquakes on each other. To be sure that earthquakes at one asperity indeed trigger earthquakes at another asperity, we adapt our model to initiate earthquake sequencies at different asperities in different moments. Thereby, first seismic cycles of asperities occur in antiphase.

It is logical to suppose that degree of interaction between the two seismogenic asperities depends on the width of the aseismic gap in-between. We vary width of the gap to study effectiveness of mutual triggering. As it could be expected, aseismic gap with a small width could not prevent rupture from propagating from one asperity to another resulting in whole model rupturing. When gap becomes too wide, asperities do not interact any more), and some rare whole model earthquakes can be explained by coincidence.

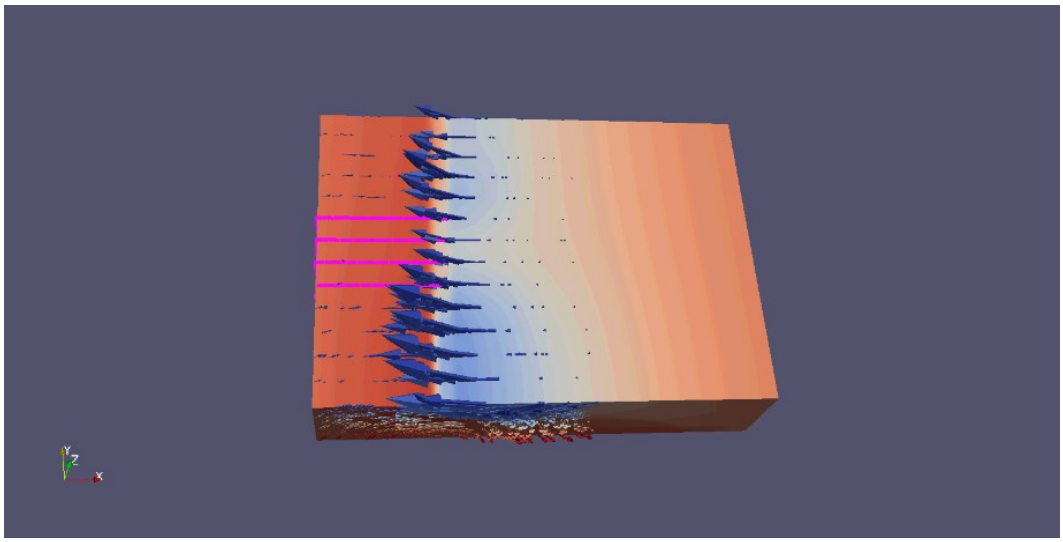

Figure 5.2 Rupture propagated through the whole subduction model, i.e., breaking the two asperities at once. Arrows and background color correspond to velocity, aseismic gap is represented with pink dots.

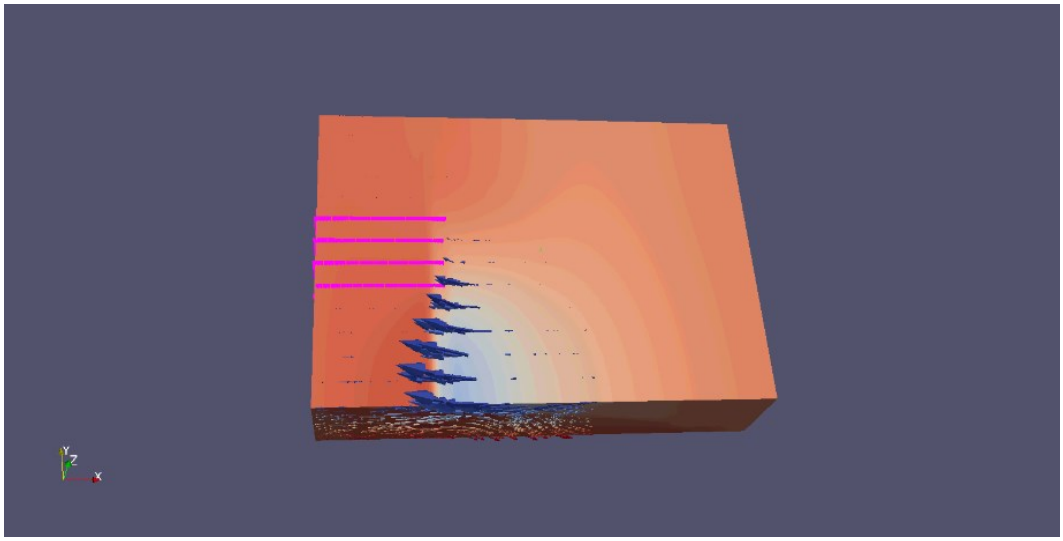

Figure 5.3 Rupturing of the southern asperity only. Arrows and background color correspond to velocity, aseismic gap is represented with pink dots.

The most interesting interaction was observed in the model with moderate width of the aseismic gap of 150 km. In this case first asperities ruptured mostly together Figure 5.2, but finally the steady-state regime was achieved, when asperities were ruptured separately, Figure

5.3. Figure 5.4 illustrates time sequence of earthquakes at different asperities. Red and blue peaks correspond to northern and southern asperity, respectively.

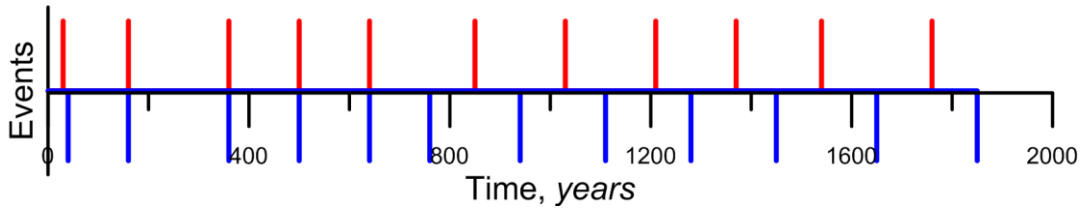

Figure 5.4 Sequence of earthquake on the two asperities. Red peaks correspond to northern asperity, blue - to southern asperity.

The very first earthquakes at northern and southern asperities were generated at different time moments, then, the next 4 earthquakes at both asperities occurred simultaneously. However, after about 700 years earthquakes occurred only in antiphase. Every earthquake occurred in the middle of interseismic period of the opposite asperity.

5.3 Interpretation and Conclusions

Our model suggests presence of a "transition" width of an aseismic gap between asperities which provokes earthquakes to occur in antiphase. This regime can be described as the least-interaction regime, when the mechanical interaction between the adjacent asperities is minimized.

If gap between asperities is smaller than the "transition" width, earthquakes on each asperiety will trigger each other. If gap-width is larger, asperities will break independently. Although interestiong, it is clear that these results must be confirmed with the higher resolution models which we plan in the future.

Interraction between neighboring asperities is an interesting problem that was previously addressed by numerical model (Kaneko et al., 2010), but to our knowlange no models have simulated interraction of asperities over the multple seismic cycles, like it happens in nature. An example of this process is the history of earthquakes along the Chilean subduction zone (Figure 5.5). This subduction zone is characterized by a long and relatively straight trench which is optimal for appearance of giant earthquakes. Several giant earthquakes over the last 500 years covered the whole range, showing complicated patters of "clustering" and anti-phase rupturing (Figure 5.5) . It is clear that for modeling of this behavour we must extend our 3D models by including several asperities and to model their interraction during longer time.

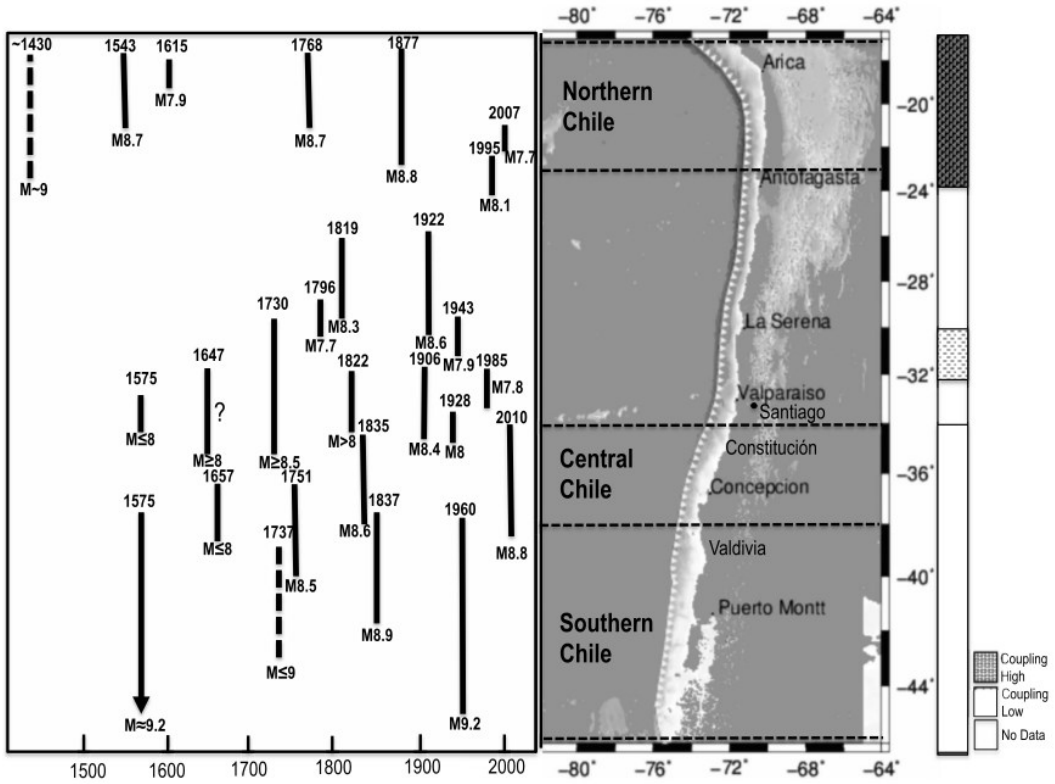

Figure 5.5. The earthquake history and coupling of Chile. From Scholz and Campos, 2012.

Chapter 6 Summary and Outlook

In the thesis a cross-scale thermomechanical model simulating the entire subduction process from earthquake (1 minute) to million years time scale was developed. The model employs elasticity, non-linear transient viscous rheology and rate-and-state friction. It generates spontaneous earthquake sequences and by using adaptive time-step algorithm, recreates the deformation process as observed naturally during seismic cycle and multiple seismic cycles.

For our reference model we designed a setup replicating of geometry, lithospheres age and temperature distribution of the southern Chile. Calibrating rate-and-state parameters we obtained model with a spontaneous instabilities are generated leading to the stick-slip deformation process with the average recurrence times of earthquakes of 350-430 years and average 2D seismic moments of $1.5\text{-}1.8*10^{17}$N, and average static stress drops of 4-6 MPa. Recurrence time, moment magnitudes (Mw=9.3-9.35 assuming rupture length of 800 km) and stress drop are in agreement with the geodesy-based estimates for the Chile 1960 event.

The model passed verification tests by comparison with the known high-resolution solutions for the generic modeling setups widely used in modeling of rupture propagation. It is demonstrated, that while not modeling rupture propagation explicitly, the modeling procedure correctly recognizes appearance of instability (earthquake) and correctly simulates cumulative slip at a fault during an earthquake in quasi-dynamic approximation.

A developed technique was used for three different studies: postseismic relaxation after great earthquakes, estimation of the maximum magnitudes of the earthquakes in subduction zones and modeling interaction of two adjacent asperities in 3D model.

1. The set of 2D models is used to study effects of non-linear transient rheology on postseismic processes after great earthquakes. Models predict that viscosity in the mantle wedge drops by 3 to 4 orders of magnitude during the great earthquake with magnitude above 9 due to the power-law creep rheology (major factor) and transient dislocation creep based on experimental data and theoretical mineral physics considerations. This results in significantly different spatial scale and timing of the relaxation processes following the earthquake than it is currently believed. Our model produce large postseismic creep due to visco-elastic relaxation in the mantle wedge that shows up in surface deformation similar to the classical afterslip and therefore can be misinterpreted as an afterslip. Our model fits well the GPS data for postseismic slip of Tohoku 2011 earthquake in the time range of 1 day-1 year.
2. The 2D models are also applied to study key factors controlling maximum magnitudes of earthquakes in subduction zones. Under the assumption that rupture length scales with the rupture width, our models demonstrate that

maximum magnitudes of the earthquakes are exclusively controlled by the factors that increase rupture width. These factors are: low slab's dipping angle (the largest effect), low friction coefficient in subduction channel (smaller effect) and high subduction velocity (the smallest effect). Models suggest that neither changes of normal stress in subduction zones nor shear stresses at subduction interface play an important role in controlling maximum magnitude of the earthquakes. In agreement with observations, our models also suggest that the largest earthquakes should occur in subduction zones with neutral (most frequently) or moderately compressive deformation regimes of the upper plate. This is a consequence of the low dipping angles and low static friction coefficients in the subduction zones with largest earthquakes, rather than a reason for the largest earthquakes. The predicted maximum magnitudes for the subduction zones of different geometries are consistent with the observed magnitudes for all events.

3. We conducted a series of low-resolution 3D models to study interaction between two large asperities at subduction interface separated by aseismic gap with different width. Our model suggests presence of a "transition" width of about 150 km and of an aseismic (b-a)=0 gap between asperities which provokes earthquakes to occur in antiphase. If gap between asperities is smaller than this "transition" width, earthquakes on both asperieties occure mostly simultaniously. If gap-width is larger, asperities rupture independently. These modeling results are suggestive, but due to the low resolution of the model can be considered only as a preliminary, which require confirmation with high-resolution models.

The developed technique of cross-scale modeling of seismic cycles is ready to study the still poorly understood effects of the multiple seismic cycles on the long-term deformation of the upper plate. The technique can be also extended to the case of continental transform faults and for the advanced 3D modeling of specific subduction zones.

The clear limitation of most of the models developed in the thesis is their relatively low spatial and temporal resolution caused by long computing time in SLIM3D. Thus, in future the technique of cross-scale earthquake cycle modeling should be implemented using highly scalable parallel codes like LAMEM (Kaus et al., 2016) and ASPECT (https://aspect.dealii.org/).

Bibliography

ASPECT: Advanced Solver for Problems in Earth's ConvecTion, https://aspect.dealii.org/

Audet, P., Bostock, M. G., Christensen, N. I. & Peacock, S. M. Seismic evidence for overpressured subducting oceanic crust and megathrust fault sealing. *Nature* **457**, 76–78 (2009).

Bai, Q., Mackwell, S.J. and Kohlstedt, D.L. High-temperature creep of olivine single cyrstals 1. Mechanical results for buffered samples. *J. Geophys. Res*. **96**, doi: 10.1029/90JB01723 (1991)

Beeler, N.M., Tullis, T.E., & Weeks, J.D., The roles of time and displacement in the evolution effect in rock friction, *Geophys. Res. Lett.*, **21**, 1987-1990, (1994).

Belytschko, T., W. Liu, B. Moran, & K. Elkhodary, Nonlinear Finite Elements for Continua and Structures, Wiley Desktop Editions, Wiley (2013).

Brace W. F. & Byerlee J. D. Stick-Slip as a Mechanism for Earthquakes. Science, New Series, Vol. 153, **3739**, 990-992. (1966).

Bürgmann, R. & Dresen, G. Rheology of the lower crust and upper mantle: evidence from rock mechanics, geodesy and field observations. *Annu. Rev. Earth Planet. Sci.* **36**, 531–567 (2008).

Cisternas, M. Predecessors of the giant 1960 Chile earthquake, *Nature* **437**, 404-407 (2005).

Cochard, A., and R. Madariaga, Compexity of seismicity due to highly rate dependent friction, *J. Geophys. Res*., **101**, 25,321-25,336, (1996).

Cubas, N. et al., Numerical modeling of long-term earthquake sequences on the NE Japan megathrust: Comparison with observations and implications for fault friction. *Earth Planet. Sci. Lett.* **419**, 187–198 (2015).

Currie, C. A. & Hyndman, R. D. The thermal structure of subduction zone back arcs. *J. Geophys. Res.* **111**, B08404, doi:10.1029/2005JB004024 (2006).

den Hartog, S.A.M., Niemeijer, A.R., Spiers, C.J. New constraints on megathrust slip stability under subduction zone *P – T* conditions. *Earth Planet Sci Lett*, **353–354**. doi:10.1016/j.epsl.2012.08.022. 240–252 (2012).

Dieterich, J.H. PAGEOPH (1978) 116: 790. doi:10.1007/BF00876539.

Dietrich, J. H., Time-dependent friction in rocks, *J. Geophys. Res.* **77(20)**,3690-3697, doi:10.1029/JB0077i020p03690 (1972).

Dzierma, Y. et al. Seismicity near the slip maximum of the 1960 Mw 9.5 Valdivia earthquake (Chile): Plate interface lock and reactivation of the subducted Valdivia Fracture Zone. *J. Geophys. Res.* **117**, B06312, doi:10.1029/2011JB008914 (2012).

Evgene B. Burov, Rheology and strength of the lithosphere, Marine and Petroleum Geology, **28(8)**, 1402-1443, http://dx.doi.org/10.1016/j.marpetgeo.2011.05.008 (2011).

Farla, R. J. M., Jackson, I., Gerald, J. D. F., Faul, U.H. & Zimmerman, M. E. Dislocation Damping and Anisotropic Seismic Wave Attenuation in Earth's Upper Mantle, *Science* **336**, 332-335 (2012).

Freed AM, & Bürgmann R. Evidence of power-law flow in the Mojave desert mantle. *Nature* **430**, 548–551 (2004).

Freed, A. M. Earthquake triggering by static, dynamic, and postseismic stress transfer. *Annu. Rev. Earth Planet. Sci.* **33**, 335–367 (2005)

Freed, A. M., & Bürgmann, R., Calais, E. & Freymueller, J. T. Stress-dependent power- law flow in the upper mantle following the 2002 Denali, Alaska, earthquake. *Earth Planet. Sci. Lett.* **252**, 481–489 (2006).

Freed, A. M., Bürgmann, R. & Herring, T. A. Far-reaching transient motions after Mojave earthquakes require broad mantle flow beneath a strong crust. *Geophys. Res. Lett.* **34**, L19302, doi:10.1029/2007GL030959 (2007).

Freed, A. M., Herring,T and Bürgmann R. Steady state laboratory flow laws alone fail to explain postseismic observations, *Earth Planet. Sci. Lett*., **300**, 1–10, doi:10.1016/j.epsl.2010.10.005 (2010).

Freed, A. M., Hirth, G. & Behn, M. D. Using short-term postseismic displacements to infer the ambient deformation conditions for the upper mantle. *J. Geophys. Res.* **117**, B01409, doi:10.1029/2011JB008562 (2012).

Gao, X. & Wang, K. Strength of stick-slip and creeping subduction megathrusts from heat flow observations *Science*, **345**, 1038–1041 (2014).

Gerya, T. V., and D. A. Yuen, Robust characteristics method for modelling multiphase visco-elasto-plastic thermo-mechanical problems, *Physics of the Earth and Planetary Interiors*, **163(1–4)**, 83–105, doi:10.1016/j.pepi.2007.04.015 (2007).

Gorczyk, W., et al., Asthenospheric upwelling, oceanic slab retreat, and exhumation of UHP mantle rocks: Insights from Greater Antilles, *Geophys. Res. Lett.*, **34**, L21309, doi:10.1029/2007GL031059 (2007).

Heuret, A. et al. Relation between subduction megathrust earthquakes, trench sediment thickness and upper plate strain. *Geophys. Res. Lett*. **39**, (2012).

Heuret, A., Lallemand, S., Funiciello, F., Piromallo, C. & Faccenna, C. Physical characteristics of subduction interface type seismogenic zones revisited. *Geochemistry Geophysics Geosystems (G3)* **12**, (2011).

Hirth, G. & Kohlstedt, D. L. Rheology of the upper mantle and the mantle wedge: A view from the experimentalists, *Inside the Subduction Factory* (ed. Eiler, J.). 83–105 (2003).

Hoechner, A., Sobolev, S. V., Einarsson, I. & Wang,R. Investigation on afterslip and steady state and transient rheology based on postseismic deformation and geoid change caused by the Sumatra 2004 earthquake. *Geochemistry*

Geophysics Geosystems (G3) **12**. Q07010, doi:10.1029/2010GC003450. (2011).
Hoffmann-Rothe, A. et al. Oblique Convergence along the Chilean Margin: Partitioning, Margin-Parallel Faulting and Force Interaction at the Plate Interface. *In* Oncken O. et al. The Andes, Active Subduction Orogeny. 125-146. Springer (2006).
Hu, Y. et al. Stess-driven relaxation of heterogeneous upper mantle and time-dependent afterslip following the 2011 Tohoku earthquake. *J. Geophys. Res.* **121**, 385–411, doi:10.1002/2015JB012508 (2016).
Hughes, T., The Finite Element Method: Linear Static and Dynamic Finite Element Analysis, Dover Civil and Mechanical Engineering, Dover Publications (2012).
Irwin,W. P. & Barnes, I. Effects of geological structure and metamorphic fluids on seismic behavior of the San Andreas fault system in central and northern California. *Geology* **3**, 713–716 (1975).
Kameyama, M., D. A. Yuen, & S.-I. Karato, Thermal-mechanical effects of low-temperature plasticity (the Peierls mechanism) on the deformation of a viscoelastic shear zone, *Earth and Planetary Science Letters*, **168(1–2)**, 159–172, doi:10.1016/S0012-821X(99)00040-0 (1999).
Kanamori H. & Brodsky E. E., The physics of earthquakes. *Rep. Prog. Phys*. **67**, 1429–1496, doi:10.1088/0034-4885/67/8/R03 (2004).
Kaneko, Y., Avouac, J. P. & Lapusta, N. Towards inferring earthquake patterns from geodetic observations of interseismic coupling. *Nature Geosci*. **3**, 363–369 (2010).
Karato S. *Deformation of Earth Materials: Introduction to the Rheology of the Solid Earth*. 462 (Cambridge Univ. Press., 2008).
Karato, S.I. Micro-Physics of Post Glacial Rebound, *GeoResearch Forum* **3-4**, 351-364 (1998).
Kaus, B., Popov, A., Baumann, T., Pusok, A., Bauville, A., Fernandez, N., and Collignon, M. Forward and inverse modeling of lithospheric deformation on geological timescales. *NIC Symposium 2016 - Proceedings*, **48**:1–8. (2016).
Kelleher, J., Savino, J. Rowlett, H. & McCann, W., Why and Where Great Thrust Earthquakes Occur along Island Arcs. *Geophys. Res*., **79**, 4889-4899, (1974).
Khazaradze, G et al, Prolonged post-seismic deformation of the 1960 great Chile earthquake and implications for mantle rheology, *Geophys. Res. Lett*. **29**, 2050, doi:10.1029/2002GL015986 (2002)
Khazaradze, G. & Klotz, J. Short- and long-term effects of GPS measured crustal deformation rates along the south central Andes. *J. Geophys. Res.,* **108**: doi: 10.1029/2002JB001879 (2003).
Lamb, S. & Davis. P., Cenozoic climate change as a possible cause for the rise of the Andes. *Nature,* **425**, 792-797 (2003).

Lamb, S., Shear stresses on megathrusts: Implications for mountain building behind subduction zones, *J. Geophys. Res.,* **111**, B07401, doi:10.1029/2005JB003916 (2006).

Landau, L. D., & E. Lifshitz, Theory of elasticity, vol. 7, Course of Theoretical Physics, 3 (1986).

Lapusta, N. & Barbot, S. Models of earthquakes and aseismic slip based on laboratory-derived rate-and-state friction laws, in The Mechanics of Faulting: From Laboratory to Real Earthquakes, edited by A. Bizzarri and H. S. Bhat, pp. 153–207, Research Signpost, Trivandrum, Kerala, India (2012).

Lapusta, N. et al. Elastodynamic analysis for slow testonic loading with spontaneous rupture episodes on faults with rate- and state-dependent friction. *J. Geophys. Res.* **105**, 23765–23789, doi:10.1029/2000JB900250 (2000).

Linde, A.T, & Silver, P.G. Elevation changes and the great 1960 Chilean earthquake: support for aseismic slip, *Geophys. Res. Lett.* **16**, 1305-1308 (1989).

Liu, Y. & Rice, J. R. Spontaneous and triggered aseismic deformation transients in a subduction fault model. *J. Geophys. Res.* **112**, B09404, doi:10.1029/2007JB004930 (2007).

Liu, Y. & Rice, J. R. Spontaneous and triggered aseismic deformation transients in a subduction fault model. *J. Geophys. Res.* **112**, B09404, doi:10.1029/2007JB004930 (2007).

Marone C., & Kilgore B., Scaling of the critical slip distance for seismic faulting with shear strain in fault zones. *Nature* **362**, 618 – 621, doi:10.1038/362618a0 (1993).

Marone, C. J., Scholz C. H., & Bilham R. On the mechanics of earthquake afterslip, *J. Geophys. Res.* **96**, 8441 – 8452 (1991).

Moreno, M. S., Bolte, J., Klotz, J. & Melnick, D. Impact of megathrust geometry on inversion of coseismic slip from geodetic data: Application to the 1960 Chile earthquake. *Geophys. Res. Lett.* **36**, L16310, doi:10.1029/2009GL039276 (2009).

Noda, H. & Lapusta, N. Stable creeping fault segments can become destructive as a result of dynamic weakening. *Nature* **493**, 518–521 (2013).

Nur, A., & G. Mavko, Postseismic viscoelastic rebound, *Science,* **183(4121)**, 204-206 (1974).

Okubo, P. G., Dynamic rupture modeling with laboratory-derived constitutive relations, *J. Geophys. Res*., **94**, 12,321-12,335, (1989).

Perfettini, H., & J.-P. Avouac. Postseismic relaxation driven by brittle creep: A possible mechanism to reconcile geodetic measurements and the decay rate of aftershocks, application to the Chi-Chi earthquake, Taiwan, *J. Geophys. Res.* **109** B02304, doi:10.1029/2003JB002488 (2004).

Plafker, G., & Savage, J. C. Mechanism of the Chilean earthquakeof May 21 and 22, 1960. *Geological Society of America Bulletin* **4**, 1001-1030 (1970).

Pollitz, F. F. Transient rheology of the uppermost mantle beneath the Mojave Desert, California. *Earth Planet. Sci. Lett.* **215**, 89–104 (2003).

Pollitz, F. F.,Post-seismic relaxation theory on a laterally heterogeneous viscoelastic model. *Geophysical Journal International*, 155: 57–78. doi:10.1046/j.1365-246X.2003.01980.x (2003).

Popov, A. A., Three-dimensional thermo-mechanical modeling of deformation at plate boundaries: case study San Andreas Fault System, Ph.D. thesis, University of Potsdam (2009).

Popov, A.A. & Sobolev, S.V., SLIM3D: A tool for thermomechanical modeling of lithospheric deformation withelasto-visco-plastic rheology. *Phys. Earth. Planet. Inter*. **171**, 55–75 (2008).

Quinteros, J., & S. V. Sobolev, Constraining kinetics of metastable olivine in the Marianas slab from seismic observations and dynamic models, Tectonophysics, 526–529, 48–55, doi:10.1016/j.tecto.2011.11.005 (2012a).

Quinteros, J., & S. V. Sobolev, Why has the Nazca plate slowed since the Neogene? Geology, 41(1), 31–34, doi:10.1130/G33497.1 (2012b).

Quinteros, J., S. V. Sobolev, and A. A. Popov, Viscosity in transition zone and lower mantle: Implications for slab penetration, Geophysical Research Letters, 37(9), 1–5, doi:10.1029/2010GL043140 (2010).

Ranalli, G. Rheology of the lithosphere in space and time. *Burg, J.-P., Ford, M. (Eds.), Orogeny through Time. Geol. Soc. London, Spec. Publ*. **121**, 19 – 37 (1997).

Rosenau, M., Oncken, O. Fore-arc deformation controls frequency-size distribution of megathrust earthquakes in subduction zones. – J. Geophys. Res., **114**, B10311, (2009).

Rubin A. M., & Ampueri J,-P., Earthquake nucleation on (aging) rate and state faults, *J. Geophys. Res.* **110**, B11312, doi:10.1029/2005JB003686 (2010).

Rubin, A.M. Episodic slow slip events and rate-and-state friction*, J. Geophys. Res*. **113**, B11414, doi:10.1029/2008JB005642 (2008).

Ruegg, J. C., et al., Interseismic strain accumulation measured by GPS in the seismic gap between Constitución and Concepción in Chile*, Phys. Earth Planet. Inter*., **175(1–2)**, 78–85, doi:10.1016/j.pepi.2008.02.015 (2009).

Ruff, L. J., Do Trench Sediments Affect Great Earthquake Occurrence in Subduction Zones?, *PAGEOPH* Volume **129**, Issue 1, 263-282, (1989).

Ruff, L., & Kanamori, H., Seismicity and Subduction Process. *Phys. Earth Planet. Inter*., **23**, 240-252, (1980).

Ruina, A. L. Slip instability and state variable friction laws. *J. Geophys. Res.* **88**, 10359–10370 (1983).

Rybacki, E., & G. Dresen, Dislocation and diffusion creep of synthetic anorthite aggregates, *Journal of Geophysical Research*, **105(B11)**, 26,017–26,036, doi:10.1029/ 2000JB900223 (2000).

Schellart, W.P. & Rawlinson, N., Global correlations between maximum magnitudes of subduction zone interface thrust earthquakes and physical parameters of subduction zones, *Physics of the Earth and Planetary Interiors*, Volume **225**, 41-67, ISSN 0031-9201, http://dx.doi.org/10.1016/j.pepi.2013.10.001, (2013)

Schellart, W.P. & Rawlinson, N. Global correlations between maximum magnitudes of subduction zone interface thrust earthquakes and physical parameters of subduction zones, *PEPI*, **225**, 41-67, http://dx.doi.org/10.1016/j.pepi.2013.10.001. (2013).

Scholz C. H. The critical slip distance for seismic faulting. *Nature* **336**, 761 – 763, doi:10.1038/336761a0 (1988).

Scholz, C. H. Earthquakes and friction laws. *Nature* **391**, 37–42 (1998).

Schubert, G., Turcotte, D. L. & Olsen, P. *Mantle Convection in the Earth and Planets*. (Cambridge University Press, 2001).

Seno, T, Stress drop as a criterion to differentiate subduction zones where Mw 9 earthquakes can occur, *Tectonophys*. **621**, 198–210, doi:10.1016/j.tecto.2014.02.016 (2014)

Shaw, B . E., & J . R. Rice, Existence of continuum complexity in the elastodynamics of repeated fault ruptures *J. Geophys. Res*., **105**, 23, 791-23,810, (2000).

Shearer, P. & Bürgmann, R. Lessons learned from the 2004 Sumatra-Andaman megathrust rupture. *Annu. Rev. Earth Planet. Sci.* **38**, 103–131 (2010).

Shibazaki,B ., and M. Matsu'ura, Spontaneous processes for nucleation, dynamic propagation and stop of earthquake rupture, *Geophys. Res. Lett.*, **19**, 1189-1192, 1992.

Simo, J., & T. Hughes, Computational Inelasticity, Interdisciplinary Applied Mathematics Series, Springer (2000).

Simons, M. et al. The 2011 magnitude 9.0 Tohoku-Oki earthquake: mosaicking the megathrust from seconds to centuries. *Science* **33**, 1421-1425 (2011).

Sobolev, S. et al. Mechanism of the Andean Orogeny: Insight from Numerical Modeling. In Oncken O. et al. The Andes, Active Subduction Orogeny. 513-535. Springer (2006).

Sobolev, S.V. & Babeyko, A. A. Thermomechanical Model of Low-angle Subduction in Central Andes Combining Geological and Recent (GPS) Deformations, (EOS, Transactions, American Geophysical Union, 85(17). (2004). at http://adsabs.harvard.edu/abs/2004AGUSM.G23A..04S

Sobolev, S.V. & Babeyko, A.Y., What drives orogeny in the Andes? *Geology* **33**, 617–620 (2005).

Strasser, F. O. Arango, M. C., & Bommer, J. J., Scaling of the source dimensions of interface and intraslab subduction-zone earthquakes with moment magnitude. *Seism. Res. Let.*. **81(6)**, 941-950, doi:10.1785/gssrl.81.6.941 (2010).

Suito, H., and J. T. Freymueller, A viscoelastic and afterslip postseismic deformation model for the 1964 Alaska earthquake, *J. Geophys. Res*., 114, B11404, doi:10.1029/2008JB005954 (2009).
Sun, T. & Wang, K. Viscoelastic relaxation following subduction earthquakes and its effects on afterslip determentaion. *J. Geophys. Res.* **120**, 1329–1344, doi:10.1002/2014JB011707 (2015).
Sun, T. et al. Prevalence of viscoelastic relaxation after the 2011 Tohoku-Oki earthquake. *Nature* **514**, 84–87 (2014).
The Geospatial Information Authority of Japan. Long-term information on crustal movement detected by GNSS-based control point. at http://mekira.gsi.go.jp/project/f3_10_5/en/index.html
Tympel J., Numerical modeling of the Cenozoic Pamir-Tien Shan orogeny, Ph.D. thesis, University of Potsdam (2014).
Tympel, J., & Sobolev, S. V. First results of 2D Thermo-mechanical modelling of Cenozoic lithospheric deformation in the Himalaya-Tibet-Pamir-Tien Shan orogen, (Geophysical Research Abstracts Vol. 13, EGU2011-8804, 2011), General Assembly European Geosciences Union (Vienna, Austria 2011).
Uyeda, S. & Kanamori, H., Back-Arc Opening and the Mode of Subduction. *J. Geophys. Res.*, **84**, 1049-1061, (1979).
van Dinther, Y. *et al*. The seismic cycle at subduction thrusts: 2. Dynamic implications of geodynamic simulations validated with laboratory models. *J. Geophys. Res.* **118**, 1502–1525 (2013).
van Dinther, Y. *et al*. The seismic cycle at subduction thrusts: Insights from seismo-thermo-mechanical models. *J. Geophys. Res.* **118**, 6183–6202 (2013).
van Dinther, Y., et al., Modeling the seismic cycle in subduction zones: The role and spatiotemporal occurrence of off-megathrust earthquakes. *Geophys. Res. Lett.*, **41**, 1194–1201, doi:10.1002/2013GL058886 (2014).
Veedu, D. M., & Barbot, S., The Parkfield tremors reveal slow and fast ruptures on the same asperity. *Nature* **532**, 361–365 (2016).
Vermeer, P. A., The orientation of shear bands in biaxial tests, *Géotechnique*, **40(2)**, 223–236, doi:10.1680/geot.1990.40.2.223 (1990).
Walsh, J. B., Stiffness in faulting and in friction experiments, *J. Geophys. Res.*, **76(35)**, 8597–8598, doi:10.1029/JB076i035p08597 (1971).
Wang, K. Coupling of tectonic loading and earthquake fault slips at subduction zones. *Pure Appl. Geophys.* **145**, 537–559 (1995).
Wang, K., & Bilek, S. L., Fault creep caused by subduction of rough seafloor relief, *Tectonophysics*, **610**, 1–24 (2014).
Wang, K., Hu, Y. & He, J. Deformation cycles of subduction earthquakes in a viscoelastic Earth. *Nature* **484**, 327–332 (2012).
Watanabe, S. et al. Evidence of viscoelastic deformation following the 2011 Tohoku-Oki earthquake revealed from seafloor geodetic observation. *Geophys. Res. Lett.* **41**, 5789–5796 (2014).

Zienkiewicz, O. C., & Tylor, R. L., The Finite Element Method Fifth edition Volume **1**: The Basis, Butterworth-Heinemann (2000).

List of Figures

Acknowledgments

First and foremost I want to thank my supervisor Prof. Dr. Stephan Sobolev, head of section “Geodynamic Modeling”, for the continuous support of my Ph.D study, for his patience, motivation, and immense knowledge. Being novice in geodynamic modeling, I was always welcomed to ask any questions at any time. Eventually through all the long discussions I came into geodynamics. I could not have imagined having a better advisor and mentor for my PhD study.

I am grateful for the opportunity to be the part of GeoSim project which let me travel to several international conferences over the years, to present my work and results. Furthermore, I would like to thank my supervisors Prof. Dr. Michael Weber and Prof. Dr. Volker John.

I am grateful to many colleagues, friends and relatives for their help, encouragement, and support, including but not limited to: The University of Potsdam for a good start in geoscience as well as providing me with the opportunity to get some teaching experience. I am grateful to Andrey Babeyko who helped me settle in the new place and advised again and again on different issues. Alexey Petrunin for setting up my workspace and clusters, and keeping calculations alive. Karen Leever and Sofia Kufner, coordinators of the GeoSim project, for helping with issues and organizing our project meetings. Anton Popov and Jens Tympel for acquainting me with SLIM3D, main tool of my study. Jonathan Bedford and Maximilian Döhmann for helping me with English and Deutsch languages. I would like to thank whole section 2.5, especially Till Bruens for helping with all sorts of issues.

Prof. Roland Bürgmann and Prof. Serge Shapiro for reviewing this thesis.

Also I would like to thank my fellow PhD students, who have helped me both academically and socially.

Last but not least, I would like to thank my family for their never-ending support: Albert, Lyailya and Nelly.

Erklärung

Hiermit versichere ich, dass ich die vorliegende Dissertation ohne unzulässige Hilfe Dritter und ohne Benutzung anderer als der angegebenen Literatur angefertigt wurde. Die Stellen der Arbeit, die anderenWerken wörtlich oder inhaltlich entnommen sind, wurden durch entsprechende Angaben der Quellen kenntlich gemacht. Diese Arbeit hat in gleicher oder ähnlicher Form noch keiner Prüfungsbehörde vorgelegen.